An Intense Attosecond Light Source - Towards Extreme Ultraviolet Pump-Probe Experiments

Campi, Filippo

2017

An Intense Attosecond Light Source - Towards Extreme Ultraviolet Pump-Probe Experiments

Filippo Campi

Doctoral Thesis

2017

An Intense Attosecond Light Source - Towards Extreme Ultraviolet Pump-Probe Experiments

Printed in Sweden by Media-Tryck, Lund, 2017

Division of Atomic Physics
Department of Physics
Faculty of Engineering, LTH
Lund University
P.O. Box 118
SE–221 00 Lund
Sweden
www.atomic.physics.lu.se

ISSN 0281-2762
Lund Reports on Atomic Physics, LRAP 539 (2017)

978-91-7753-483-9 (print)
978-91-7753-484-6 (pdf)

"If it was simple, it would have already been done"

P.J.

Abstract

This thesis presents important steps towards performing high-intensity attosecond pump-probe experiments at the Lund high-intensity extreme ultraviolet (XUV) beamline, which followed two complementary paths: maximization of the XUV intensity available in the interaction region with a gas target, and providing attosecond temporal resolution.

To maximize the energy of the XUV pulses generated via high-order harmonic generation (HHG), the macroscopic response of atoms to the driving infrared field was optimized. A major upgrade to the beamline allowed more energy to be used to drive the HHG process, with the same goal of increasing the energy of the generated XUV pulses. Two different options for reducing the duration of the XUV pulses were investigated: reducing the duration of the driving infrared pulses, and a newly conceived gating mechanism to confine the HHG process in time. Considerable effort was devoted to optimizing the focusing conditions, leading to a smaller focus and thus to higher peak intensities, by minimizing the aberrations of the wavefront of the pulses focused in the gas jet.

Intensities in the range of 10^{12} W/cm^2 have been achieved, and demonstrated by initiation of a non-linear absorption process in neon. The products of this photoionization process were detected with a newly developed particle spectrometer: a double-sided velocity map imaging spectrometer.

The pump-probe setup has been designed, implemented, tested, and integrated in the beamline. It constitutes an enabling technology that provides the beamline with the temporal resolution required for attosecond pump-probe experiments. The scheme implemented at the Lund high-intensity beamline laid the groundwork for the design of a similar scheme at the Extreme Light Infrastructure in Szeged, Hungary.

Popular Scientific Summary

Curiosity about their surroundings is the main driver of the learning process in many animal species [1, 2], but it is mainly humans that possess the capacity of abstraction necessary to replicate naturally occurring phenomena [3], and to exploit them to their advantage. This higher cognitive function has allowed mankind to make several major advances throughout history. We learned how to tame fire, to farm land, to make tools and build shelters. Since reaching these important milestones we have evolved even further and taken on increasingly more difficult challenges.

Many questions that puzzled man such as, "Are all four hooves of a galloping horse off the ground at once?" "How does a falling cat rotate to land safely on its paws?" [4] and "How does a bird fly, and can we replicate it?" [5, 6], have been already answered with the aid of physics. Taking a series of still images to form a primitive kind of video allowed the motion of these animals to be analyzed frame-by-frame so that we could see what was happening. We now take it for granted that we can take photographs and movies of anything, anytime we want to, using digital cameras or smartphones.

So are there no other fast processes occuring in nature that are worth investigating? As the limit is imposed by our own curiosity, the answer is no.

Challenges of the 21st century

The 20th century saw tremendous scientific advances leading to a boom in knowledge and technology. At the beginning of that century the structure of the atom was not completely understood [8], but by its end it was possible to detect a single atom [9]. During that same period, questions concerning events taking place at the rate of a few hundreds of frames per second, such as cats rotating in the air (see Figure 1), turned into questions about how atoms vibrate in a molecule, which would require capturing images at a rate of about 1,000,000,000,000,000, or 10^{15} frames per second. Measuring the time taken for an athlete to complete a 400 m lap requires a clock with a resolution of one hundreth of a second, while measuring the time taken for a molecule to vibrate one cycle would require a clock with a resolution of a femtosecond (1 femtosecond = 10^{-15} seconds). Such "clocks" can be constructed using lasers in so-called *pump-probe* experiments [10], which are the subject of this thesis. The resolution of these systems, corresponding to the ticks of a clock, is provided by very short bursts of light, or laser pulses.

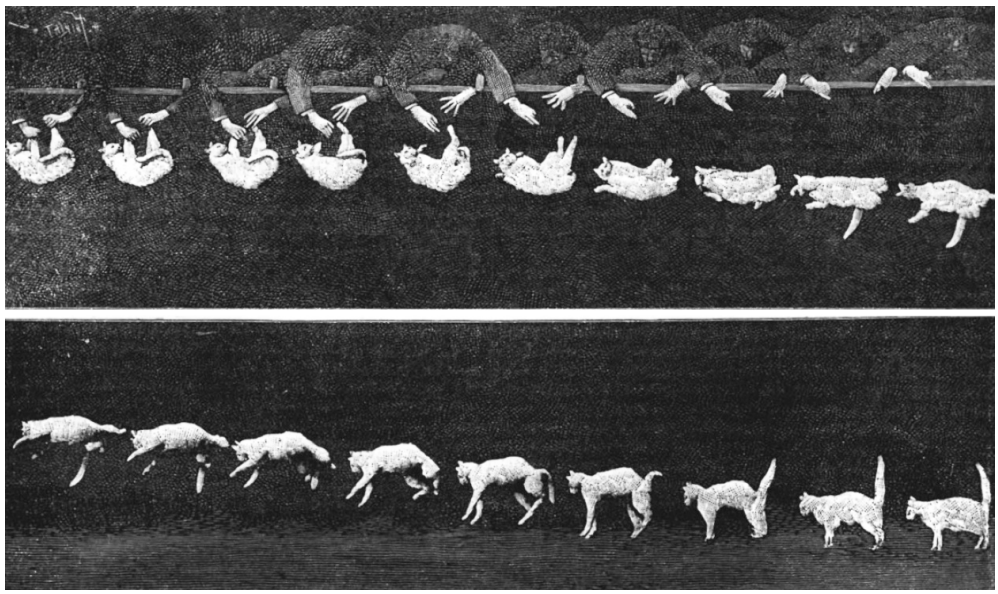

Figure 1: Solution of the falling cat problem. Photographs taken with a "chronophotographic gun" by Marey. Reproduced from Ref [7].

A scientific and technological challenge facing us now, at the beginning of the 21st century, is to develop tools that act as clocks on an even shorter timescale, the attosecond timescale (1 attosecond = 10^{-18} seconds). At this frame rate, it is possible to visualize the motion of electrons in slow motion, as the time taken for an electron to complete a single "orbit" around a nucleus is around 100 attoseconds. But why is it interesting to investigate such rapid processes? What benefits would such knowledge bring to society?

Electrons are minuscule particles that carry the unit of electric charge. The distribution of these charges in space and their movement in time define most of the properties of the materials around us. It is difficult to predict the dynamic behavior of charges, and understanding it is the first step towards controlling and replicating it. The benefit to society that may arise from replicating processes involving charges is also difficult to foresee, so there is no simple answer to the questions posed above. However, one of the challenges facing us now, and future generations, is the production of clean sustainable energy.

Nature has developed her own power-plants in the form of chlorophylls in plants, and photosynthetic bacteria. Over millions of years of evolution, they have perfected the conversion of radiative energy from the sun into chemical energy, by transferring charges from one molecule to another. If we are able to mimic the processes underlying charge transfer, it may be possible to improve the efficiency of artificial materials used to harvest solar power [11].

Attosecond technology

In the same way that femtosecond-long laser pulses are needed for femtosecond clocks, attosecond-long pulses are required for attosecond clocks. These pulses have been generated for the past fifteen years [12] via a process called high-order harmonic generation (HHG) [13, 14]. In this process a very intense femtosecond laser pulse is used to remove the electrons from atoms in a gas, to accelerate them, and to drive them back to their parent ion. The result is a burst of light comprising photons, the "units" of light, that have a much shorter wavelength than those constituting the original pulse; so short that it can reach the X-ray spectral range [15]. These bursts of light usually have durations of only a few tens of attoseconds, thus constituting the "tick" of the attosecond clock.

To investigate processes that take place on the attosecond timescale using these very short pulses, it is necessary to define two events: the first one, called the *pump* event, when the photons from a pulse remove an electron from the atom or molecule to be investigated, thus starting some dynamics; and the second one, called the *probe* event, when the photons from a second pulse remove another electron. The resulting fragments of the system being investigated are observed with detectors that provide some information about what has happened since the *pump* event took place. This information is analogous to the individual frames in a movie. If the relative delay between the *pump* and the *probe* events is varied, the sequence of the recorded frames can be re-played like a movie.

The developments presented in this thesis

The attosecond *pump-probe* experiments described above require intense attosecond pulses. The intensity determines the probability that photons from the *pump* pulse and the *probe* pulse will interact with the same target. Only then will the fragments carry information about the temporal evolution of the system investigated. To achieve a sufficiently high intensity three conditions are required: highly energetic pulses, with short durations, should be focused into a small volume. The work described in this thesis has been concerned with all three of these aspects.

To obtain highly energetic pulses, a long beamline that employs an advanced laser system to drive HHG in noble gases has been constructed at the Lund Laser Centre. To increase the efficiency of the generation process the collective response of atoms irradiated by the laser pulses was optimized. The attosecond pulses were made even shorter by compressing the femtosecond laser pulses driving HHG and by limiting the time-window during which HHG takes place. The pulses were focused into a very narrow volume by careful characterization of the optics and their alignment. The thesis also described the study of the ionization of atoms from a noble gas, neon, with these intense pulses, as well as the development of a sophisticated spectrometer to detect particles created during such processes. The main aim was to develop the tools required to record attosecond movies or, in other words, to perform attosecond *pump-probe* experiments. This was achieved by developing a setup that is able to create two identical replicas of one attosecond pulse, and to introduce a stable and reliable delay between them.

Outlook

When the Internet first saw the light of the day in the latter half of the 20^{th} century, few could have envisaged that it would become one of the defining milestones of the current anthropological era, the information era. Although attosecond science might not have the same impact on society as the Internet, it has the potential to shape the future of our species. Imagine an era where we will not only be able to fully comprehend the laws of physics, but will also be able to control the processes occurring in nature, at the most fundamental level. The benefits arising from this could cover areas from material sciences to medicine, and from steering cognition to enhancing our own bodies. The only limits are our imagination and curiosity. ï»¿

Riassunto Divulgativo

La curiosità verso l'ambiente circostante è la spinta primaria nel processo di apprendimento di molte specie animali [1, 2], ma solamente l'essere umano possiede la capacità di astrazione necessaria per riprodurre i fenomeni naturali e sfruttarli a proprio vantaggio [3]. Questa capacità cognitiva superiore ha permesso alla razza umana di compiere passi da gigante nel corso della storia. Abbiamo domato il fuoco, coltivato la terra, fabbricato utensili e creato ripari. Grazie al raggiungimento di queste pietre miliari ci siamo ulteriormente evoluti, affrontando sfide sempre più difficili.

A molte domande apparentemente impossibili, come "Un cavallo al galoppo ha, in un qualsiasi momento, tutti e quattro gli zoccoli sollevati da terra?", o "Come fa un gatto che cade a torcersi per atterrare sulle zampe?" [4] e "Come fa un uccello a volare? Possiamo imitarlo?" [5, 6], la fisica ha già trovato una risposta. Accostando una serie di fotogrammi in una sorta di film rudimentale è possibile analizzare il movimento di questi animali scatto dopo scatto, così da studiare ciò che avviene. Oggi con fotocamere e smartphone troviamo naturale poter fotografare o filmare qualsiasi cosa, quando vogliamo.

Dobbiamo quindi supporre che non ci siano in natura altri processi rapidi degni di essere approfonditi? Siccome l'unico limite è imposto dalla nostra curiosità, la risposta è no.

Sfide del XXI secolo

Il XX è stato un secolo di enorme progresso scientifico, che ha portato ad un'impennata in termini di scienza e tecnologia. Nei primi anni la struttura dell'atomo era ancora in parte sconosciuta [8], mentre verso la fine del secolo se ne poteva addirittura osservare uno [9]. Nello stesso periodo si è passati da curiosità riguardanti eventi osservabili ad un centinaio di fotogrammi al secondo, come un gatto che si torce in aria (vedi Figura 2), a curiosità sul movimento degli atomi in una molecola, che necessitano l'acquisizione di almeno 1.000.000.000.000.000 (10^{15}) immagini al secondo. Cronometrare il tempo che impiega un atleta a percorrere 400 metri di pista richiede orologi con una precisione al centesimo di secondo, mentre misurare il tempo di un ciclo di molecola in vibrazione richiederebbe degli orologi con una precisione al femtosecondo (cioè 10^{-15} secondi). Tali "orologi" vengono realizzati tramite l'uso dei laser nei cosiddetti esperimenti *pump-probe* [10], che sono l'oggetto di questa tesi. La risoluzione

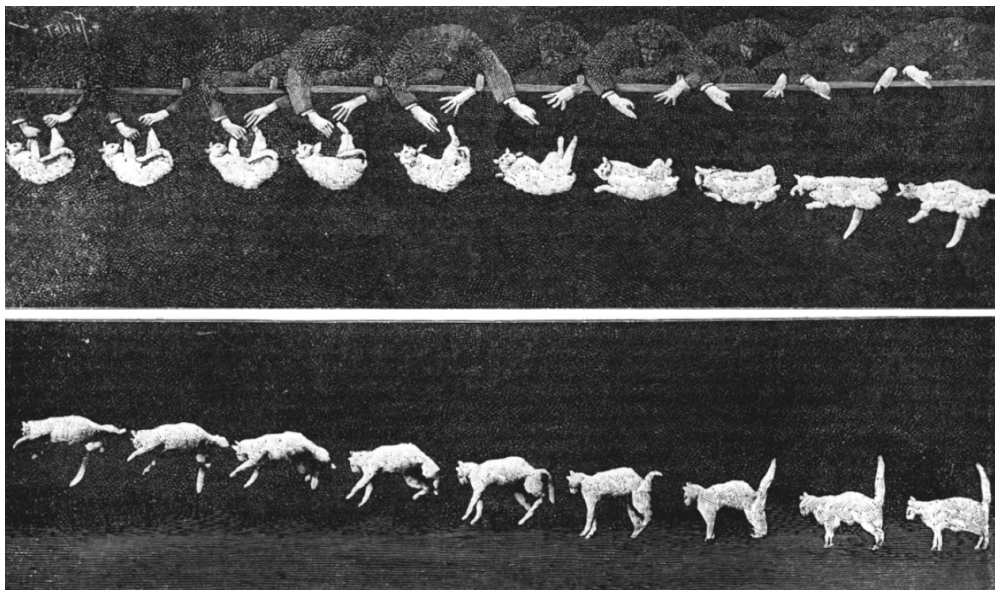

Figure 2: Soluzione del problema del gatto in caduta libera. Fotografie catturate tramite il "cannone cromofotografico" di Marey. Riprodotto dalla Ref [7].

di questi sistemi, corrispondente al ticchiettio dell'orologio, è fornita da flash di luce brevissimi o impulsi laser.

All'inizio del XXI secolo, una sfida che ci attende è sviluppare orologi che abbiano una risoluzione ancora migliore, cioè di un attosecondo (10^{-18} secondi). A questo *frame-rate* è possibile osservare il movimento degli elettroni a rallentatore, visto che il tempo che impiega un elettrone a completare una singola "orbita" attorno al nucleo è di circa cento attosecondi. Ma perché è interessante indagare questi processi così rapidi? Quali vantaggi può portare questa conoscenza alla società?

Gli elettroni sono particelle minuscole che rappresentano la quantità unitaria di carica elettrica. La distribuzione di queste cariche nello spazio e il loro movimento nel tempo definiscono le proprietà dei materiali che ci circondano. È difficile prevedere il comportamento dinamico delle cariche, ma capirlo è il primo passo fondamentale per controllare e riprodurre tali comportamenti. È altrettanto difficile prevedere i vantaggi che la società trarrebbe dalla capacità di replicare i movimenti delle cariche, pertanto non esiste una risposta univoca alle domande di cui sopra. Tuttavia, una delle sfide che le generazioni contemporanee e future si trovano ad affrontare riguarda la produzione di energia sostenibile.

La natura ha sviluppato le proprie centrali elettriche sottoforma di clorofilla nelle piante e di batteri fotosintetici. Tramite l'evoluzione che va avanti da milioni di anni, essi hanno perfezionato la conversione di energia radiativa solare in energia chimica, trasferendo cariche da una molecola all'altra. Se potessimo imitare il processo alla base del trasferimento delle cariche, potrebbe essere possibile migliorare l'efficienza dei materiali artificiali impiegati per la produzione di energia solare [11].

Tecnologia ad attosecondi

Così come i laser a femtosecondi sono alla base degli orologi al femtosecondo, gli impulsi ad attosecondi sono indispensabili per gli orologi all'attosecondo. Negli ultimi quindici anni [12] questi impulsi sono stati generati tramite un processo chiamato generazione di armoniche di ordine elevato (*high-order harmonic generation*, o HHG [13, 14]). In questo processo un impulso laser a femtosecondi ad alta intensità viene utilizzato per rimuovere gli elettroni dagli atomi di un gas, accelerarli e riportarli nuovamente allo ione da cui derivano. Il risultato è un flash di luce che contiene fotoni, la quantità unitaria di luce, che hanno una lunghezza d'onda molto più corta di quella dell'impulso originario; talmente corta che può raggiungere la regione spettrale dei raggi X [15]. Questi flash di luce hanno solitamente una durata di poche decine di attosecondi e pertanto costituiscono un "ticchettio" dell'orologio all'attosecondo.

Per studiare processi della durata di alcuni attosecondi mediante l'utilizzo di questi impulsi molto brevi, bisogna prima definire due eventi: il primo, chiamato *pump*, quando i fotoni di un impulso rimuovono un elettrone dall'atomo o molecola da studiare; il secondo, chiamato *probe*, avviene quando i fotoni di un secondo impulso rimuovono un altro elettrone. I frammenti del sistema sotto indagine vengono analizzati tramite vari rilevatori i quali forniscono informazioni su cosa sia accaduto al sistema da quando è accaduto l'evento *pump*. Queste informazioni sono come i fotogrammi di un film. Se la distanza nel tempo tra il *pump* e il *probe* viene cambiata, la sequenza dei fotogrammi registrati può essere riprodotta come fosse un film.

Gli sviluppi presentati in questa tesi

L'esperimento *pump-probe* descritto qui sopra richiede impulsi intensi della durata di alcuni attosecondi. L'elevata intensità aumenta la probabilità che i fotoni del *pump* e quelli del *probe* interagiscano con lo stesso atomo o molecola. Infatti, solo allora i frammenti porteranno con sè informazioni riguardanti l'evoluzione temporale del sistema investigato. Per ottenere un'intensità sufficientemente elevata è necessario che impulsi altamente energetici e dalla breve durata siano focalizzati in un piccolo volume. Il lavoro descritto in questa tesi ha coinvolto tutti e tre questi aspetti.

Per ottenere impulsi altamente energetici, al Lund Laser Centre si è progettata una *beamline* molto estesa che impiega un avanzato sistema laser per generare le armoniche di ordine elevato in gas nobili. Per migliorare l'efficienza del processo di generazione, si è ottimizzata la risposta sincronizzata degli atomi irradiati dal laser. Gli impulsi ad attosecondi sono stati resi ancora più brevi comprimendo gli impulsi laser al femtosecondo usati per la loro generazione e limitando la finestra temporale in cui le armoniche vengono generate. Gli impulsi vengono focalizzati in un volume molto ristretto tramite un'attenta caratterizzazione delle ottiche e del loro allineamento. La tesi descrive anche lo studio del processo di ionizzazione degli atomi di un gas nobile, il neon, grazie questi impulsi intensi. Descrive inoltre lo sviluppo di uno spettrometro sofisticato per raccogliere le particelle createsi durante tali processi.

Lo scopo principale è stato quello di sviluppare gli strumenti necessari per girare film ad attosecondi, o in altre parole per svolgere esperimenti *pump-probe* ad attosecondi. Questo scopo è stato raggiunto grazie allo sviluppo di un *setup* in grado di creare due copie identiche di un impulso ad attosecondi e di instaurare un ritardo stabile e riproducibile tra di essi.

Prospettiva futura

Quando nella seconda metà del XX secondo venne creata la rete informatica, o internet, in pochi immaginavano che essa avrebbe costituito una pietra miliare dell'attuale era antropologica, l'era informatica. La scienza ad attosecondi potrebbe non avere lo stesso impatto sulla società che ha avuto internet, tuttavia essa ha il potenziale per modellare il futuro della nostra specie. Si immagini un'era in cui non solo potremmo comprendere appieno le leggi della fisica, ma anche padroneggiare i processi che avvengono ai livelli più fondamentali della natura. I vantaggi derivanti potrebbero influenzare la Scienza dei Materiali e la Medicina, potremmo essere in grado di migliorare i processi cognitivi e biologici. L'unico limite è la nostra immaginazione e curiosità.

List of Publications

This thesis is based on the following papers, which will be referred to by their roman numerals in the text.

I **A high-flux high-order harmonic source**
P. Rudawski, C. M. Heyl, F. Brizuela, J. Schwenke, A. Persson, E. Mansten, R. Rakowski, L. Rading, F. Campi, B. Kim, P. Johnsson, and A. L'Huillier.
Rev. Sci. Instrum. **84**, 073103 (2013).

II **Two-photon double ionization of neon using an intense attosecond pulse train**
B. Manschwetus, L. Rading, F. Campi, S. Maclot, H. Coudert-Alteirac, J. Lahl, H. Wikmark, P. Rudawski, C. M. Heyl, B. Farkas, T. Mohammed, A. L'Huillier, and P. Johnsson.
Phys. Rev. A **93**, 061402 (2016).

III **Compression of TW class laser pulses in a planar hollow waveguide for applications in strong-field physics**
A. Jarnac, F. Brizuela, C. M. Heyl, P. Rudawski, F. Campi, B. Kim, L. Rading, P. Johnsson, A. Mysyrowicz, A. L'Huillier, A. Houard, C. L. Arnold.
Eur. Phys. J. D **68**, 373 (2014).

IV **Gating attosecond pulses in a noncollinear geometry**
M. Louisy, C. L. Arnold, M. Miranda, E.W. Larsen, S.N. Bengtsson, D. Kroon, M. Kotur, D. Guenot, L. Rading, P. Rudawski, F. Brizuela, F. Campi, B. Kim, A. Jarnac, A. Houard, J. Mauritsson, P. Johnsson, A. L'Huillier, and C. M. Heyl.
Optica **2**, 6 (2015).

V **Design and test of a broadband split-and-delay unit for attosecond XUV-XUV pump-probe experiments**
F. Campi, H. Coudert-Alteirac, M. Miranda, L. Rading, B. Manschwetus, P. Rudawski, A. L'Huillier, and P. Johnsson.
Rev. Sci. Instrum. **87**, 023106 (2016).

VI **The ELI-ALPS facility: the next generation of attosecond sources**
S. Kühn, M. Dumergue, S. Kahaly, S. Mondal, M. Fule, T. Csizmadia, B. Farkas, B. Major, Z. Varallyay, F. Calegari, M. Devetta, F. Frassetto, E. Mänsson, L. Poletto, S. Stagira, C. Vozzi, M. Nisoli, P. Rudawski, S. Maclot, F. Campi, H. Wikmark, C. L. Arnold, C. M. Heyl, P. Johnsson, A. L'Huillier, R. Lopez-Martens, S. Haessler, M. Bocoum, F. Boehle, A. Vernier, G. Iaquaniello, E. Skantzakis, N. Papadakis, C. Kalpouzos, P. Tzallas, F. Lepine, D. Charalambidis, K. Varju, K. Osvay, and G. Sansone.
J. Phys. B: At. Mol. Opt. Phys. **50**, 132002 (2017).

VII **A Versatile Velocity Map Electron-Ion Covariance Imaging Spectrometer for High Intensity XUV Experiments**
L. Rading, S. Maclot, J. Lahl, F. Campi, H. Wikmark, J. Peschel, H. Coudert-Alteirac, B. Oostenrijk, M. Gisselbrecht, and P. Johnsson.
Manuscript in preparation.

VIII **Micro-focusing of broadband high-order harmonic radiation by a double toroidal mirror**
H. Coudert-Alteirac, H. Dacasa, F. Campi, E. Kueny, B. Farkas, F. Brunner, S. Maclot, B. Manschwetus, H. Wikmark, J. Lahl, L. Rading, J. Peschel, B. Major, K. Varjú, G. Dovillaire, P. Zeitoun, P. Johnsson, A. L'Huillier, and P. Rudawski.
Manuscript submitted.

Other related publications by the author, not included in this thesis:

Tracing Electron-Ion Recombination in Nanoplasmas Produced by Extreme-Ultraviolet Irradiation of Rare-Gas Clusters
B. Schütte, F. Campi, M. Arbeiter, Th. Fennel, M.J.J. Vrakking, and A. Rouzée.
Phys. Rev. Lett. **112**, 253401 (2014).

Contents

Abstract v

Popular Scientific Summary vii

Riassunto Divulgativo xi

Contents 1

1 Introduction 5
- 1.1 From femtochemistry... 5
- 1.2 ...to attophysics 6
- 1.3 Attosecond pump-probe experiments 7
- 1.4 Description of the present work 7
- 1.5 Outline of this thesis 8

2 Theoretical Background 9
- 2.1 Ultrashort laser pulses 9
  - 2.1.1 Mathematical description 10
- 2.2 Pulse propagation 14
  - 2.2.1 Total external reflection and critical angle 15
  - 2.2.2 Reflective optics for XUV pulses 16
- 2.3 Ultrafast pulse diagnostics 17
  - 2.3.1 Intensity autocorrelation 17
  - 2.3.2 Field autocorrelation 18
  - 2.3.3 Second-order interferometric autocorrelation 19
  - 2.3.4 Dispersionless autocorrelation 21
- 2.4 High-order harmonic generation 22
  - 2.4.1 Microscopic response - The Three-Step Model 23
  - 2.4.2 Macroscopic effects - Phase-matching effects 26
  - 2.4.3 Scaling the focusing geometry 27
  - 2.4.4 Towards isolated attosecond pulses 28

3 High-Power High-Order Harmonic Generation 31
- 3.1 The Lund high-intensity XUV beamline 31
  - 3.1.1 The laser system and beam preparation 32

3.1.2 The high-order harmonic generation and diagnostic setup . . . 33
3.2 HHG experiments . . . 34
3.2.1 Yield optimization . . . 35
3.2.2 Generation of shorter pulses . . . 36

4 Micro-focusing end-station **39**
4.1 Application chamber . . . 39
4.1.1 Even-Lavie valve . . . 39
4.2 Photon and particle detectors . . . 40
4.2.1 XUV photodiode . . . 41
4.2.2 XUV CCD camera . . . 41
4.2.3 XUV Microscope . . . 41
4.2.4 Particle spectrometer . . . 42
4.3 XUV focusing optics . . . 44
4.3.1 Ellipsoidal and toroidal mirrors . . . 44
4.3.2 Wolter optics . . . 45
4.3.3 Alignment . . . 47
4.4 High-intensity optimization: measurement of the XUV wavefronts . . . 48
4.5 High-intensity application: TPDI of neon . . . 51

5 The pump-probe setup **53**
5.1 Split-and-delay unit . . . 53
5.1.1 Wavefront splitting . . . 54
5.1.2 Delay line and stabilization . . . 56
5.1.3 Test of the performance . . . 61
5.1.4 Alignment . . . 63
5.2 Volume autocorrelation of XUV pulses . . . 64
5.3 First results of time-resolved experiments . . . 68
5.3.1 Autocorrelation of IR pulses . . . 68
5.3.2 Above-threshold ionization of argon . . . 71
5.3.3 Delay-dependent XUV intensity distribution in the focus . . . 71

6 Summary and Outlook **75**
6.1 Further developments . . . 76

Appendix - Raytracing **79**

Comments on the papers **83**

Acknowledgements **85**

References **89**

Papers

I A high-flux high-order harmonic source 101

II Two-photon double ionization of neon using an intense attosecond pulse train 110

III Compression of TW class laser pulses in a planar hollow waveguide for applications in strong-field physics 118

IV Gating attosecond pulses in a noncollinear geometry 127

V Design and test of a broadband split-and-delay unit for attosecond XUV-XUV pump-probe experiments 133

VI The ELI-ALPS facility: the next generation of attosecond sources 141

VII A Versatile Velocity Map Electron-Ion Covariance Imaging Spectrometer for High Intensity XUV Experiments 182

VIII Micro-focusing of broadband high-order harmonic radiation by a double toroidal mirror 195

Chapter 1

Introduction

Our understanding of the world stems from the abstraction of what we perceive and the deduction of a general theory meant to explain our perception. Since the scientific revolution, this approach has been widely accepted as a way of expanding our knowledge [16], and scientists are constantly striving to improve the way we perceive our surroundings. Thanks to these efforts, we are now able to measure many different observables that we cannot detect with our senses, leading to modern physics. Such a paradigm shift allows us to push the envelope of knowledge forward and seek answers to new questions arising from our curiosity. One aspect of our surroundings that we have always found compelling is systems that are too fast to be visualized. The work presented in this thesis focuses on developing tools to advance the detection limits in the ultrafast systems.

1.1 From femtochemistry...

Thanks to modern technology, commercially available cameras can acquire thousands or even millions of images per second. More advanced devices can capture motion on the nanosecond timescale (1 nanosecond = 10^{-9} seconds), but to study events faster than this, it is necessary to develop alternative techniques.

In the quest to improve temporal resolution, so-called pump-probe techniques have been developed [10]. The main idea behind these techniques is to use a first event (the pump) to excite a system, and a second event (the probe) to record the changes that have taken place in the system since the pump event took place. By repeating the measurement with different time delays between the pump and the probe, it is possible to reconstruct the evolution of the system and find correlations between different observables.

The Nobel Prize in Chemistry was awarded to A. Zewail in 1999 [17], for his pioneering work on monitoring chemical reactions on the femtosecond timescale (1 femtosecond = 10^{-15} seconds). Up until that time it had been possible to predict the outcomes of a chemical reaction, given the intial reactants, without knowing what has

happened during the reaction. With the dawn of femtochemistry, the nuclei involved in the reaction could be followed on their natural timescale, i. e. femtoseconds, and their relative arrangement could be used to predict the final outcome [18].

Recent advances in theoretical modeling of molecular systems have predicted that charge oscillations take place long before nuclear motion [19], and these influence the subsequent structural changes [20]. Hence, if we are to fully understand the nature of chemical reactions, we must understand the dynamical behavior of the charges, on their natural timescale, i.e. attoseconds (1 attosecond = 10^{-18} seconds).

Obtaining a deep and comprehensive understanding of a naturally occuring process is usually the first step towards controlling and mimicking it. The potential benefits of mastering ultrafast phenomena such as charge transfer are immense, ranging from a more efficient solar power harvesting, to counteracting the pathological consequences of photodamage of DNA or misfolding of proteins. If we are to achieve this, it is necessary to extend established femtosecond pump-probe techniques to the attosecond regime.

1.2 ...to attophysics

The main tool enabling the extension of pump-probe techniques to the attosecond regime are attosecond-long pulses [12]. Such pulses are readily produced in the extreme ultraviolet (XUV) spectral region via a process called high-order harmonic generation (HHG) in gases [13, 14].

The HHG process has an intrinsically low conversion efficiency, thus yielding low-energy pulses, and the optical properties of materials in the XUV spectral region make dealing with these pulses challenging. For these reasons, the first experimental observations of the "footprints" of charge dynamics in molecules were through indirect methods. Dynamics were initiated with an attosecond XUV pulse (the pump event) and then detected with the aid of a femtosecond infrared (IR) pulse (the probe event) [21]. While in that experiment it was possible to observe the signature of femtosecond dynamics, the presence of a femtosecond-long IR pulse limits the resolution, and if faster dynamics were present, it would not be possible to observe them. Furthermore, the presence of the IR field in the experiment may distort the dynamics to be probed.

In order to perform a "cleaner" experiment, it would be preferable to implement an XUV attosecond pump-probe scheme; in other words, an experiment in which both the pump and the probe pulses have attosecond-long structures and lie in the XUV spectral region [22]. These pulses should carry as many photons as possible, in a short time, and in a small space; in other words, they should be characterized by high intensities. High intensity is required to increase the probability of one photon from the pump pulse and one from the probe pulse interacting with the same system. Only then will the measurement carry information about the evolution of the system under investigation. Furthermore, the short duration of the pulses ensures high resolution in the experiment. Finally, it should be possible to set the delay between the pump and the probe events with attosecond precision, and to maintain it throughout the course of the experiment.

1.3 Attosecond pump-probe experiments

Despite the intrinsically low conversion efficiency of the HHG process, XUV attosecond pulse trains (APTs) with energies exceeding a microjoule have been reported in a few laboratories around the world [23–26]. When a pulse of this energy is focused down to a spot of a few micrometers, the peak intensity reaches values that are high enough to initiate non-linear processes [27, 28]. As in the optical regime (visible and infrared), a non-linear process can be used as a pulse diagnostic, if two replicas of the same pulse are produced and delayed with respect to each other. XUV autocorrelation was first reported in 2003, and can be regarded as the first XUV pump-probe experiment, where no dynamics were investigated [29].

In the following years, a few more experiments involving APTs were reported, mainly investigating atoms and small molecules, such as nitrogen [30, 31] and hydrogen [32, 33]. While APTs carry the entire energy generated and provide attosecond resolution, their overall envelope is responsible for an autocorrelation trace that is a few tens of femtosecond long [34], and any signal arising from the probed dynamics must be deconvoluted from the autocorrelation contribution.

The alternative to APTs is isolated attosecond pulses (IAPs) [35–38]. In order to produce these, the HHG process is combined with one of the available gating techniques to confine the generation process within one half cycle of the driving field. This leads to a continuous spectrum that corresponds to a single pulse in time, potentially with durations below 100 attoseconds [39], thus improving the time resolution. The implementation of these gating techniques leads to a more complicated and lossy optical setup [40]. In either case, the result is a considerable decrease in the overall conversion efficiency, leading to lower energies per pulse, and thus to lower peak intensities.

IAPs have been reported with energies of about 1 µJ [25]. Despite the fact that this is about ten times smaller than that of APTs [24], researchers have managed to obtain intensities high enough to initiate non-linear absorption in, for instance, xenon [22]. A few studies have been published in which the authors were able to successfully probe the dynamic behavior of the system.

Regardless of whether the XUV pulse is a train of pulses or only a single pulse, the optical setup needed for a pump-probe scheme is rather complicated, as will be explained later, and losses in the system will reduce the intensity even further. In order to achieve the highest possible intensity, the focusing components and their precise alignment are of the utmost importance.

1.4 Description of the present work

The long-term goal of the group working at the Lund high-intensity XUV beamline is to study non-linear interactions between light and bio-relevant molecules, and several important steps towards this were made during the course of my work. Immediately before I started my Ph.D. studies, the laboratory hosting the intense XUV beamline was rebuilt, providing more space to develop the beamline. The reason for such a major upgrade was the desire to use a very loose focusing geometry in the HHG experiments, as well as to install a new experimental end-station where the XUV radiation could be refocused and the products of the interaction with a gas target

detected with newly designed spectrometers. The loose focusing geometry was tested as a means of increasing the energy of the XUV pulses generated, while the refocusing station allows high intensities to be achieved. In fact, the extended length of the setup allows for a greater demagnification between the object (the generation volume) and the image (the focus in the experimental region).

The main goal of the work described here was to develop and implement the tools required to perform XUV pump-probe experiments. My work was mainly concerned with setting up and optimizing the beamline, testing some crucial components, and designing and developing the pump-probe setup. The beamline was optimized so as to maximize the intensity available for pump-probe experiments, which is a crucial requirement, as explained above.

The aim of the experiments presented in Papers **I** and **II** was to maximize the efficiency of the HHG process, thus increasing the available pulse energy.

Papers **III** and **IV** describe experiments aimed at reducing the duration of the generated pulses.

The main focus of my Ph.D. studies was the design and development of the pump-probe setup. Testing the split-and-delay unit led to Paper **V**, while a scaled-up version of the device was designed to be implemented in the long gas high-order harmonic generation beamline at the Extreme Light Infrastructure Attosecond Light Pulse Source (ELI-ALPS) in Szeged, Hungary. This is described in Paper **VI**.

Considerable effort was devoted to understanding and otimizing the focusing conditions, as described in Paper **VIII**.

The above-mentioned experiments led to the availability of intense pulses for XUV experiments, in particular pump-probe experiments. The first observation of a nonlinear process with this beamline is also reported in Paper **II**.

Furthermore, a new particle detector was developed and implemented, as described in Paper **VII**.

1.5 Outline of this thesis

Chapter 2 provides the theoretical background necessary to understand the most important concepts described in this thesis, including a mathematical description of ultrashort pulses, a quasi-classical HHG model, and a description of some of the well-established pulse metrology techniques. Chapter 3 describes the HHG setup used throughout the work, together with some of the results regarding optimization of the generated pulse energy, and reduction of the pulse duration. Chapter 4 describes experimental efforts towards obtaining and demonstrating high intensity of the XUV pulses, through optimization of the focusing components and the detection of a second-order ionization process. Chapter 5 presents the central part of this work, i.e., a description of the design and implementation of the pump-probe setup, and the tests performed on it. It also touches upon some aspects of pulse metrology in the XUV. The final chapter presents a summary of the work carried out, and gives some information on the activities and upgrades planned for the near future. The appendix presents a few concepts of raytracing, as this tool has been widely utilized throughout this work.

Chapter 2

Theoretical Background

This chapter provides the mathematical framework for ultrashort pulses and their interaction with matter during their propagation. The latter encompasses both the linear interaction, which results in the optical properties of materials, and the highly non-linear interaction in the HHG process. Furthermore, this chapter introduces the basis of pulse metrology in the visible and IR spectral regions, laying the ground for the extension of these techniques to the XUV spectral region, described in Chapter 5.

2.1 Ultrashort laser pulses

Since the early days of laser physics, soon after the invention of the first laser [41], there has been increasing interest in producing short bunches, or pulses, of light. The first semiconductor [42] and solid state lasers [43] were naturally pulsed, and the development of the first gas lasing medium marked the dawn of continuous-wave lasers. The first short pulses were produced using the Q-switching technique [44], and were in the nanosecond regime (1 ns = 10^{-9} s). Further developments led to the advent of the mode-locking technique [45] which allows the production of pulses down to the picosecond regime (1 ps = 10^{-12} s) [46] and femtosecond regime [47, 48], together with the discovery of new lasing materials that supported spectral bandwidths broad enough for the pulse to be amplified and compressed to such a short duration [49]. In fact, one of the fundamental principles of ultrashort pulses is that the product of the time and bandwidth has a lower limit, and for gaussian pulses it is: $\Delta\tau\Delta\nu \geq 0.44$ [50]. In other words, the broader the spectrum ($\Delta\nu$), the shorter the pulse ($\Delta\tau$).

The term "ultrashort" usually describes pulses ranging across the femtosecond regime, and more recently, the attosecond regime [51]. In general, the duration of a pulse is limited by the oscillation period of its central frequency. Thus, if pulses shorter than 1 fs are to be produced, their central frequency must be higher than 1 PHz (1 PHz = 10^{15} Hz), corresponding to a wavelength of 300 nm, or shorter.

Regardless of the exact pulse duration, direct measurements are not possible when the pulse is shorter than, or comparable to, the response time of the electronics (hun-

dreds of picoseconds, at best). Section 2.3 addresses the problem of ultrashort pulse diagnostics.

2.1.1 Mathematical description

Temporal/spectral domain

An optical ultrashort pulse can be described in the temporal domain by its complex amplitude $\tilde{U}$:

$$\tilde{U}(t) = \tilde{A}(t)e^{i\omega_0 t},$$

where $\tilde{A}$ is the envelope and $\omega_0 = 2\pi\nu_0$ is the angular frequency corresponding to the central frequency ν_0, or carrier frequency. It is common to refer to the angular frequency as the frequency, as will be done here. While the usual convention is to define a pulse in the complex domain, its physical representation is the real part of such a complex value.

The envelope can be written as $\tilde{A}(t) = |\tilde{A}(t)|\exp[i\phi(t)]$, where $\phi(t)$ is the temporal phase, so that:

$$\tilde{U}(t) = |\tilde{A}(t)|e^{i[\omega_0 t+\phi(t)]}.$$

The corresponding description in the spectral, or frequency, domain is related to that in the temporal domain through the Fourier transform:

$$\tilde{U}(\omega) = \mathcal{F}\{\tilde{U}(t)\} = \int \tilde{A}(t)e^{-i(\omega-\omega_0)t}dt = \tilde{A}(\omega-\omega_0).$$

In other words, the spectrum of the pulse is that of the envelope, centered at ω_0, i.e. the carrier frequency.

$\tilde{U}(\omega)$ is a complex quantity and as such it is characterized by an amplitude and a phase, namely the spectral phase. It is possible to show that if the temporal phase is constant, the spectral phase is also constant. Similarly, if the temporal phase is quadratic, the spectral phase is also quadratic.

It is possible to express the intensity of the pulse as:

$$I(t) = \frac{cn\epsilon_0}{2}|\tilde{U}(t)|^2,$$

where c is the speed of light in vacuum, n is the refractive index of the medium through which the pulse is propagating, and ϵ_0 is the permittivity of vacuum.

As an ultrashort pulse is an electric field confined in time, but containing a wide range of frequencies, another relevant quantity is the instantaneous frequency ω_i, which is, by definition, the derivative of the temporal phase of $\tilde{U}(t)$:

$$\omega_i(t) = \omega_0 + \frac{d\phi(t)}{dt}.$$

If the phase is linear with t, the instantaneous frequency is constant over time, i.e. the electric field oscillates at the same frequency at different points in time, and the temporal width of the pulse is the shortest supported by its spectral bandwidth.

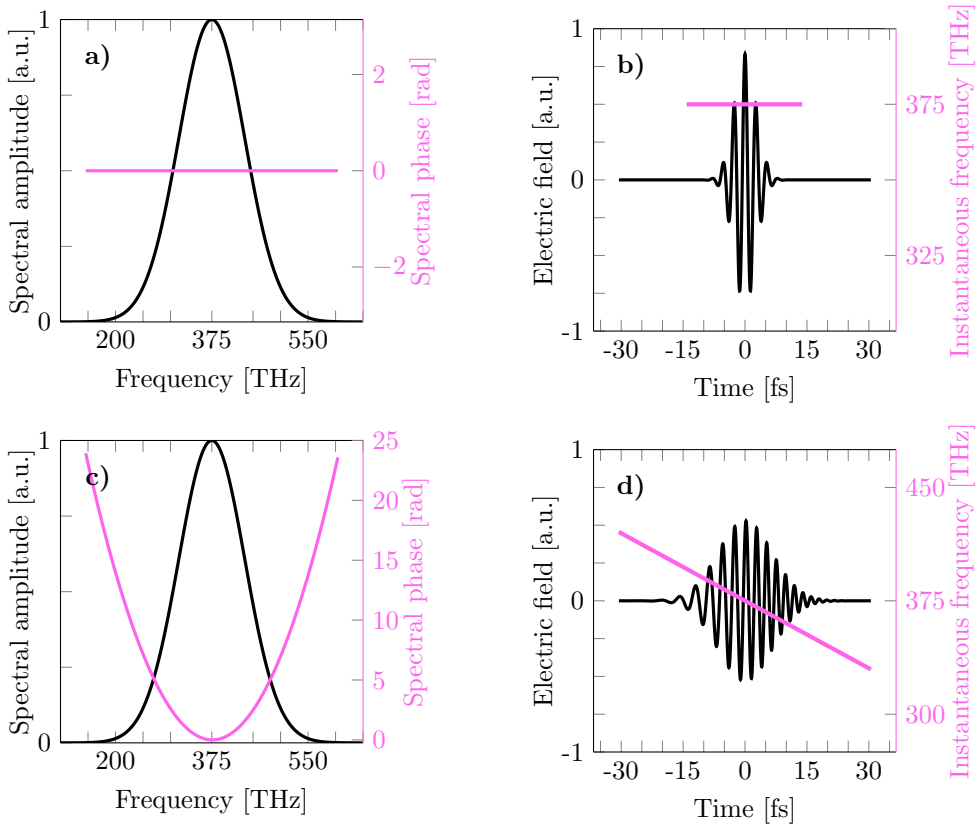

Figure 2.1: Effect of the spectral phase on short pulses. a, c) Spectral amplitude and phase of a broadband IR pulse. b, d) Temporal profile of the electric field and its instantaneous frequency.

Conversely, if the phase is non-linear in time, the instantaneous frequency shows a time-dependent behavior. The electric field oscillates at different frequencies at different points in time, and the pulse is called "chirped". It can be shown that a chirped pulse is also streched in time compared to a pulse with the same spectral amplitude and a constant phase, and constant instantaneous frequency.

This effect is shown in Figure 2.1. Panel a) shows the spectral amplitude of an ultrashort IR pulse, centered at 800 nm, or 375 THz. The inverse Fourier transform of the spectrum is the pulse profile as a function of time. The corresponding electric field, i.e. the real part of the pulse profile, is shown in panel b). It oscillates at the same frequency at all points in time, and its instantaneous frequency is constant (purple line) because its temporal phase, and thus its spectral phase, is flat. Panels c) and d) show the corresponding quantities for a quadratic spectral phase. The resulting instantaneous frequency varies in time and the duration of the pulse is longer. It is important to note that, as the overall energy carried by the pulse is the same in both cases, not only does a chirped pulse have a longer duration, it also has a lower peak intensity.

Such behavior is characteristic of any light pulse, but it is more dramatic for ultrashort pulses and special care has to be taken to avoid temporal broadening. In general, the shorter the pulse the more it tends to stretch during propagation in a medium. This phenomenon is called group velocity dispersion, and is intrinsically related to the optical properties of the material, namely the refractive index.

The spatial domain

In the spatial domain, gaussian beams, a solution of the paraxial Helmholtz equation [50], are used to describe laser beams. The complex electric field distribution $\tilde{U}$ can be expressed in the general form by:

$$\tilde{A}(x,y,z) = \tilde{A}_0(x,y,z)e^{-i\psi(x,y,z)} = A_0(x,y,z)\exp(-i(kz+\frac{k(x^2+y^2)}{2R(z)}-\zeta(z))), \quad (2.1)$$

where z is the propagation direction, and x and y are two orthogonal transverse directions. The term $\tilde{A}$ represents the complex amplitude of the electric field in space. The imaginary exponent $\psi(x,y,z)$ is the spatial phase, and in the case of gaussian beams it can be decomposed into three different terms. The first term, where $k = \omega/c$ is the wavevector, represents the phase accumulated by a plane wave, and the last two terms describe the phase of the paraboloidal wave as it propagates. The second term, albeit explicitly depending only on the transverse coordinates (x,y), contains an implicit z-dependence through the value of the radius of curvature $R(z)$. The last term $\zeta(z)$, namely the Gouy phase, is the difference between the on-axis phase for a plane wave and for a gaussian wave.

An important concept in wave optics is the wavefront. This is defined as the surface of constant phase. In the case of a plane wave, the wavefronts are planes perpendicular to the direction of propagation separated in space by the wavelength of the field. The upper part of Figure 2.2 shows a comparison between the wavefronts of a plane wave (grey dashed lines) and an ideal gaussian wave (solid red lines) at three different distances along the propagation axis. At the location of the beam waist ($z = 0$), the two wavefronts are flat (the radius of curvature R is infinite) and they coincide because the Gouy phase is zero; the only difference being the lateral extent of the intensity distribution. In fact, a plane wave extends infinitely in the lateral direction, by definition. At a given plane corresponding to $z = \overline{z}$ the gaussian wavefront is curved and its radius of curvature is proportional to $\overline{z} + 1/\overline{z}$. Because of the divergence, the beam is broader than at its waist and the Gouy phase is different from zero. At a plane placed at infinity, the wavefront becomes flat as its radius of curvature approaches infinity. Strictly speaking, the wave is also not confined in the lateral direction. In this plane the Gouy phase has reached its asymptotic value of $\pi/2$.

Although a rigorous mathematical treatment of wavefront aberrations is beyond the scope of this text, it is useful to touch upon a few aspects of those for the understanding of the rest of the text, and especially Paper **VIII**.

At any given plane $\overline{z}$ the wavefront, which is directly related to the spatial phase, can be written as:

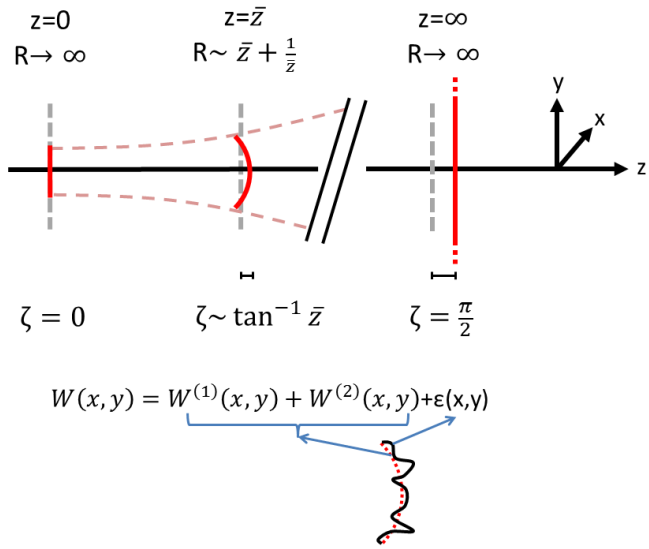

Figure 2.2: The upper part represents three gaussian wavefronts (red lines) at three different planes: at the beam waist, at a given distance along the direction of propagation $\overline{z}$, and at infinity. The dashed red line indicates the evolution of the beam width along the propagation axis, and the grey dashed lines are the corresponding wavefronts of a plane wave. R is the radius of curvature of the gaussian wavefronts, and ζ is the Gouy phase. The lower part of the figure shows an example of an aberrated wavefront (black line) with a reference gaussian wavefront (red dashed line).

$$W(x,y,\overline{z}) = \frac{\psi(x,y,\overline{z})}{k} = \sum_{n,m} a_{n,m} Z_{n,m}(x,y,\overline{z}) = \\ = W^0(\overline{z}) + W^1(x,y,\overline{z}) + W^2(x,y,\overline{z}) + \epsilon(x,y,\overline{z}),$$

where $a_{n,m}$ are the coefficients expressing the relative weights of the Zernike polynomials $Z_{n,m}$. The terms $W^{(i)}$, with i=0,1,2, represent the first three orders of the un-aberrated wavefront expansion, while ϵ represents the aberrations of the wavefront. There are different definitions of Zernike polynomials and of their order in different coordinate systems. It is therefore important to be aware of the convention used. A thorough treatment of wavefront decomposition can be found elsewhere (e.g. Ref. [52]).

The zeroth-order W^0 is a constant mean value of the phase that does not affect the overall shape and can always be subtracted from the expansion; for this reason it is not shown in Figure 2.2. There are two first-order terms, W^1, that describe linear slopes in the phase profile, thus defining the x- and y-tilts (in the corresponding cartesian coordinates). A flat but tilted wavefront describes a plane wave that is propagating at an angle to the optical axis and therefore, rather than constituting an aberration, it gives rise to a displacement of the intensity distribution from the optical axis. The second-order term, W^2, is the so-called defocus term. This describes the parabolic

curvature of the wavefront that is typical of a gaussian beam out of the focal plane, and in practice indicates how far from the focal plane the considered wavefront is, and therefore does not constitute an aberration.

The lower part of Figure 2.2, represents an ideal gaussian wavefront (red dashed line), and an aberrated one (black solid line); the difference between them being ϵ. The term ϵ describing the aberrations of the wavefront contains two second-order terms, 0° astigmatism and 45° astigmatism, as well as higher-order terms, accounting for coma and higher-order aberrations.

Analysis and decomposition of the wavefront of a beam can be used to assess the quality of a beam and the relative amount of aberrations introduced by sub-optimal alignment of optical elements in the beam path, especially focusing elements. It is important to point out that distortion of the wavefront indicates non-optimal focusing. This is crucial in the case of high-intensity experiments, as the peak intensity is inversely proportional to the focal area.

2.2 Pulse propagation

The refractive index, n, is intimately related to the response of the material to an electromagnetic field and, in particular, it describes the velocity at which an electromagnetic wave moves in a given material, relative to the speed of light:

$$n = \frac{c}{v_p},$$

where v_p is the phase velocity, i.e. the wave propagation velocity through the medium. Microscopically, the refractive index describes the response of the bound electrons when exposed to an electric field. The refractive index is ultimately responsible for the macroscopical behavior of optical elements when irradiated by light of different wavelengths. A thorough description of the relation between refractive index and the optical properties of materials is beyond the scope of this work, but a few relevant aspects are highlighted below.

Formally, the refractive index can be expressed as the sum of its real and imaginary parts:

$$\tilde{n}(\omega) = \delta(\omega) + i\beta(\omega), \tag{2.2}$$

where δ is the real part, and β is the imaginary part.

To visualize the relation between the complex refractive index and absorption and reflection, it is useful to consider a plane monochromatic wave propagating along the z direction:

$$U(z,t) = U_0 e^{-i(\omega t - \tilde{k}z)}, \tag{2.3}$$

where $\tilde{k} = \omega\tilde{n}/c$ is the wave vector associated with the plane wave. Inserting Equation 2.2 into Equation 2.3 gives:

$$U(z,t) = U_0 \exp(-i\omega(t - \frac{z}{c}\delta)) \exp(-\beta\frac{\omega}{c}z). \tag{2.4}$$

The first exponential describes the phase shift accumulated by the wave during propagation in the material, while the second is an exponential attenuation, directly related to the imaginary part of the complex refractive index. The imaginary part of the refractive index is very small for most common sorts of glass at IR and visible wavelengths, thus the electromagnetic radiation can penetrate several meters into the material with only small losses. However, at ultraviolet wavelengths, especially for vacuum ultraviolet to XUV, the attenuation is very strong and the intensity of the radiation falls to $1/e$ of the incident value within a distance ranging from a few tens of nanometers to a few tens of micrometers from the surface. This strong attenuation makes transmissive optics unfeasible in this spectral region, and reflective optics must be used.

The real part of the refractive index has an implicit wavelength dependence that causes different spectral components to propagate at different velocities within the material, and to accumulate different phase shifts. This is the effect that was defined as group velocity dispersion in Section 2.1.1 and it leads to a stretching of the pulse in time, thus reducing the peak intensity.

There is one case of interest in the present work where the combination of high losses and dispersion is desirable: thin metallic foils. In fact, XUV photons are able to penetrate a few hundreds of nanometers in certain metals, whereas IR photons are rapidly absorbed. This provides a filter, and in most HHG-based experiments foils of aluminum (or other metals) are employed as a means of blocking the driving radiation while only attenuating the XUV radiation. Furthermore, pulses generated by HHG exhibit a so-called attochirp (see section 2.4.1) which results in a longer pulse duration than that supported by the large bandwidth. Metallic filters can be used to compensate for this effect, thus leading to shorter pulses and higher intensities [53, 54].

2.2.1 Total external reflection and critical angle

While Snell's law for refraction yields the phenomenon of total internal reflection in the visible and IR spectral regions, the same law causes peculiar behavior in the XUV region.

In fact, the real part of the refractive index of materials is usually greater than one at IR wavelengths, and this causes radiation traveling from a material to air to bend further from the normal to the surface. As the angle of incidence is increased, it reaches a certain angle at which the refracted ray coincides with the interface itself. At this angle, called the critical angle, the radiation is completely reflected and transmission is suppressed. This phenomenon is called total internal reflection.

For short wavelengths (XUV, X-rays) the real part of the refractive index of standard materials is less than one, unity being the refractive index of vacuum, by definition. At an interface between vacuum and a material, the former is the medium with the higher refractive index, and radiation propagating from vacuum into the material will be bent further from the normal to the interface. As the angle of incidence is increased, it reaches a certain angle (critical angle) where the refracted radiation coincides with the interface itself. This physical behavior is analogous to the previous case, but the nomenclature differs. It is intuitive to define this phenomenon as total external reflection, as at high angles of incidence the radiation is confined outside the material.

2.2.2 Reflective optics for XUV pulses

Apart from accounting for the group velocity dispersion, the real part of the refractive index is responsible for the phenomena of total internal/external reflection as well as the reflectivity of materials at their interface. The power reflection coefficient $R = I_r/I_i$, where I_r and I_i are the reflected and incident intensities, respectively, can be seen as the sum of the contributions arising from the two polarization components. For the sake of simplicity let us consider only the reflectivity coefficient for s-polarization, i.e. the component perpendicular to the plane of incidence. For a field impinging at an angle ϕ from the normal to the interface between vacuum and a medium with refractive index $\tilde{n}$, this is given by the Fresnel equation [55]:

$$R_s = \frac{\left|\cos\phi - \sqrt{\tilde{n}^2 - \sin^2\phi}\right|^2}{\left|\cos\phi + \sqrt{\tilde{n}^2 - \sin^2\phi}\right|^2}, \tag{2.5}$$

which increases monotonically as the angle of incidence increases from zero to $\pi/2$.

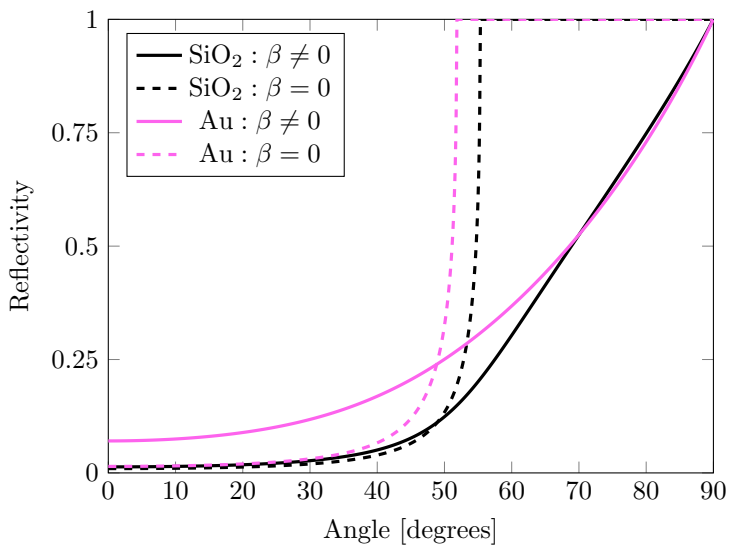

Figure 2.3: Reflectivity of silica (black) and gold (purple). The dashed curves represent the ideal lossless case, and the solid curves the real case. The curves were calculated from Equation 2.5 for a wavelength of 34.8 nm and s-polarized radiation.

Figure 2.3 shows the reflectivity at the interface between vacuum and two different materials (silica: SiO_2 and gold: Au) at a wavelength of 34.8 nm (35.6 eV).

The dashed curves represent the ideal case of lossless materials (when the imaginary part of the refractive index β is zero). The reflectivity levels off at the value of 1 for angles equal to, or greater than, the critical angle. The critical angle depends only on the real part of the refractive index, and the closer it is to 1, the smaller the critical angle [55].

When the absorption is included, the solid curves show that the reflectivity indeed increases with increasing angle of incidence, but it never reaches the value 1. This is

because, despite the suppression of transmission, the impinging photons are absorbed and the overall reflectivity is lower than in the ideal (lossless) case. For radiation with a given spectral width, different parameters should be taken into account when designing an XUV beamline.

- Metallic optics generally offer higher reflectivity than glasses for spectral components above a couple of tens of eV;
- however, glass substrates allow for the deposition of thin dielectric films, which can be designed to achieve very high reflectivity, but only in a narrow spectral window;
- increasing the angle of incidence increases the reflectivity of mirrors. This comes at the expense of practicality and costs, as a larger angle of incidence requires optics with larger apertures, and the small deviation introduced upon reflection leads to the need for larger setups.

As mentioned in the introduction, the goal at the high-intensity XUV beamline in Lund is to perform high-intensity experiments. In order to maintain high intensity throughout the beamline, two aspects must be addressed: minimizing the energy loss for each pulse by designing high-reflectivity optics, and preserving the spectral bandwidth, in order not to elongate the temporal structure of the pulses. The natural choice was thus to design the beamline for a grazing angle using metallic optics, with no coating. The grazing angle θ is the complementary to the incidence angle ($\theta = \pi/2 - \phi$), and it is used out of convenience for the XUV spectral region.

2.3 Ultrafast pulse diagnostics

In order to measure the duration of an event, it must be substantially longer than the response time of the measurement system, and therefore a direct measurement of femto- or attosecond-long pulses is not possible. However, it is possible to record a signal that is proportional to the length of the original pulse even with a slow detector, by applying a short gate window to the pulse, and varying the relative delay. The temporal resolution of the resulting measurement will depend on the temporal width of the window function applied. When sufficiently short windows are not available, the pulse itself can be used as an optical window function [50]. Such measurements are called autocorrelations, and there are various kinds, which will be presented in the following sections.

2.3.1 Intensity autocorrelation

When the window function is a delayed replica of the pulse itself, and the measured signal is proportional to the product of the intensity of the two individual pulses I, the recorded trace is called an intensity autocorrelation and its analytical expression is:

$$G_I(\tau) = \int I(t)I(t-\tau)dt,$$

where τ is the delay between the two replicas.

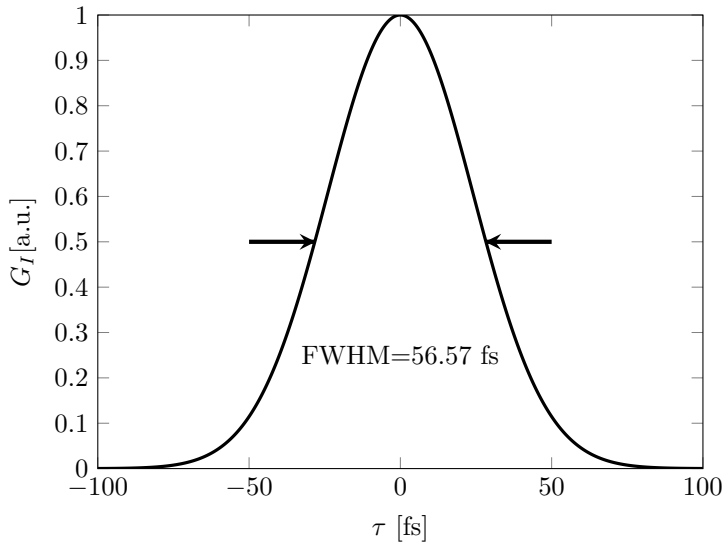

Figure 2.4: Intensity autocorrelation trace for a transform-limited 40 fs gaussian pulse.

As Figure 2.4 shows, since $I(t)$ is a real function, $G_I(\tau)$ is symmetrical about the peak value, $G_I(0)$. It approaches zero for infinite delays, i.e. when the two replicas do not overlap in time. This feature gives this technique the advantage of being background-free. The autocorrelation width is generally broader than the pulse itself. However, by assuming a certain temporal shape, a deconvolution factor can be applied and the original width can be retrieved.

It should be noted that only the duration can be retrieved from an intensity autocorrelation. No phase information can be obtained, as this measurement only allows the magnitude of the envelope of the pulse to be probed. In fact, the autocorrelation function G_I is, by definition, the Fourier transform of the absolute square of the spectral intensity [56].

An intensity autocorrelation trace is obtained, for example, when two replicas of a pulse are non-collinearly focused into a second harmonic generation crystal, and the second harmonic signal is acquired with a photodiode.

2.3.2 Field autocorrelation

If the two pulse replicas are superimposed on the sensitive surface of a slow detector and their interference pattern is recorded, without introducing a second-order process, some information can be obtained about the spectral intensity $I(\omega)$. The spectral intensity is defined as: $I(\omega) = |\tilde{U}(\omega)|^2$, where $\tilde{U}(\omega)$ is the spectral amplitude of the electric field of the pulse. By definition the autocorrelation of a function is the Fourier transform of the spectral intensity of the function itself, and therefore the field autocorrelation of a pulse, $R_U(\tau)$, provides information about its spectrum.

The field autocorrelation is a function of the delay τ:

$$R_U(\tau) \propto \int |\tilde{U}(t) + \tilde{U}(t-\tau)|^2 dt = \\ = \int |\tilde{U}(t)|^2 dt + \int |\tilde{U}(t-\tau)|^2 dt + 2\mathrm{Re} \int \tilde{U}(t)\tilde{U}(t-\tau) dt.$$

By inserting $\tilde{U} = \tilde{A}\exp(i\omega_0 t)$ in the previous equation, it can be shown that it reduces to [50]:

$$R_U(\tau) \propto G_A(0) + |G_A(\tau)| \cos[\omega_0 \tau - \arg(G_A(\tau))],$$

where $G_A(\tau) = \int A^*(t)A(t-\tau)dt$ is the autocorrelation function of the complex envelope.

Since the field autocorrelation of a pulse relates only to its spectral intensity, the shape of the spectral phase has no impact on the field autocorrelation trace, hence no information can be retrieved from it about the actual chirp or duration. As a consequence, the analysis of the envelope of the curve $G_A(\tau)$ can only provide an estimate of the Fourier transform-limited duration supported by the pulse spectrum.

A field autocorrelation is recorded when two replicas of a pulse are collinearly superimposed on the sensitive area of a photodiode. If the pulses are superimposed in a non-collinear fashion, it is important to select only a small portion of their wavefront otherwise the visibility of the trace is lowered, or the oscillations may completely vanish. In fact, in this case the angle between the directions of propagation of the two pulses maps different effective delays to different transverse positions on the detector. An example of such non-collinear field autocorrelation is presented in Section 5.3.1 and in Paper **V**.

2.3.3 Second-order interferometric autocorrelation

When the window function is a non-linear process, not introduced by the combination of the intensities of two replicas of the pulse, but by the square of the intensity of the sum of the two fields, a second-order interferometric autocorrelation is performed. Its name originates from the fact that the resulting trace shows phase dependence, as the total intensity decreases when the two replicas are out of phase and decreases when the two replicas are in phase. In this configuration the two fields are recombined prior to the non-linear process (e.g. second-order harmonic generation). The measured photocurrent is proportional to:

$$R_U^{(2)}(\tau) = \int \left|[\tilde{U}(t) + \tilde{U}(t-\tau)]^2\right|^2 dt. \tag{2.6}$$

The total signal is the sum of three terms [50]:

$$R_U^{(2)}(\tau) \propto C_o(\tau) + 4\,\mathrm{Re}\left\{C_1(\tau)e^{i\omega_0\tau}\right\} + 2\,\mathrm{Re}\left\{C_2(\tau)e^{i2\omega_0\tau}\right\},$$

where:

$$C_0(\tau) = \int I^2(t)dt + \int I^2(t-\tau)dt + 4\int I(t)I(t-\tau)dt = 2G_I(0) + 4G_I(\tau),$$

$$C_1(\tau) = \int A^*(t)A(t-\tau)[I(t) + I(t-\tau)]dt,$$

$$C_2(\tau) = \int [A^*(t)A(t-\tau)]^2 dt,$$

and $G_I(\tau)$ is the intensity autocorrelation described in Section 2.3.1. The interferometric autocorrelation is thus the superposition of three components, separated in the Fourier domain: the term $C_0(\tau)$ which does not oscillate and two terms oscillating at frequencies of ω_0 and $2\omega_0$. This oscillatory behavior shows dependence of the autocorrelation on both the phase and amplitude of the two fields.

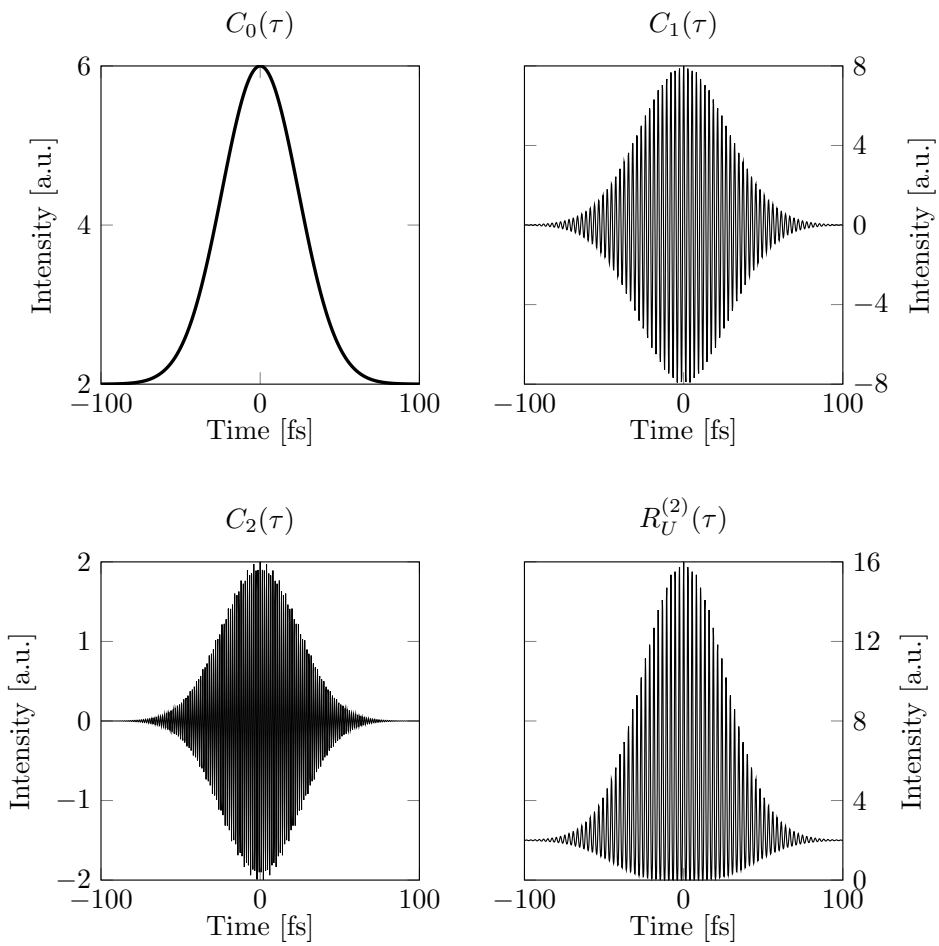

Figure 2.5: Second-order interferometric autocorrelation trace for a Fourier transform-limited 40 fs gaussian pulse.

Figure 2.5 shows how the overall function $R_U^{(2)}$ is bound by an upper envelope whose maximum value, calculated from Equation 2.6, is $16G_I(0)$, and by a lower envelope,

whose minimum value is zero. The asymptotic value, for infinite delays is twice the maximum of the intensity autocorrelation signal $G_I(0)$, giving a non-background-free measurement. The peak-to-background contrast in this measurement is therefore 8:1 [50].

If the acquisition time is sufficiently long, or conversely if the spectral resolution is high enough, the different frequency components ($C_0(\omega)$, $C_1(\omega)$, and $C_2(\omega)$) are well separated and can be resolved. By applying a low-pass filter it is then possible to retrieve the component $C_0(\omega)$, corresponding to the intensity autocorrelation signal, and to estimate the pulse duration as described in Section 2.3.1.

Furthermore, when the intensity profile varies slowly compared to the electric field (this is valid except in few-cycle pulses) the term C_1 is a field autocorrelation of the pulse, and its spectrum can be retrieved by applying a Fourier transform. In addition, the term C_2 is the field autocorrelation of the second harmonic, and the spectrum of the second harmonic can be retrieved from this component in the same way.

2.3.4 Dispersionless autocorrelation

As mentioned above, autocorrelation techniques were developed to overcome the limitation of the slow response of electronic equipment, i.e. photodetectors. On the optical side, most of the typical methods for ultrashort pulse metrology based on autocorrelation rely on some kind of transmissive element, usually a beam splitter and/or a beam recombiner, generally consisting of a thick glass plate.

The propagation of an ultrashort pulse through material introduces dispersion, leading to temporal broadening of the pulse, and in order to perform a reliable measurement it is common to allow the two replicas to propagate through the same amount of material, compensating in one arm for the dispersion introduced by the glass in the other one. This leads to the measurement being carried out on a stretched version of the pulse, with a more or less dramatic effect on the duration of the pulse itself.

As briefly addressed in Section 2.1.1, this problem becomes more relevant the shorter the pulse, and the wider the range of frequencies its spectrum contains. It is crucial to use dispersionless setups (e.g. all-reflective setups, with no transmission optics) to perform autocorrelation, in particular for transform-limited pulses, and especially for sub-femtosecond pulses in the XUV regime where conventional beamsplitters are not available.

In parallel with such autocorrelation-based techniques, a number of other methods have been implemented for ultrashort pulse metrology, based mainly on cross-correlation of the XUV pulse with an IR pulse. An overview of these methods is outside the scope of this work, and the reader is referred to other publications [51, 57–60].

It has been shown that, by using a reflective wavefront splitting device, with the possibility to introduce a tunable delay into one of the two replicas, it is possible to obtain an interferometric autocorrelation trace, giving the same temporal duration as that retrieved with a conventional setup based on a Michelson interferometer, when measuring a 14-fs-long pulse at a central wavelength of 800 nm. In order to implement a nonlinear windowing function, a two-photon-induced current detector was used [61]. A number of other experiments were reported where a dispersionless setup was employed to measure the pulse duration, both in the IR and XUV regime [62, 63].

The concept of a wavefront splitting device will be explained in Section 5.1.1 as its development was central to this work. Tests on a such a device to record autocorrelation traces for IR pulses of different durations are presented in Chapter 5 and in Paper **V**.

2.4 High-order harmonic generation

High-order harmonic generation is a strong-field process that takes place when an atomic system interacts with an electromagnetic field whose strength is comparable to that of the binding force on electrons in the atomic potential. When a high-power laser beam is focused into a gas target with intensities of about $10^{13} - 10^{14}$ W/cm^2, a burst of high-order harmonics is emitted along the direction of propagation of the driving laser beam. Being a highly non-linear process, the efficiency of the HHG process depends on a combination of optimized conditions, both on the micro- and macroscopic levels. As a result of these technical challenges and the lack of a reliable theory, high-order harmonic generation was not observed until 1987 [13, 14].

At that time non-linear optics was well understood in a perturbative framework, and the available theoretical models could only partially explain the observed behavior of the harmonic spectra generated [64]. In fact, the conversion efficiency of only a few lower harmonic orders follows an exponential drop consistent with the order of the process, while experimental spectra showed different regions that could not be explained by the perturbative model [65].

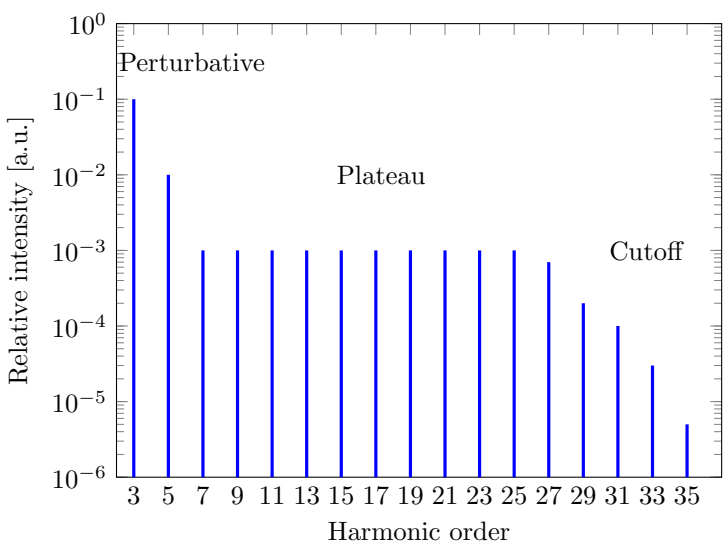

Figure 2.6: Simplified representation of a typical HHG spectrum showing three different regions: perturbative, plateau, and cutoff. Only the odd harmonics of the fundamental field are present.

Figure 2.6 shows a typical HHG spectrum generated by the interaction between a driving pulse and noble gases. Three regions can be identified: first a region cor-

responding to the perturbative regime, where the harmonics follow the behavior of classical low-order harmonic generation, e.g. in a crystal; a plateau, where the conversion efficiency remains constant with increasing non-linear order; and a third, cutoff region where the conversion efficiency falls rapidly over a few harmonic orders. No higher-order harmonics can be generated beyond this region. It was only a few years later, in 1993, that a reliable explanation was proposed [66, 67].

This semi-classical theory, often referred to as the Three-Step Model, can, in principle, explain a variety of strong-field phenomena, but here it will be discussed mainly in connection with HHG, while above-threshold ionization (ATI) will only be briefly touched upon [68]. It should also be noted that a complete quantum mechanical description was reported only a year later [69]. This model, based on the so-called Strong Field Approximation, gives a more accurate description of the quantum effects involved in HHG through evaluation of the time-dependent Schr$\acute{}$odinger equation. In the section below, the semi-classical model is used to describe the interaction between light and matter.

2.4.1 Microscopic response - The Three-Step Model

When a linearly polarized electric field, with a strength comparable to that of the Coulomb potential experienced by valence electrons, interacts with an atomic system, an electron can tunnel out into the continuum, as shown in step 1 in Figure 2.7. The electron is assumed to enter the continuum with an initial velocity of zero and, while in the continuum, its interaction with the ion is neglected as the electric field of the laser dominates.

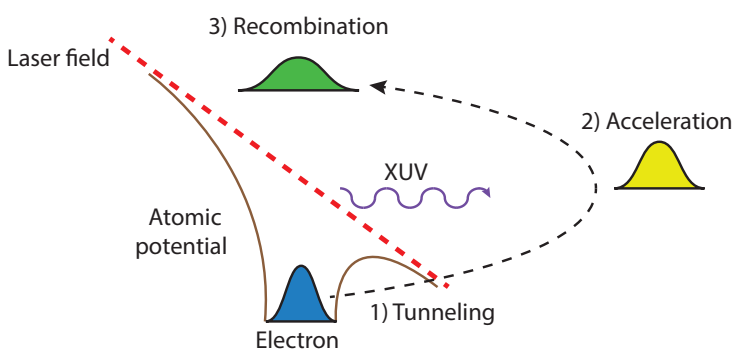

Figure 2.7: Schematic representation of the Three-Step Model: an electron tunnels out of the atomic potential distorted by the laser field (1), is accelerated by the laser field (2), and eventually recombines (3), emitting a burst of XUV photons.

The second step is treated in a purely classical fashion, as the free electron can be accelerated in the continuum by the electric field of the laser pulse (step 2 in Figure 2.7). In the case of a sinusoidal electric field $E(t) = E_0 \sin(\omega t)$, linearly polarized in the x-direction, with amplitude E_0 and angular frequency ω, the electron trajectory along the coordinate x can easily be calculated:

$$x(t) = \frac{eE_0}{m\omega^2}[\sin(\omega t) - \sin(\omega t_i) - \omega(t - t_i)\cos(\omega t_i)],$$

where e is the electron charge and m its mass. The only parameter that influences whether the electron returns to the parent ion or not is the tunneling time relative to the laser field, t_i. It can be shown that, in fact, for $0 < t_i < 0.25T$ (where T is the oscillation period of the driving laser field) the electron never returns to the parent ion. During its excursion in the continuum the accelerated electron acquires energy. If the electron returns to its starting position, it may recombine with the parent ion, in which case a burst of light is emitted (step 3 in Figure 2.7). The energy of the photons emitted is determined by the amount of energy acquired by the electron. Two different kinds of trajectories contribute to the same final energy, namely short and long trajectories, depending on the time spent in the continuum [66]. This is depicted in Figure 2.8 and 2.9.

For a given wavelength and intensity I, it can be shown that the maximum energy transferred to the electron corresponds to $3.17U_p$, where the ponderomotive energy U_p, representing the time-averaged energy acquired by a free electron over a laser cycle, is given by:

$$U_p = \frac{e^2 I}{2m\omega^2\epsilon_0 c},$$

where c is the speed of light in vacuum and ϵ_0 the vacuum permittivity. From simple energy conservation considerations the maximum photon energy that can be emitted is:

$$E_{max} = \hbar\omega_{max} = I_p + 3.17U_p,$$

where I_p is the field-free ionization potential. It is predicted that the emitted photons may have energies ranging from the ultraviolet to the XUV, and in some cases up to the X-ray region [15, 70], which is in good agreement with experimental observations [71].

The fact that the different trajectories originate at different times within the laser cycle allows one or the other type to be favored, for instance, by enhancing or suppressing the driving field with sub-cycle precision [72]. It is known that short and long trajectories exhibit different optical properties, especially in terms of divergence and coherence [73], because of the different phases accumulated by the electron during its excursion in the continuum [74, 75]. The different contributions to the phase of the emitted photons are described in Section 2.4.2.

Another consequence of the dependence of the return energy on the emission and the excursion times, is that photons with different energies are emitted at different times within the cycle. This causes the so-called attochirp, and is illustrated in Figure 2.8. Considering only either short or long trajectories, the resulting pulses exhibit an almost linear positive or negative chirp.

Above-threshold ionization

When recombination does not take place after the second step of the semi-classical model, either because the electron does not return to the parent ion, or because it is

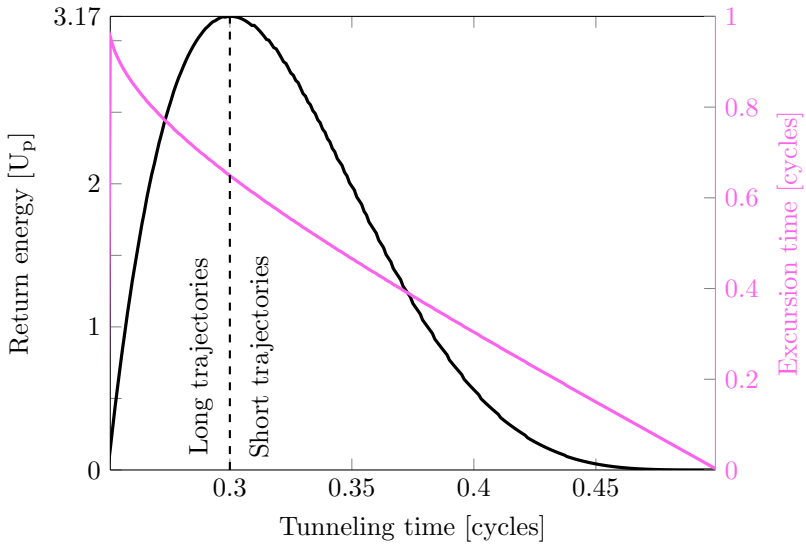

Figure 2.8: Return energy (black) and time spent in the continuum (purple) for electrons emitted at different times within the laser cycle. The dashed vertical line divides the trajectories into long and short.

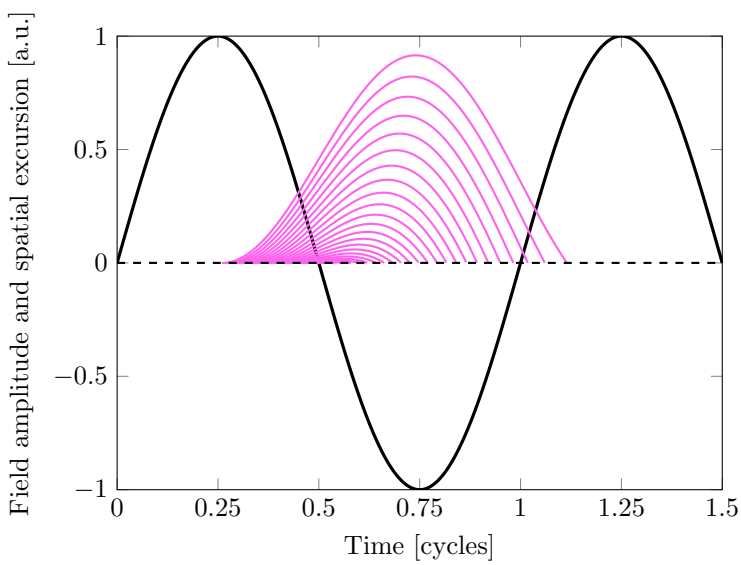

Figure 2.9: Trajectories of the recombining electrons in the continuum (purple). The time axis is defined in units of the driving field cycle (black).

rescattered, ATI can take place. The electron remains in the continuum and is further accelerated by the driving field, thus acquiring more energy. This can be repeated, and it can be shown that the electron can acquire an energy up to 10 U_p. As the oscillatory

motion of the electron has the same periodicity as the driving field, the amount of energy that is transferred to the electron is discrete, and it is a multiple of the photon energy. As a consequence, the resulting spectrum (i.e. the energy distribution) of the electrons that do not recombine exhibits equidistant discrete peaks separated by the energy of the photons of the driving field [68].

2.4.2 Macroscopic effects - Phase-matching effects

Although the emission process relies on the response of a single atom to the driving laser field, the observed emission is the macroscopic coherent sum of the response of an ensemble of different atoms within the interaction region. For this reason, as for any other non-linear optical process, phase-matching conditions must be taken into account in order to maximize the efficiency of the HHG process.

For each harmonic order q, the maximum length over which constructive interference between the radiation generated by different atoms takes place is called the coherence length: $L_{coh,q} = \pi/\Delta k_q$. It depends on the mismatch vector $\Delta k_q = qk_f - k_q$, where k_f is the wavevector of the fundamental laser field and k_q is that of the qth order harmonic. The vector notation has been dropped here, indicating that only on-axis terms are considered. In order to maximize the coherence length, and thus improve the efficiency of HHG, the mismatch vector must be minimized. In other words, the light generated by one emitter must maintain the same phase relation to the driving field when it reaches the next emitter, so that this emission will add coherently to the previous one. In fact, the overall conversion efficiency can be limited by the destructive interferences arising from out-of-phase generation in different atoms.

Previous studies have shown that the mismatch in the generation process depends on different parameters during the generation process [75–80]. Four main contributions were found to be relevant, and the wavevector mismatch can thus be expanded as:

$$\Delta k_q = \Delta k_g + \Delta k_n + \Delta k_p + \Delta k_d.$$

The first contribution, Δk_g, is related to the geometrical phase, and originates from the gaussian beam phase along the propagation direction, or Gouy phase, and it is always negative (see section 2.1.1). The second and third terms, Δk_n and Δk_p, are related to the dispersion arising from propagation in a neutral medium and in a free-electron plasma, and they are positive and negative, respectively. The final contribution, Δk_d, is dependent on the dipole phase, and is proportional to the intensity gradient. This phase mismatch arises from the propagation of the electron in the continuum, and its magnitude depends on the excursion time. Because of this, the contribution of the dipole phase is greater for the long trajectories. Δk_d is positive at positions located after the focus of the driving IR beam, and negative before the focus.

A complete description of the phase-matching condition would require comprehensive knowledge of the electric field and the gas density distribution in the entire interaction volume, as the four individual contributions vary at each point in space. Furthermore, some of the contributions are dependent on the intensity of the laser and the free-electron density, which also vary in time, thus making the phase-matching conditions dynamic.

In the case of a loose focusing geometry, the dipole phase can be considered constant as the longitudinal intensity gradient is small. It can be shown that in this scenario, for a specific focusing geometry, the neutral dispersion can be used to cancel out the Gouy phase mismatch and the plasma dispersion, provided that the degree of ionization of the medium is not too high. In fact, as the intensity increases, so does the degree of ionization and the plasma contribution, which are proportional to each other. If the latter dominates over the neutral dispersion it is not possible to achieve efficient phase-matched generation. Intuitively, this means that, in order to generate harmonics efficiently and to employ a driving field with higher energy, the intensity should be kept constant by adopting a looser focusing geometry. This may lead to a higher energy of the generated XUV pulses, if the generation volume is also increased. Furthermore, it is possible to show that, for a certain generation geometry, there is a pressure at which the volume over which phase-matched generation takes place, is maximized.

2.4.3 Scaling the focusing geometry

In the previous section, a means of experimentally determining a local maximum of the conversion efficiency was suggested. The generation process can be optimized by adjusting the generation gas pressure, for any given set of the other parameters. The other experimental parameters that can be varied are the focal length, f, of the focusing element, the beam diameter, D, (combined to form the f-number $f_{\#} = f/D$), the pulse duration, the pulse energy, the focal position, and the gas pressure.

Despite knowing that an absolute maximum exists in the parameter space, a thorough scan of the whole space is tedious and time consuming. It can be shown that instead, starting from a given set of generation conditions, the conversion efficiency can be maintained when changing one parameter and scaling the others accordingly, in order not to move away from the conditions for phase-matched generation. Following gaussian optics considerations [80], it is possible to derive the following scaling relations for phase matching pressure, length of the generation medium, and energy of the driving pulse:

$$\begin{aligned} p_{match} &\propto 1/f_{\#}^2, \\ L_{med} &\propto f_{\#}^2, \\ E_f &\propto f_{\#}^2. \end{aligned}$$

At the same time, the energy of the generated harmonics scales as $E_h \propto f_{\#}^2$.

In practice, starting from an already optimized situation, where the phase matching condition is met for the largest possible generation volume, an increase of a factor of two in the focal length will result in a gain in harmonic energy of a factor of four, if the other parameters are properly scaled.

It is important to bear in mind that rigorous scaling requires the intensity distribution within the generation volume to be scaled-up in space, while not affecting the temporal structure. Furthermore, parameters such as the relative position of the focal plane with respect to the generation medium should not be varied.

2.4.4 Towards isolated attosecond pulses

While APTs carry all the energy that has been converted in XUV photons during the HHG process, their relatively long overall pulse duration, modulated by the individual attosecond pulse structure, might lead to a descrease in temporal resolution in a pump-probe experiment and their periodic structure could give rise to complex signals. Intuitively, when the delay between the pump and the probe pulses matches n times the temporal spacing of the pulses within the train, the pump pulse overlaps its nth neighbor, and at these delays the signal will exhibit a local maximum. In other words the desired signal is convoluted with a periodic signal, whose period is twice that of the fundamental field.

In order to perform a "clean" attosecond pump-probe experiment, isolated attosecond pulses (IAPs) are required. Several schemes have been reported for the generation of IAPs to date, and they can be categorized into four types, depending on the principle on which they rely [58, 81–83].

- **Spectral gating -** These techniques achieve spectral selection by, for example, metallic filters. As the generated cutoff is intensity-dependent and varies at each half cycle, the spectral components arising from the generation within only the most intense half cycle of the driving pulse can be isolated. The resulting spectrum is continuous, and the temporal profile of the XUV is that of a single pulse. This kind of spectral gating is called amplitude gating [12, 35, 84].

  Ionization gating is an extension of amplitude gating [85–87]. When the intensity on the leading edge of the pulse is already well above the ionization threshold, the electric field ionizes the generation medium to a degree where HHG is hindered in the following cycles. In principle, the resulting emssion is confined to only one half cycle. In practice, especially for many-cycle pulses, the first cycle during which HHG can take place might not have sufficient intensity to strongly ionize the medium. For this reason, subsequent spectral filtering is required, in a similar fashion to the amplitude gating scheme. Furthermore, both of these techniques rely on that the same intensity is reached at the same cycle in consecutive IR pulses, and therefore require stability of the carrier-envelope phase [88].

- **Temporal gating -** The aim of these techniques is to control the polarization of the driving field on a sub-cycle level. The HHG efficiency is very sensitive to the ellipticity of the driving pulse, and a small deviation from perfectly linear polarization induces transverse acceleration of the electrons in the continuum, dramatically decreasing the probability of recombining with the parent ion. If the driving laser pulse is circularly polarized at all times apart from the central half cycle, only one XUV pulse is emitted with a continuous spectrum, leading to an isolated pulse [37, 89, 90]. This is called polarization gating, and it can be extended to a similar technique called double optical gating [91–93]. In this scheme an additional second-harmonic pulse with the same polarization configuration co-propagates with the driving pulse. The effect of the second harmonic is to break the field symmetry, confining the emission of XUV photons to the central cycle, rather than only half of it. This allows for higher intensity of the driving pulse to be utilized, thus leading to higher XUV yields.

- **Spatio-temporal gating -** Two similar approaches exploit spatio-temporal couplings in the driving pulse, especially rotation of the wavefront. For a thorough description of this effect the reader is referred to other publications [94, 95]. For the sake of this discussion, rotation of the wavefront during propagation of a pulse leads to the XUV pulses generated being propagated in different directions.

  This effect is employed in both the so-called attosecond lighthouse and non-collinear optical gating (NOG) [96] to generate individual attosecond pulses that are intrinsically separated in space, and simple spatial discrimination leads to isolated attosecond pulses. The main difference between these two approaches is that in a non-collinear scheme the XUV pulses are already separated in space from the driving IR pulse, avoiding the need for metallic filters for spectral discrimination.

  The concept of NOG was developed in Lund, and its proof-of-principle led to Paper **IV**.

- **Two-color generation -** This approach allows for the generation of an IAP even with relatively long driving IR pulses. By adding an incommensurate wavelength to the driving field (e.g. 1300 nm to a 800 nm driving field) it is possible to reshape the IR field in such a way that only one isolated attosecond pulse is generated [97].

Chapter 3

High-Power High-Order Harmonic Generation

This chapter introduces the experimental setup that was used throughout this work, as well as the steps taken to optimize the HHG process, to reduce the pulse duration (by broadening its spectrum), and to move towards the generation of IAPs. The author was involved in all of these efforts to different extents.

Immediately before the author's work started, a major rebuilding took place at the Lund Laser Centre, expanding the available laboratory space and leading to the possibility of developing a 15-meter-long beamline in order to accommodate very loose focusing geometries in the HHG setup. It also allowed the addition of an application end-station, which will be described in the next chapter.

Several upgrades have also been implemented over the past few years. This chapter describes only the current setup, but highlights the changes in certain components when it is necessary for the understanding of the setup used to conduct experiments leading to the publications.

3.1 The Lund high-intensity XUV beamline

The high-intensity XUV beamline at the Lund High-Power Laser facility is driven by a Ti:sapphire chirped pulse amplification terawatt laser, the main laser system of the Lund High-Power Laser Facility since its inauguration in 1992 [98]. It delivers pulses to a high-power arm, carrying an energy per pulse as high as 1.5 J and reaching peak powers of about 40 TW at a central wavelength of 800 nm. The low-power arm, used to drive the high-intensity XUV beamline, delivers pulses with energies as high as 250 mJ.

3.1.1 The laser system and beam preparation

The first component is an oscillator producing pulses at an 80 MHz repetition rate with a spectral bandwidth of about 60 nm. A combination of a Pockels cell and a Glan-Taylor polarizer reduces the repetition rate to 10 Hz directly after the oscillator, before reaching the amplification stages. Initial amplification is achieved with a multipass preamplifier, after which a precompensation for high-order dispersion is applied by means of an acousto-optic programmable dispersive filter [99]. The pulses are then stretched to a few hundreds of picoseconds in order to prevent them from damaging the gain medium in the next amplification stage. Amplification is first performed in a regenerative amplifier, and then in a multipass amplifier pumped by two Q-switched Nd:YAG lasers, before being sent to the HHG beamline, located in another room.

An energy of about 220 mJ per pulse is routinely available at the output of the low-power arm. This beam is then focused by a 1.7 m focal length lens into a conical pinhole with an aperture of 400 µm in order to filter out high spatial frequencies, and then recollimated in a 1:1 confocal telescope configuration. After spatial filtering, a combination of a rotatable half-wave plate and a Brewster angle polarizer is used as a variable energy attenuator. The half-wave plate is mounted on a motorized, remotely-controlled rotating mount. The beam is then expanded to a diameter of 35 mm before being sent to the grating compressor. Compression narrows the pulses temporally to 35 fs (measured by means of a commercial intensity autocorrelator, see Section 2.3, and a d-scan setup [100]). Pulses with an energy as high as 80 mJ are then sent to the harmonic generation gas cell. The beam is fully enclosed in boxes and tubes in order to reduce fluctuations due to ambient air-flow, which could damage the spatial filter and reduce the overall stability of the beam.

At the time of writing, a different beam transport scheme is being implemented. The aim of this upgrade is to propagate the beam from the laser output to the input of the compressor under vacuum, in order to further decrease pointing fluctuations, which are detrimental to our experiments, as will be discussed in Chapters 4 and 5.

After the compression stage, right before entering the vacuum apparatus, the size of the beam can be reduced by means of a motorized iris. The beam is then focused into the generation gas cell. Various focusing geometries were employed throughout the course of this work, depending on the requirements of the different experiments. Table 3.1 presents a summary of the different focusing geometries adopted.

Paper	Focusing element	Focal length
I	Lens	4 m
II	Lens	8.7 m
VII, **VIII**	Lens + DM	8.7 m
III	Mirror	2 m
Upgrade	Mirror + DM	8 m

Table 3.1: Different focusing geometries utilized for the experiments. DM: deformable mirror.

Although the general purpose of the beamline was to take full advantage of the available energy of the IR pulses, and for this reason the focal length has been increased over time, the experiment presented in Paper **III** required a shorter focal length. This is because the throughput of the setup suffers from high losses, and a shorter focal length is required in order to achieve the intensity needed for HHG.

More recently, a deformable mirror (DM) has been installed in the beamline. This is a dielectric mirror with 32 actuators able to deform the reflecting surface with a precision of $\lambda/20$, or better. The objective is twofold: to compensate for aberrations in the driving IR beam (see Section 2.1.1), and to finely tune the focal position with respect to the generating medium.

In fact, it is possible to operate the DM in combination with an IR wavefront sensor. This commercial device is routinely used to assess the wavefront quality in the generation volume. A thorough description of this device is provided in Ref [101]. A description of the XUV analog is provided in Section 4.2.

By fine-tuning the individual actuators of the DM it is possible to reshape the wavefront in order to ensure its flatness in the focal plane by compensating the pre-existing aberrations and those introduced, e.g., by misalignments in the focusing components. The actuators can also be collectively tuned in order to change the macroscopic curvature of the mirror, thus changing the compound focal length. This provides a high degree of flexibility: in fact, we estimated that the combination of this DM with an 8 m focal length mirror should result in focal lengths ranging between 5 m and 20 m.

3.1.2 The high-order harmonic generation and diagnostic setup

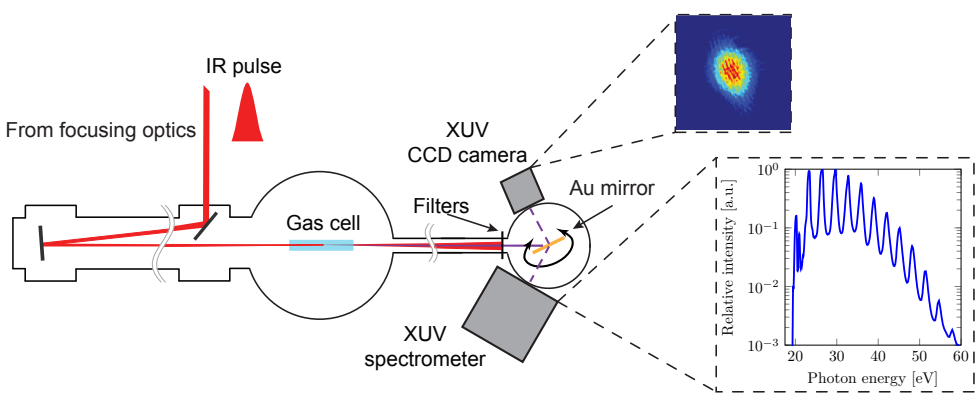

Figure 3.1: Schematic illustration of the HHG and diagnostic setup.

Figure 3.1 presents a schematic of the HHG setup. At the input of the setup, the compressed pulses are focused into the generation gas cell, which was designed by the author with the intention of maintaining the maximum degree of flexibility. The length can be varied between 30 mm and 150 mm, in 15-mm steps. Furthermore, it can be filled with gas statically, or in a pulsed manner through a commercial piezo-driven valve. The gas cell is mounted on a 4-axis stage, allowing linear movements in the xy-plane and tilting around the x- and y-axes (z-axis being the propagation

direction). Two gas cells can be installed in the generation chamber, either in parallel or in series [72]. In the experiment reported in Paper **I**, the gas cell used was 20 mm long and filled with Ar or Ne in a pulsed fashion. The piezo-driven valve was actuated at a repetition rate matching that of the laser, and synchronized to the arrival of the IR pulse. In other experiments described in this thesis, the gas cell was 60 mm long and statically filled, apart from the experiment described in Paper **VII**, where it was operated in pulsed mode.

After the generation chamber, the harmonic beam, co-propagating with the driving IR beam, reaches the next chamber, which contains the beam diagnostics. One or more metallic filters can be inserted in the beam path before the diagnostics chamber (via a manual manipulator), to block the IR radiation which would damage the sensitive detection equipment.

A gold-coated mirror is mounted on a remotely controlled rotation stage in the center of the diagnostic chamber. This mirror is used to reflect the beam and direct it to one of the two photon detectors in the chamber: an XUV spectrometer or a CCD XUV camera. Optionally, the beam can be sent outside the chamber through a window for alignment purposes, or any other side experiment. An example of an alignment procedure using this option is given in Section 5.1.4.

The flat-field grating spectrometer (Jobin-Yvon PGM-PGS 200) consists of a horizontal entrance slit, which is imaged by a toroidal mirror onto the back surface of a microchannel plate (MCP)/phosphor screen assembly. Spectral discrimination is provided by further reflection from a grating. The phosphor screen thus shows the XUV spectrum, spatially resolved in the lateral direction, and spectrally resolved in the vertical direction. It is possible to acquire XUV spectra by imaging the screen with a camera. The inset in Figure 3.1 shows a typical spectrum generated in Ar.

The XUV camera (Andor iKon-L) employs an energy-calibrated CCD chip. The sensor provides both the spatial intensity distribution of the impinging beam (single- or multi-shot), and a measurement of the integrated energy. By combining the information from this camera with a spectrum, it is possible to obtain the energy generated per harmonic. This is done by correcting the measured energy for the calculated reflectivity of the gold mirror, the estimated transmission of the metallic filter(s), the spectrometer response, and the efficiency of the camera. This is a fairly complicated procedure that leads to rather large uncertainties in energy estimation. The inset in Figure 3.1 shows a typical far-field profile of the harmonic beam.

3.2 HHG experiments

As mentioned out in the introduction, high XUV intensities are needed to perform non-linear experiments in atoms and molecules. Such high intensities can be achieved in three main ways.

- Maximizing the energy carried by each pulse, which can be achieved by ensuring the highest possible conversion efficiency in the HHG process, regarding both the single-atom response and the macroscopic phase-matching effects. The reflection/transmission losses in the beam transport chain should also be minimized.

- Generating and preserving a large XUV bandwidth which leads to short pulses: actively, by applying IR pulse post-compression schemes, and passively, by choosing appropriate XUV optics that do not limit the pulse bandwidth.
- Opimizing the focusing conditions.

The first two approaches can be combined into one: namely the generation and preservation of high-power broadband XUV pulses. The third will be addressed in the next chapter.

3.2.1 Yield optimization

In the experiment presented in Paper **I** an automatic scanning routine was used to optimize HHG in a loose focusing geometry. By scanning a four-dimensional parameter space it is possible to find several local maxima, as well as the absolute maximum achievable. The experimental parameters that could be varied were: driving pulse energy, beam diameter, gas pressure (actuated by a piezo-driven valve, thus with variable opening time), and the position of the gas cell relative to the focus (by translating the cell). The experiment demonstrated the possibility of achieving phase-matching conditions over a large bandwidth, in both Ar and in Ne. The acquired spectra exhibit a cutoff energy of 45 eV for Ar, and 91.5 eV for Ne.

The optimal generation conditions were found to be a beam aperture of 10 mm and a pulse energy of 20 mJ, thus leading to a peak intensity of 3×10^{14} W/cm^2 in the focus. Given the loose focusing configuration, this intensity is approximately constant in the generation medium, which was 20 mm long.

The energy generated per pulse was estimated from the measured spectra and harmonic beam energy, and found to be on the microjoule level. It was later found that the manufacturer of the energy-calibrated CCD camera had provided incorrect calibration curves, and omitted an efficiency curve. Accurate a posteriori evaluation of the overestimation of the energy generated would have required precise knowledge of the spectral transmission of the filters utilized, which was not done during the experiment. For these reasons the energy of the XUV pulses has been measured in the focus during following experiments.

Leading up to the experiment presented in Paper **II**, the focusing geometry was extended in an attempt to utilize more of the available IR pulse energy (see Table 3.1). To rigorously scale up the geometry according to the relations presented in Section 2.4.3, while maintaining the same generation conditions as in the previous experiment, it would be necessary to concentrate the entire available energy in a small beam (10 mm), which was not possible. In fact, in the used setup, the adjustment of the beam size, performed by clipping the size of the field with a variable aperture, is not independent of the pulse energy. On the other hand, if the full pulse energy were used to drive the HHG process, the resulting peak intensity would exceed 10^{15} W/cm^2 which would lead to a high degree of ionization in the gas medium, thus rendering the HHG process inefficient (see Section 2.4.2).

For this reason, the best generation conditions were found when the position of the focus was about 50-100 cm after the gas cell, thus resulting in a peak intensity in the range of 10^{14} W/cm^2, for a driving pulse energy of 80 mJ, and a beam diameter of 30 mm. The looser focusing configuration allows for efficient phase-matching over

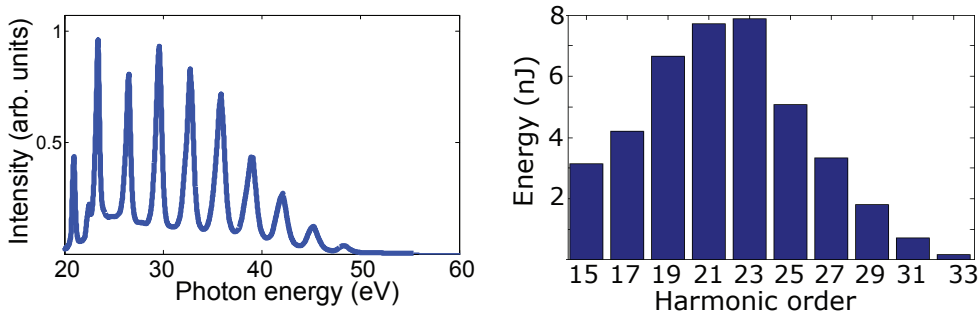

Figure 3.2: Spectrum generated in argon (left) and energy on target per harmonic (right). Reproduced from Paper **II**.

a longer distance, and this was the reason for increasing the length of the gas cell to 60 mm.

The left panel of Figure 3.2 shows a typical spectrum generated in Ar, and the right panel shows the energy per harmonic in the focus during this experiment. The spectrum shown is corrected for the response of the optical elements in the beam path to the spectrometer (including aluminum filters). By acquiring an image with the calibrated XUV camera, it was possible to estimate an energy per pulse approaching one microjoule. The energies shown in the right panel of Figure 3.2 were calculated by combining this measurement with the recorded spectrum, and assuming a theoretical reflectivity of 46% of the focusing optics. The resulting total energy in the focus was estimated to be about 40 nJ.

3.2.2 Generation of shorter pulses

The aim of the experiment described in Paper **III** was to reduce the duration of the driving pulse by means of spectral broadening and further recompression, in order to increase the intensity compared to a longer driving pulse carrying the same energy. During this experiment the uncompressed pulses were focused into a hollow planar waveguide by means of a cylindrical mirror, and later recollimated with another cylindrical mirror. This waveguide was filled with argon in order to exploit its non-linear response (Kerr effect), which gives rise to spectral broadening, potentially leading to shorter IR pulses. In order to utilize the full extent of the broader spectrum, a chirp-mirror compressor was implemented, and its output was focused into the generation gas cell with a 2-m focal length lens.

The results showed a four-fold increase in the spectral bandwidth and a reduction in the pulse duration of about three times, down to less than 15 fs. Due to the limitations of the setup employed, only 20 mJ were available for HHG. Figure 3.3 shows a comparison between the spectra generated in two cases: when the post-compression setup was by-passed (blue curve) and when the beam was sent through the post-compression setup (red curve). It is clear that the higher driving intensity leads to a significant extension of the cutoff, as well as increased continuity of this spectral region. The inset in Figure 3.3 shows the spatially resolved generated spectrum. A

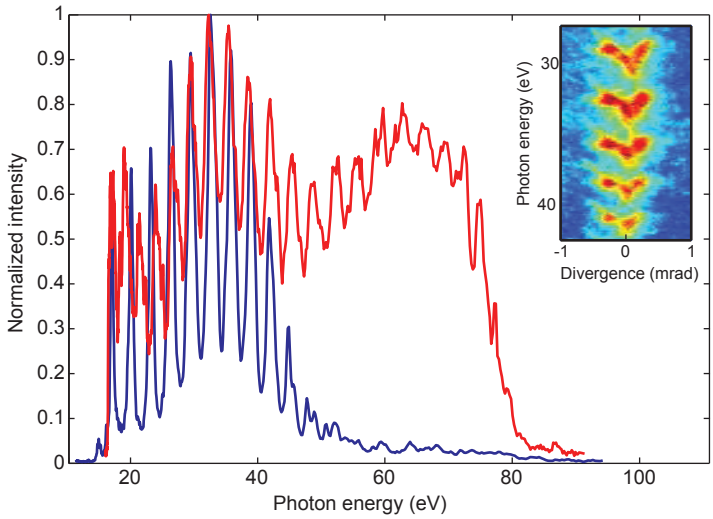

Figure 3.3: Spectra generated in argon with the same pulse energy of 20 mJ. The blue curve is the spectrum generated with 45-fs pulses, and the red is that generated with post-compressed pulses with a duration of 13.6 fs. The inset shows the spatially resolved generated spectrum. Reproduced from Paper **III**.

blue-shift can be seen in the central part, probably due to higher non-linearities arising from the uneven spatial profile of the post-compressed beam.

This experiment demonstrated the viability of this post-compression scheme for driving IR energies exceeding the microjoule level, whereas other methods such as hollow-fiber compression are currently limited to that level [102, 103].

Chapter 4

Micro-focusing end-station

This chapter describes the setup used to focus the short, energetic XUV pulses into a tight spot to achieve high intensities. It also presents the experiments performed with the aim of optimizing the focusing conditions, and therefore the peak intensity (see Section 4.4).

These experiments are carried out in the application chamber, which is shown in Figure 4.1 both as a sketch and a photograph. This chamber was designed to host high-intensity non-linear photoionization experiments in atomic and molecular target systems, in the gas phase. For this reason, it is designed for ultra-high vacuum pressures.

4.1 Application chamber

Three main operations are to be performed in the application chamber: injection of the sample to be probed in the gas phase, focusing the XUV pulses in the sample, and detection of the products of the non-linear process under investigation. The gas is injected by means of a pulsed valve, described in Section 4.1.1, the focusing optics are discussed in detail in Section 4.3, and the detectors are described in Section 4.2.

4.1.1 Even-Lavie valve

The pulsed valve installed on the application chamber is an Even-Lavie valve [104]. The aperture is regulated by a magnetic plunger driven by an electro-magnetic coil that allows the aperture time and the repetition rate to be tuned. When the valve is open, high-pressure gas flows into the chamber through a series of two conical skimmers. The passage of the gas through the skimmers creates a dense collimated jet, characterized by supersonic velocities. Additionally, a small cylinder is placed on the outer side of the valve and can be filled with a liquid or solid sample. By heating the cylinder, it is possible to evaporate the sample so that the atoms are carried into

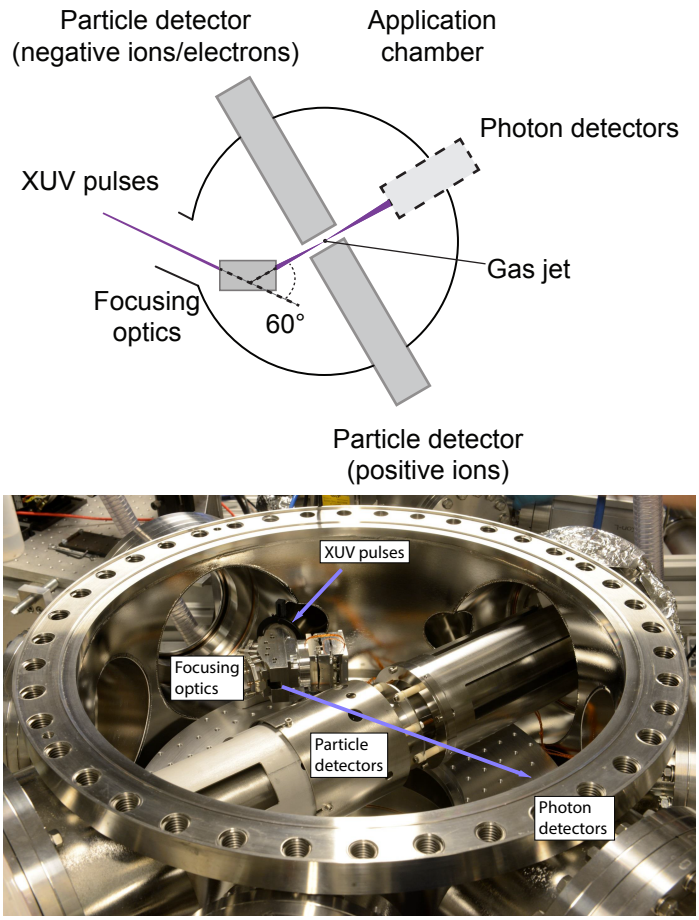

Figure 4.1: Sketch (above) and photograph (below) of the application chamber.

the experimental region by the molecules of a noble gas, typically helium. Figure 4.2 shows a photograph of the Even-Lavie valve mounted on a flange.

4.2 Photon and particle detectors

There are several diagnostic tools in the application chamber to detect either photons or particles. The photon detectors are placed in the beam path, while the particle detectors are designed to extract the particles originating from the interaction between the IR or XUV beam and the gas, in the direction transverse to the direction of propagation of the beam. The photon detectors are: an XUV photodiode, an XUV CCD camera, and an XUV microscope.

Figure 4.2: Photograph of the Even-Lavie valve.

4.2.1 XUV photodiode

The photodiode is calibrated to measure the energy of the incident XUV pulses and is placed directly after the focus. It allows for the acquisition of single-shot information about the energy of the pulses reaching the focus, thus not requiring to assume the reflectivity of the optical components in the beam path between the point where the energy is measured and the focal region. This single-shot information is particularly useful when there are energy fluctuations between each shot of the driving IR laser, which are then magnified by the high non-linearity of the HHG process. It is necessary to correct for such fluctuations when a partial covariance analysis method is applied, as discussed briefly in Chapter 6. The photodiode is installed on a manual actuator in a way that it can be moved out of the beam path, thus allowing the XUV pulses to reach other detectors, or it can be used to block the beam.

4.2.2 XUV CCD camera

The CCD camera is the one described in Section 3.1.2 as part of the diagnostic setup. It can be installed after the focus in the application chamber with several purposes: to record the intensity profile of the beam after the focus, to measure the energy of the XUV pulses, and to evaluate how the XUV beam is split by the wavefront splitting device described in Chapter 5. Chapter 6 presents a brief discussion of the effects of uneven splitting ratios on time-resolved experiments. The same chapter also provides an outlook of the intended use of this detector in the near future.

4.2.3 XUV Microscope

An XUV microscope was developed to acquire an image of the intensity distribution at the focus. The XUV radiation is converted into visible light at a wavelength of 550 nm by a Ce-doped yttrium aluminum garnet (Ce:YAG) scintillation crystal [105, 106]. The emitted luminescence is imaged onto a CCD camera, cooled to -40 °C, by an optical system composed of an infinity-corrected objective (Mitutoyo M Plan Apo 100×), a tube lens, and a relay lens working in 2f-2f configuration. The crystal is

clamped to a thin fused silica window in vacuum, while the imaging system with the camera is outside the vacuum chamber. The field of view of the system is estimated to be 50 µm, and the resolution is approximately 2 µm. The microscope cannot be operated at the same time as the particle detectors because the scintillation crystal must be placed in the focal plane, and the size of the window it is clamped to is greater than the separation of the electrodes of the particle detector.

The microscope was used to characterize the intensity distribution in the focal plane. The first results are reported in Paper **II** and were used to estimate the intensity available in the interaction region. The focal spot was measured and found to be 11 µm × 16 µm, full-width at half-maximum (FWHM), as shown in Figure 4.3. Knowledge of this size and the assumption of the duration of the XUV pulse led to the estimation of peak intensities as high as 3×10^{12} W/cm^2. The measured focal distribution was compared to a raytracing simulation, and the latter predicted a circular intensity distribution in the focal plane with a diameter of about 4.5 µm at half-maximum. The raytracing simulation was consistent with simulations provided by the manufacturer, which predicted a FWHM size of 4.2 µm. The disagreement between the experimental findings and the two simulations was attributed to aberrations introduced by not perfect focusing and to non-ideal optics, especially in terms of surface flatness.

During the experiments reported in Paper **VIII** the performance of the microscope was assessed more carefully, and compared to back-propagation of wavefronts recorded with the sensor described in Section 4.4. Back-propagation provided a result consistent with the simulations, and an analysis of the optical setup of the microscope revealed the presence of spherical aberrations that affected the estimated resolution. Furthermore, during the first experiments, the data were collected by the accumulation of several shots since the camera employed at the time was not sufficiently sensitive for the acquisition of single-shot data. In that case, each shot of the laser was recorded at a different position due to pointing fluctuations, which leads to blurring of the image. The images recorded by means of the microscope should thus be considered an estimate of the upper-limit, and thus the estimate of the intensity provides a lower-limit. Another limitation on the reliability of the microscope in measuring the intensity distribution at the focus is that, when this setup is installed in the focal region, none of the other detectors can be operated, thus making the optimization of the alignment of the focusing optics more complicated and less precise. It is therefore difficult to compare the results obtained with the microscope to the results obtained through back-propagation of a wavefront.

4.2.4 Particle spectrometer

The particle spectrometer is shown in Figure 4.4. The charged particles (electrons or negative ions, and positive ions) created by photoionization events are extracted from the interaction region by the electric field generated by a series of parallel electrodes whose axis of symmetry is perpendicular to the direction of the propagation of the photons. The fragments enter either of the flight tubes and reach the front surface of an MCP/phosphor screen. Different properties of the fragments can be observed, depending on the combination of the voltages applied to the electrodes and to the flight tubes. Two main observables: the time of arrival of the particles, and the position on the screen, are given by this kind of detector.

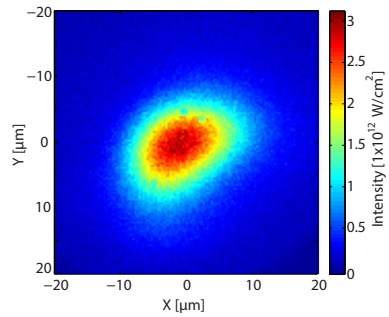

Figure 4.3: Intensity distribution in the focal plane, showing a size of 11 µm × 16 µm FWHM. Reproduced from Paper **II**.

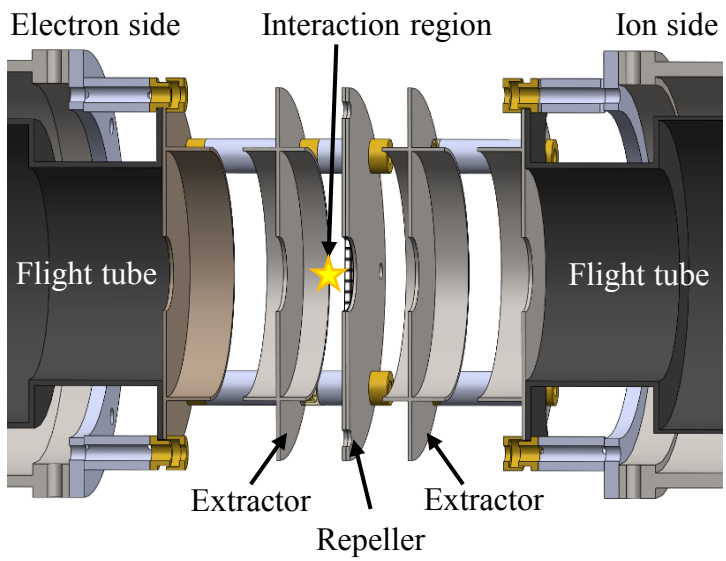

Figure 4.4: 3D illustration of the particle detector. Electrons and negative ions are repelled and extracted on one side (left in the figure), while positive ions are extracted on the other side (right in the figure). Reproduced from Paper **VII**.

If the voltages are set in such a way that the time of arrival of the particles is independent of where they originated within the interaction region, the spectrometer is called a Wiley-McLaren time-of-flight (TOF) spectrometer [107]. The time at which the particles arrive at the back surface of the MCP depends only on the ratio between their mass and their charge. The resulting trace is then called a TOF spectrum, and it is useful in the estimation of which fragments are produced in the photoionization process.

It is possible to detune the voltages of the electrodes so that the time of arrival depends on both the mass/charge ratio and on the lateral position of the origin of the charged particles. This is useful when knowledge of the lateral position is important, as in the case of the alignment procedure described in Section 5.1.4.

The voltages applied to the electrodes can be set in such a way that the distribution of the transverse component of the momentum is mapped onto the position of arrival on the MCP. The position of the impact on the phosphor screen is then acquired with a sensitive camera. If the studied system has an axis of cylindrical symmetry along the axis of the detector, it is possible to retrieve the initial three dimensional distribution of the momentum using a numerical algorithm. For these voltages the spectrometer is called a velocity mapping imaging (VMI) spectrometer [108]. Such spectrometers are employed in a wide range of experiments, typically to detect either positive ions or electrons. The development of a double-sided VMI spectrometer able to detect both ions and electrons at the same time is reported in Paper **VII**.

It is possible to operate the VMI spectrometer in the so-called spatial mode [109]. A particular combination of voltages applied to the electrodes ensures that the position of arrival of the particles at the MCP depends on their initial position, and not on their initial momentum. In practice, this mode allows the interaction region to be projected onto the phosphor screen, which is particularly useful for alignment purposes. An example of an alignment procedure where this mode has been employed is described in Section 5.1.4.

This detector can be operated in TOF mode, single VMI mode, double VMI mode, or a combination of these, e.g. double VMI+TOF mode. In this configuration the TOF spectra suffer only minor degradation in terms of resolution, as reported in Paper **VII**.

4.3 XUV focusing optics

When performing a non-linear broadband experiment, the focusing element is of the utmost importance. The goal is to focus pulses down to the smallest possible spot, while maintaining the broad bandwidth, so as not to elongate the temporal structure of the pulses. Bearing this in mind, the natural choice is to use metallic optics in a grazing incidence configuration, as argued in Section 2.2.2. At the same time, it is important to minimize the number of reflections, due to the low reflectivity of optics in the XUV regime. For this reason, the decision was taken when designing the layout of the end-station not to recollimate the harmonic beam generated prior to re-focusing, but to image the generation volume placed 6 m behind the focusing optics into the gas jet placed 170 mm after the focusing optics. This leads to a considerable demagnification exceeding 35, which not only leads to a focus of a few micrometers, but also reduces the effect of pointing instabilities.

Another constraint when choosing the focusing geometry was imposed by space limitations, and a large angle of deflection was desirable. On the other hand, large angles of deflection imply small angles of normal incidence, thus yielding lower reflectivities. The trade-off was to introduce a deflection of 60°, as shown in the sketch in Figure 4.1.

4.3.1 Ellipsoidal and toroidal mirrors

The ideal shape of a mirror for an imaging configuration is an ellipsoid, but in practice ellipsoidal mirrors have several drawbacks. An ellipsoid is a surface of revolution

generated by the rotation of an ellipse about one of its axes of symmetry. To explain the working principle of an ellipsoidal mirror (commonly also referred to as elliptical mirror), it is sufficient to consider an ellipse, for the sake of simplicity.

While rays originating in the first geometrical focus of an ellipse converge perfectly in the second focus, those whose origin is displaced from the first focus converge at different locations from the second focus and experience a marginally different radius of curvature and, therefore, focal length. This happens in realistic cases when the source is not a point. These non-idealities give rise to strong coma aberrations [110].

The Abbe sine condition states that, in order to eliminate coma aberrations, the principal surface must be perpendicular to the rays themselves [110]. The principal surface is defined as the surface on which the rays in the object space, when traced forwards, intersect the corresponding rays in the image space traced backwards. In the case of a single mirror in a grazing incidence configuration, the principal surface is the mirror itself and the rays are nearly parallel to it. Other limitations that hinder wide-spread use of elliptical mirrors are the high manufacturing costs due to the lack of standard tools to ensure high surface quality and flatness, and the tedious alignment procedure.

Locally, the best approximation of an ellipsoidal surface is a toroidal one, which has the advantage of being easier to manufacture, and it also allows the radii of curvature in the tangential and the sagittal planes to be set independently. The tangential plane is the plane containing the optical axis (which is defined as the path taken by the central ray of the propagating beam) and the normal to the reflecting surface, while the sagittal plane contains the optical axis and is perpendicular to the tangential plane. The two radii are tuned in such a way that the resulting focal lengths are matched in order to eliminate the astigmatism arising from a spherical surface in a grazing incidence configuration. In fact, the focal lengths in the two planes are defined by:

$$f_T = \frac{R_T \sin\theta}{2}, \tag{4.1}$$

and

$$f_S = \frac{R_S}{2\sin\theta}, \tag{4.2}$$

where R denotes the radius of curvature and the indices T and S refer to the tangential and the sagittal planes, respectively. θ is the grazing angle of incidence [110]. Although toroidal mirrors are more practical, a single one would suffer from the same aberrations as elliptical mirrors, since they are unable to satisfy the Abbe sine condition. However, a combination of two toroidal mirrors can fulfill all the requirements for high-intensity broadband experiments, as shown in the following section.

4.3.2 Wolter optics

In the 1950s, Wolter demonstrated that certain combinations of confocal conic sections of revolution lead, to some extent, to aberration-free systems [111] by satisfying the Abbe sine condition. Is it important to note that a toroidal surface is not a conic section, therefore a combination of two toroidal mirrors is a "Wolter-like" configuration, but for the sake of simplicity it will be referred to as a Wolter configuration in the following. The reason for this extension is that, as depicted in Figure 4.5a,

the combination of these mirrors also approximately satisfies the Abbe sine condition. Figure 4.5b shows a schematic representation of the Wolter assembly as designed and manufactured by Thales SESO. The center-to-center distance between the two mirrors is 30 mm and the grazing angle of incidence on each mirror is 15°, thus achieving the desired deflection angle of 60°.

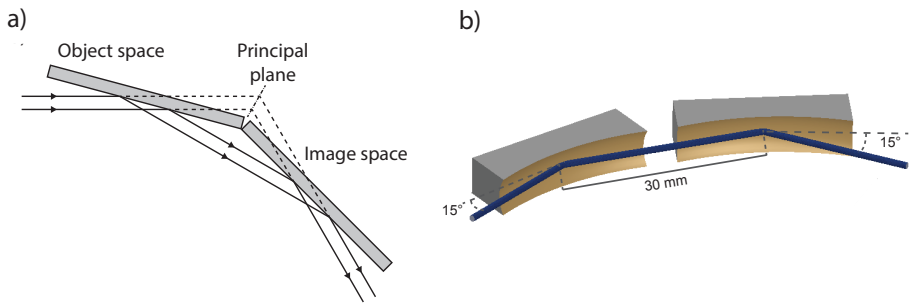

Figure 4.5: a) Visualization of approximate satisfaction of the Abbe sine condition: the rays in the object space meet the rays in the image space at the principal plane, behind the mirrors. They cross the plane almost at right angles. b) Schematic representation of Wolter optics, showing the center-to-center distance and the angles of grazing incidence.

Thanks to the nature of the toroidal surface and the presence of two mirrors it is possible to set the four radii of curvature, according to Equations 4.1 and 4.2, so as to match all the requirements for focal length and compensation of the aberrations. Table 4.1 gives the individual radii and focal lengths in the two planes, as well as the combined focal length, which results in about 164 mm (from the center of the second mirror), calculated in the paraxial approximation. This guarantees the required imaging properties.

	Tangential		Sagittal	
	R_T [m]	f_T [mm]	R_S [m]	f_S [mm]
First mirror	2.050	265.3	0.1372	265.0
Second mirror	4.213	545.2	0.2818	544.4
Combined	Focal length = 164.2 mm			

Table 4.1: Curvatures and focal lengths calculated from Equations 4.1 and 4.2 for the individual mirrors and the equivalent focal length of the assembly.

The mirrors are coated with gold because of its broadband reflectivity in the XUV range. In fact, the gold layer yields 61% reflectivity for s-polarized light, between 20 and 50 eV, and for a grazing angle of incidence. The ideal throughput of the assembly is then 37%. The optics were installed in a sturdy assembly and prealigned by the manufacturer in order to maintain the relative alignment of the two mirrors. This assembly is installed on a custom-made 5-axis motorized stage to assure the maximum degree of flexibility in the alignment. Figure 4.6 shows the degrees of freedom of the

movement of the stage (a), and a photograph of the assembly (b). The movements labeled 1 and 2 are linear translations actuated by piezo-driven stick-and-slip positioners with precision better than 1 nm. The movements labeled 3-5 are rotations applied by a vertical goniometer, a rotation stage, and a horizontal goniometer, respectively. The resolution of the goniometers is about 40 µ°, and that of the rotation stage is about 2 µ°. The movements will be referred to by the corresponding numbers in the following.

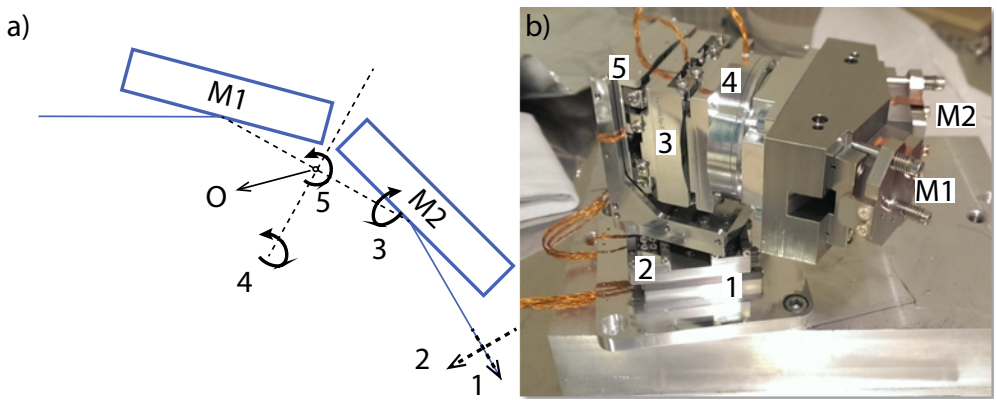

Figure 4.6: a) Representation of the movements actuated by the mechanical stage. 1 and 2: linear translations along and orthogonal to the axis coincident with the direction of propagation of the outgoing beam. 3 and 4: rotations around axes of revolution that are aligned orthogonal to and along the direction of propagation of the beam between the two mirrors. 5: rotation in the horizontal plane around the axis crossing the point O. b) Photograph of the mirror assembly and its 5-axis stage. The labels correspond to the numbers in a).

4.3.3 Alignment

The alignment degrees of freedom needed to assure both optimal focusing and precise alignment in all three directions had not been simulated prior to designing the mechanical stage, nor had the possible couplings between the effects introduced by each of the movements. Raytracing simulations were therefore performed to estimate the effect of each of the five movements independently, i.e. one movement was implemented in the raytracing model while keeping the other four stages in the nominal position (the nominal position corresponds to perfect alignment).

The simulations showed that neither of the two linear movements (1 and 2) affected the focusing conditions, at least to a first approximation. They can thus be used to position the focus in the center of the interaction region, defined by the gas jet and the electrodes of the particle detectors. Since the movements of the linear stages are aligned along and orthogonal to the direction of propagation of the beam going from the second mirror to the focus (local z-axis), they are decoupled. In other words, they can be used independently to set the focal position in the x- and z-directions (the x-z plane is the horizontal plane in the frame of reference of the laboratory).

Movement 3 does not affect the focusing conditions, and therefore does not change the size of the focus, to a first approximation and for small movements. Its main effect is to change the vertical position of the focus (y-direction). Since the intention is to maintain a constant height of the beam (in the frame of reference of the laboratory) from the input of the vacuum apparatus until the interaction region, this degree of freedom is, in principle, redundant. In practice, deviations can arise from slight misalignment of previous optics, and the vertical goniometer can be utilized to compensate for these deviations. Furthermore, movement 3 can also be useful for compensation of 45° astigmatism, as addressed in Section 4.4.

The remaining movements (4 and 5) both move the position of the focus and change the focusing conditions by introducing aberrations. These aberrations are addressed in Section 4.4 and in Paper **VIII**. Movement 4 induces a linear translation in the y-direction and a non-linear one in the x-direction, as shown in Figure 4.7a. Movement 5 does not move the focus in the y-direction, but it induces non-linear movement in the x-direction, as shown in Figure 4.7b.

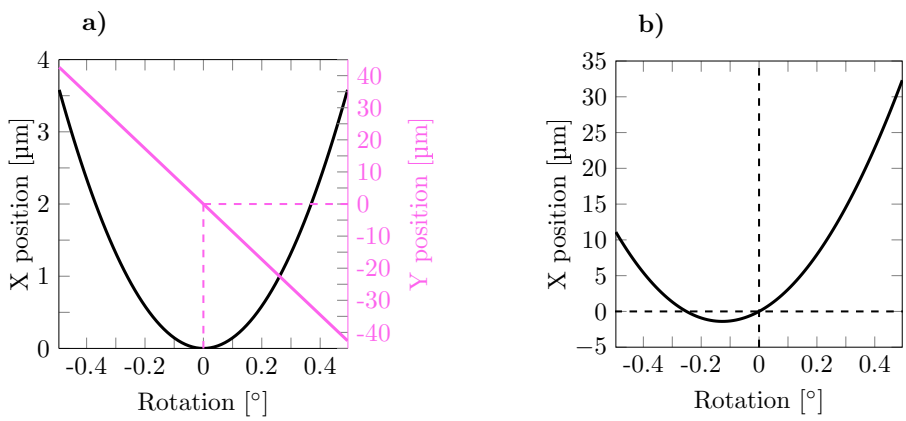

Figure 4.7: Displacement of the focus introduced by movement of the rotation stage (a) and of the horizontal goniometer (b).

4.4 High-intensity optimization: measurement of the XUV wavefronts

The sensor used to record the wavefront of an XUV beam is a so-called Hartmann sensor [112]. It consists of a mask and an XUV CCD camera, and its working principle is shown in Figure 4.8. The mask is a nickel plate with a thickness of 100 µm and an array of 34 × 34 square holes with an aperture of 110 µm and pitch of 387 µm. The holes create diffraction patterns on the chip of the camera, and their position is recorded. Comparison between the recorded position and the position of the patterns resulting from illuminating the mask with a beam having a well-known reference wavefront allows the local slopes of the wavefront to be calculated. Software is then used to reconstruct the wavefront over the whole aperture. It is possible to decompose

the wavefront into the individual contributions described in Section 2.1.1 to assess the aberrations and, for example, to optimize the alignment of the focusing components.

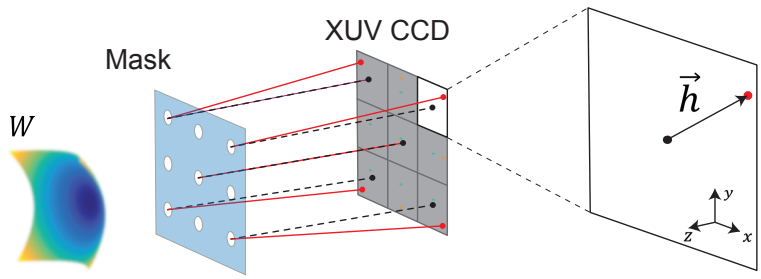

Figure 4.8: Working principle of a Hartmann sensor. The wavefront W creates an array of diffraction patterns at certain positions on the CCD chip (red dots). The distance between the spot recorded and the reference position (black dots) is given by the Hartmann vector, **h**. Its components along the x- and y- axes are proportional to the partial derivatives of the wavefront, which are used to reconstruct the wavefront. Reproduced from Paper **VIII**.

The focusing conditions were optimized in the experiment reported in Paper **VIII**. The XUV wavefront sensor was employed to record single-shot information about the wavefronts in the far field, and decomposition of these in Zernike polynomials was performed as a means of assessing the relative amounts of the three main aberrations: 0° astigmatism, 45° astigmatism, and coma. The best wavefront was found to exhibit an rms deviation of about $\lambda/36$, where λ=42 nm, and is shown in Figure 4.9a. This wavelength was chosen for the analysis as it is the weighted average of the spectra usually generated. Figure 4.9b shows a typical XUV wavefront before the focusing optics, which exhibits an rms value of $\lambda/9$. This two-fold improvement showed that it is possible to compensate for pre-existing aberrations, thus improving the quality of the focus, and the peak intensity.

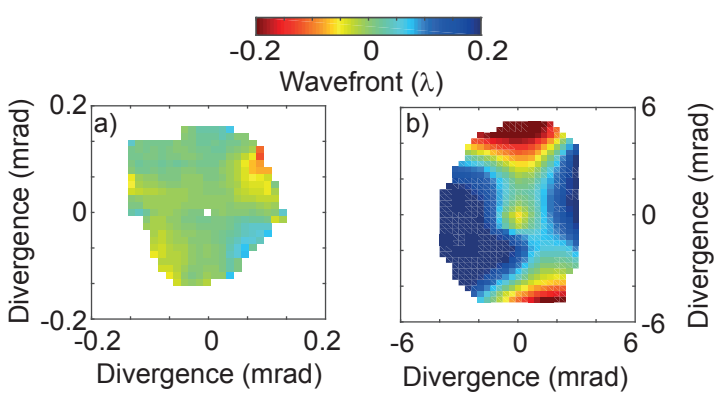

Figure 4.9: a) The best wavefront obtained after optimizing the alignment of the focusing optics. b) A typical wavefront before the focusing optics. Reproduced from Paper **VIII**.

The effect of the movements of the three rotational degrees of freedom of the me-

chanical stage holding the focusing optics was investigated in the same experiment. In fact, these movements had previously only been characterized in terms of displacement of the focus and the size of the resulting intensity distribution, without any explicit investigation of the aberrations introduced by misalignments. The investigation was conducted by varying one of the three degrees of freedom at a time, while keeping the other two unchanged. Single-shot wavefronts were recorded at each of the positions and later reconstructed and decomposed. Figure 4.10 shows the results of this analysis, in terms of the relative amounts of three different aberrations introduced by misalignment of the three rotational degrees of freedom. The experimental data points are compared qualitatively to the result of raytracing simulations, which predicted the absence of coma aberration, in agreement with the argument presented in Section 4.3.2.

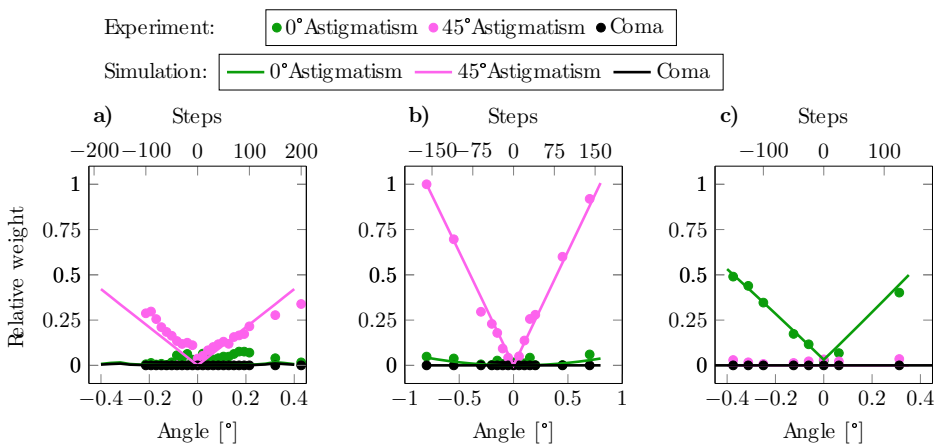

Figure 4.10: Relative amount of aberrations predicted by raytracing simulations and estimated from decomposition of the measured wavefronts. a) Vertical goniometer, b) rotation stage, and c) horizontal goniometer. The simulations refer to the lower x-axis, which is in absolute angles. The experimental data refer to the upper x-axis, which is in number of steps. All the data was analyzed following the same procedure, and simluated data and experimental data were normalized independently, but consistently between the three panels. The point to which all the remaining points are normalized to is the one with relative weight 1 in b). The reason for this choice was that at this point the overall rms of the simulated and experimental data matched. The comparison should therefore intended as qualitative, and the scope of this analysis was to show a clear correspondence in the two trends. Reproduced from Paper **VIII**.

Knowledge of all the components of a wavefront allows back-propagation of the intensity distribution to the focal plane. The best wavefront, shown in Figure 4.9b, was back-propagated and resulted in the intensity distribution shown in Figure 4.11a, having a size of 3.6 µm × 4.0 µm. Figure 4.11b shows the result of raytracing simulations, which predicted an intensity distribution in the focus giving a size of 3.0 µm × 3.2 µm, in good agreement with the measured size.

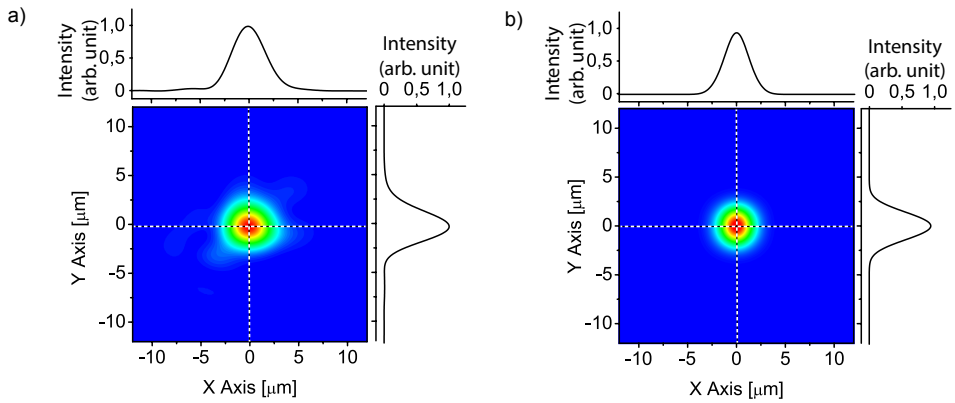

Figure 4.11: Color maps of the intensity distribution obtained from: (a) back-propagation of the wavefront in Figure 4.9b, (b) raytracing simulation. The black lines are the lineouts of the distributions through the center of the data. Reproduced from Paper **VIII**.

4.5 High-intensity application: TPDI of neon

In the experiments reported in Paper **II** the intense XUV pulses were used to induce two-photon double ionization (TPDI) in neon. Two competing pathways can contribute to the production of Ne^{2+} from the ground state, as shown in Figure 4.12. Figure 4.13 shows a typical spectrum generated in argon during the experiment. Direct single-photon ionization of neon would require photons with energies exceeding 62.5 eV, which are not present in the spectrum.

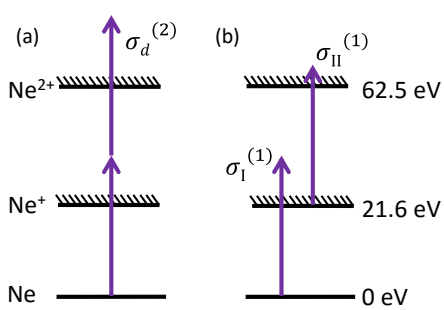

Figure 4.12: Possible pathways involved in TDPI of neon, in a direct (a) or sequential (b) process. $\sigma_d^{(2)}$ is the cross-section of two-photon direct absorption, $\sigma_I^{(1)}$ is the cross-section of single-photon ionization from the ground state to the first ionic state, and $\sigma_{II}^{(1)}$ is the cross-section of single-photon ionization from the first to the second ionic state. The probability of the process is directly proportional to the cross-section. Reproduced from Paper **II**.

The pulses generated were focused in the neon gas jet in the interaction region of the TOF spectrometer, and a peak located at a mass/charge ratio of 10 was observed, corresponding to the ion Ne^{2+}. The peak intensity in the focus was estimated to be 3×10^{12} W/cm^2, calculated from the measured energy generated and the focal

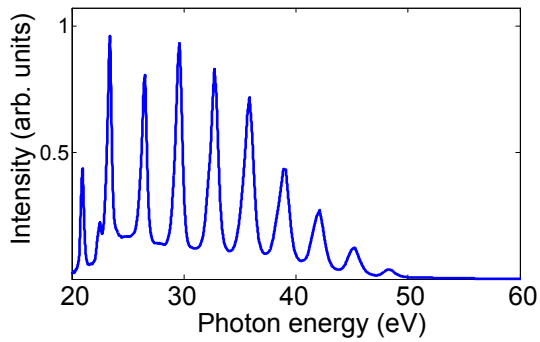

Figure 4.13: Typical spectrum generated in argon during the experiment. It contains harmonic orders 15 (23.3 eV) through 33 (51.2 eV). The peak at 20.5 eV arises from second-order diffraction on the grating of the spectrometer. Reproduced from Paper **II**.

distribution, as discussed in Section 4.2.3. The energy of the XUV pulse in the focus was calculated with the measured transmission of the aluminum filters and assuming the reflectivity of the optics. The equivalent duration of the XUV APTs was estimated to be of about 4.5 fs. The yield of Ne^{2+} was measured against the intensity of the XUV pulses to confirm that double ionization arose from a non-linear process, i.e. involving the absorption of two XUV photons. The dependence was expected to be quadratic, consistent with a second-order process. The trend was fitted and the slope was found to be 1.8, which is reasonably close to 2, thus confirming the second-order nature of the ionization process.

The TDPI process was also demonstrated to take place predominantly in a sequential manner. In fact, Ne^{2+} was not observed in the TOF spectrum when repeating the experiment with XUV pulses generated in krypton to limit the spectral bandwidth to below 41 eV, which is the photon energy needed for the second ionization step to take place, as shown in Figure 4.12.

Chapter 5

The pump-probe setup

This chapter describes the pump-probe setup designed and implemented by the author, as well as the preliminary tests carried out to assess the performance of the setup (Paper **V**). It also introduces the theoretical background needed to extend the well-known techniques for IR pulse metrology, described in Chapter 2, to the XUV spectral range. At the end of this chapter, the first results of time-resolved experiments are presented.

The pump-probe setup consists of two components: a split-and-delay unit (SDU) and its all-optical stabilization interferometer. The former is located inside a vacuum chamber, namely the interferometer chamber, which is permanently integrated in the beamline between the generation chamber and the diagnostics chamber, and the latter is next to the chamber. The layout is shown in Figure 5.1.

5.1 Split-and-delay unit

The XUV pulses, co-propagating with the IR pulses, reach the SDU and are split into two replicas upon reflection on the optics installed on the device (splitting mode). The pulses then propagate further towards the diagnostics chamber. The SDU is installed on a linear stage that can be used to translate the entire assembly parallel to the reflecting surface of the optics, thus allowing the entire beam to be reflected by only one mirror while maintaining the direction of propagation of the reflected beam (normal/alignment mode). This is desirable both for alignment purposes and for performing experiments requiring only one beam, since the wavefront splitting performed by the optics of the SDU reduces the peak intensity by a factor of at least two.

The SDU performs two functions: it splits the wavefront of the XUV pulses into two replicas, and delays one of them with respect to the other, while still sending them both to the same focusing optics. In order to guarantee the availability of high intensity in the experimental region, the optical components of the device must have high broadband reflectivity in the XUV. At the same time, they should assure a good extinc-

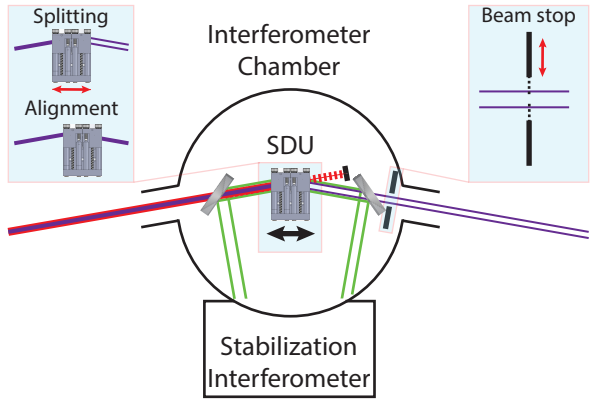

Figure 5.1: Schematic representation of the interferometer chamber: it hosts the SDU and its stabilization setup. Two small beams from a green diode laser are inserted into the beam path via a holey mirror and then picked out wiht a second holey mirror. The IR beam is partially transmitted by the optics in the SDU. The left inset shows two operation modes of the SDU: splitting wavefront mode (resulting in two replica beams) and alignment mode. It is possible to switch between two by linear translation (red arrow). The right inset shows a detail of the beam stop. It is possible to select either replica by linear translation of the beam stop. HM: holey mirrors. Their size is exaggerated for the sake of clarity.

tion ratio of the fundamental beam, and their steering must be remotely controlled in vacuum in an automated fashion. The following sections describe the implementation chosen for the various functions of the SDU and its stabilization interferometer.

5.1.1 Wavefront splitting

The optics installed in the SDU must create two identical replicas of the incoming XUV pulses. As pointed out in Section 2.2, transmissive optics are not available in the XUV spectral range, thus amplitude beamsplitters are not feasible, and the two replicas must be created through wavefront splitting. In other words, the pulses are sent to the edge of the aligned surfaces of a pair of split mirrors which separately reflect the two halves of the wavefront, thus creating two mirrored replicas of the incoming pulses, each of them having the same original amplitude.

Substrate

The substrate chosen for the split mirrors is silica (SiO_2), which allows for partial transmission of the fundamental IR field and the deposition of an anti-reflection thin film coating for the radiation at IR wavelengths with *s*-polarization (perpendicular to the incidence plane). The configuration in grazing incidence confers high reflectivity at XUV wavelengths, as discussed in Section 2.2.2. The angle of grazing incidence under which the mirrors are operated was chosen to be 10°. The coating was therefore designed for this specific angle, and consists of alternated layers of SiO_2 and TiO_2, the top layer being SiO_2. In order to achieve destructive interference of the IR field,

the layers are on the order of 100 nm thick. This guarantees that the layer under the top layer is "invisible" to the XUV radiation (because of high absorption within the top layer), thus assuring good XUV reflectivity.

The height was chosen to be 14 mm in order to ensure that the plates were completely illuminated by the IR pulses in the geometry used for HHG experiments. The length of each plate (40 mm, giving 80 mm in total) is determined by the 10° grazing incidence configuration, to ensure that the entire surfaces are illuminated with a circular beam. The thickness of 7 mm was chosen to achieve good mechanical stability. All the surfaces are polished to optical quality, while both the front and the back surfaces are coated with an 800 nm anti-reflection coating for the fundamental IR wavelength, as described above.

Geometry

Figure 5.2 shows a schematic representation of the working principle of the optical components of the split mirror, using geometric optics.

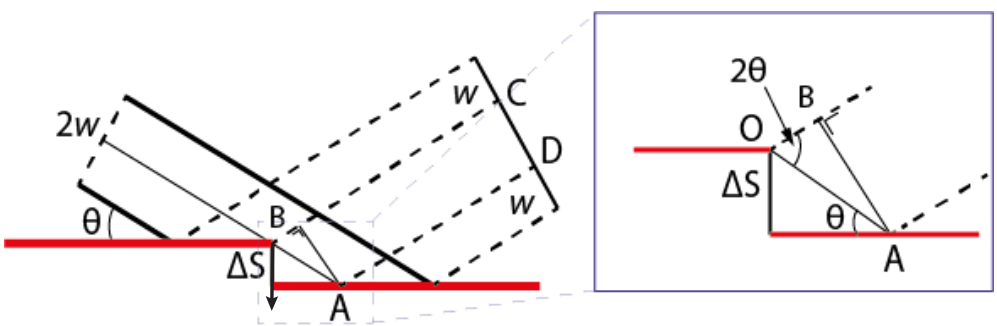

Figure 5.2: Geometrical optics of the split mirror.

The thick solid lines represent the marginal rays of a beam with width $2w$ impinging at an angle of grazing incidence of θ=10°, while the thinner solid line indicates the central ray of the beam. The dashed lines represent the marginal rays of the two beams split after reflection, each of width w. When one of the two mirrors is displaced paralely by a distance ΔS, two effects are obtained: the beam reflected by the second surface is delayed in time, and moved sideways in the frame of reference of the reflected beams. To evaluate the delay introduced by this displacement, it is useful to consider the inset in Figure 5.2 and to evaluate the difference in the paths taken by the central ray after being reflected by the two mirrors at points O and A, which is:

$$\overline{OA} = \frac{\Delta S}{\sin\theta}, \tag{5.1}$$

$$\overline{OB} = \overline{OA}\cos 2\theta = \frac{\Delta S}{\sin\theta} - 2\Delta S\sin\theta, \tag{5.2}$$

$$\Delta\tau = \frac{\overline{OA} - \overline{OB}}{c} = \frac{2\Delta S\sin\theta}{c} = 1.1585\,\frac{\text{fs}}{\mu\text{m}}\,\Delta S[\mu\text{m}], \tag{5.3}$$

where c is the speed of light in vacuum. If ΔS is finely tunable with (sub-) micrometer precision, this gives (sub-) femtosecond resolution of the delay. The lateral displacement, corresponding to the distance $\overline{CD}$ in the figure, can be calculated as:

$$\Delta x = \overline{CD} = \overline{BA} = 2\Delta S \cos\theta = 1.7 \frac{\mu\text{m}}{\text{fs}} \Delta\tau[\text{fs}]. \tag{5.4}$$

Two main aspects were taken into account when deciding for this configuration for the split mirrors (with the edge of the two mirrors perpendicular to the direction of propagation, i.e. vertical, or parallel to the direction of propagation, i.e. horizontal): focal overlap and reflection losses. The former is addressed in Section 5.1.2, while the latter can be understood from a simple trigonometric argument, considering a 1 mm FWHM beam impinging on the split mirrors when the plates are separated by a gap of about 100 µm, in two different cases. When the edge is horizontal, the full extent of the gap causes losses that amount to about 10% of the total intensity, regardless of the displacement between the two plates, while when the edge is vertical the maximum loss at zero delay is reduced by the angle of incidence to about 2% of the total intensity. Referring to Equation 5.3 and Figure 5.2, it is straightforward to estimate that the losses due to the rays "transmitted" through the gap become zero at a delay of about 20 fs. Furthermore, the direction of the displacement ΔS was chosen to avoid "shadowing" effects that would arise if ΔS was in the opposite direction. Although it increases the precision in setting the delay, the grazing incidence geometry effectively decreases the range of delays achievable by a factor corresponding to the sine of the angle θ ($\sin 10° = 0.17$). This reduces the mechanical instabilities: in fact, for a small fluctuation in the displacement, of δS, the corresponding instability in the delay, $\delta\tau$, is also reduced by the same geometrical factor.

5.1.2 Delay line and stabilization

Mechanics

The geometry and the required optical properties of the SDU induced the choice of the piezoelectric actuators, which had to be done considering both the desired maximum achievable delay and the physical size of the device. Current state-of-the-art cased piezoelectric actuators offer a travel range that is about a thousand times smaller than the size of the piezoelectric crystal, with resolution down to the (sub-) nanometer regime. In order to obtain an effective delay of about 50 fs, according to Equation 5.3, the actuators must support a total movement of about 45 µm.

The design was conceived to meet all the requirements on functionality and rigidity, while maintaining high flexibility for future upgrades. For this reason, the mount is symmetrical about the plane that contains the gap between the two split mirrors, to allow it to be used in different geometrical configurations. The mount, illustrated in Figure 5.3, consists of a base plate mountable on standard optical posts, and two movable parts, each of them holding one mirror. The assembly is equipped with three piezoelectric actuators (P-840.3 Physical Instruments) with a total travel range of 45 µm, and three dummy actuators, which are replicas of the actuator casings without the piezoelectric actuators. In this way either, of the two movable mirror holders can be actuated through a computer, depending on how the SDU is assembled. Furthermore,

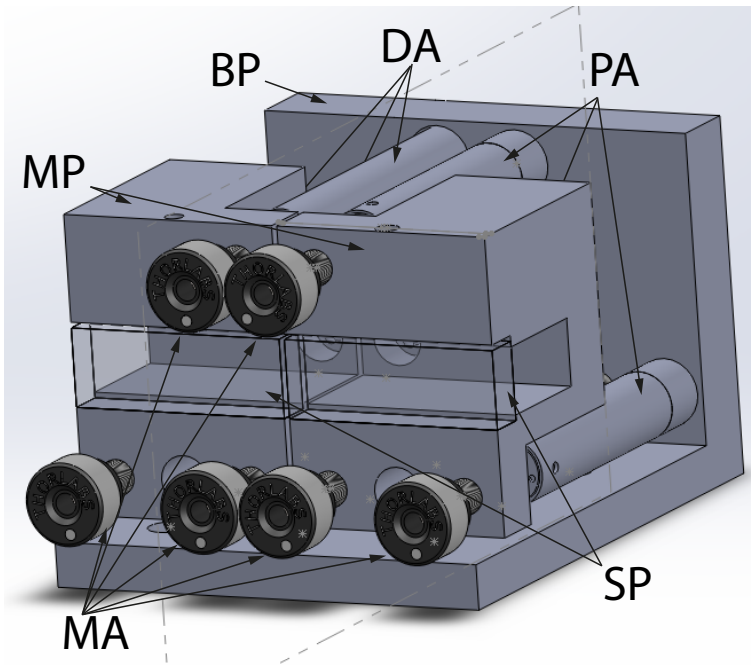

Figure 5.3: 3D model of the SDU. BP: base plate. MP: movable parts. SP: split plates. PA: piezolectric actuators. DA: dummy actuators. MA: manual actuators.

there is the possibility of upgrading the design by installing six piezoelectric actuators, to obtain full control over the steering of both the incident beams. All the real and dummy actuators are screwed directly on the base plate from the back side.

The two movable parts are each held against the ball tips of the actuators by two extension springs (Lesjöfors Gas & Stock Springs, #9767), and contact is made in such a way that the ball tips are resting in the sockets of the ball tips of manual actuators for standard optics holders (Thorlabs DAS110). These manual actuators are very finely threaded differential screws, which allow prealignment of the entire assembly to a very high precision (25 µm/revolution). Figure 5.4 shows the springs and the contact between the manual and piezoelectric actuators through the ball tip of the latter. The ball tip decouples the vertical force from the horizontal force, so that the weight of the movable parts does not introduce a torque on the encased piezoelectric actuators, which would damage them (torque limit: 0.35 Nm). The actuators are arranged in an "L" shape, so that one of them can control the pivot point, which can be pre-set to be immediately below the reflecting surface of the mirror, while the other two control horizontal and vertical movement. This configuration minimizes the coupling between the different movements. The travel range of the piezoelectric actuators and the relative distances between them are such that the maximum deflection angles introduced are 1.7 mrad and 1.2 mrad in the horizontal and vertical directions, respectively. Figure 5.5 shows a photograph of the assembled device, in its current state.

A homemade beam stop is installed after the SDU to block either of the two replicas to allow the two foci to be aligned in the focal region, which is crucial for pump-probe

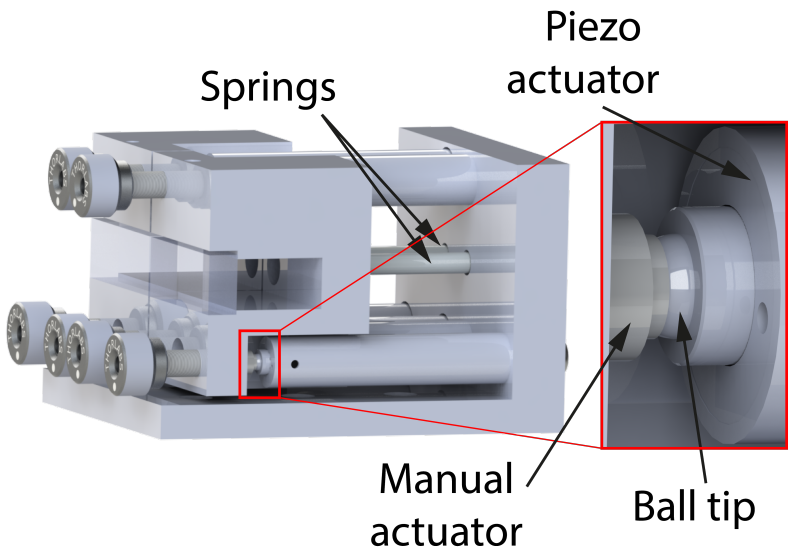

Figure 5.4: Rendering of the SDU model. The inset shows the contact between the micrometric screws and the actuators.

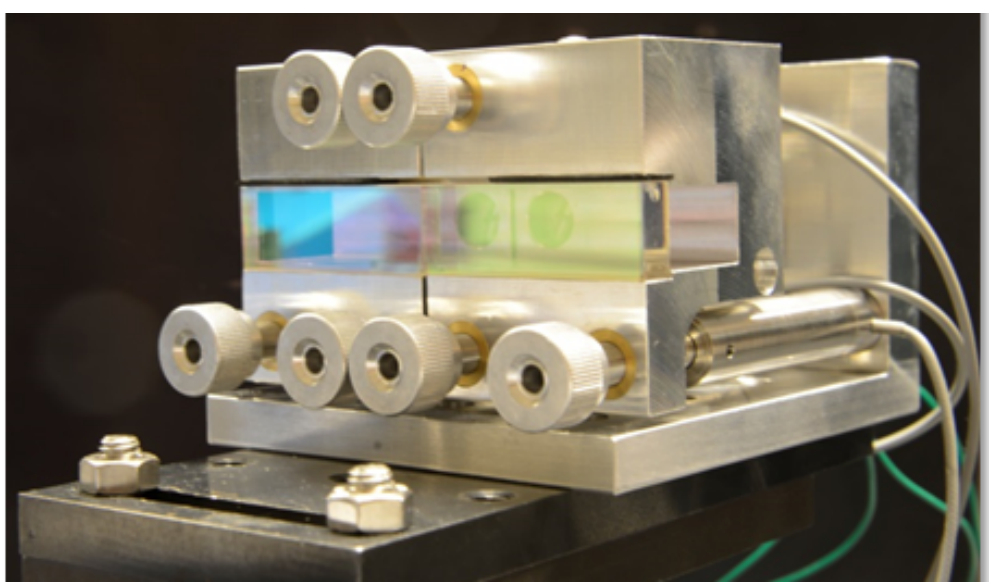

Figure 5.5: Photograph of the SDU.

experiments. A description of the alignment procedure is provided in Section 5.1.4.

Feedback loops

When performing non-linear experiments involving the two split replicas, not only must the temporal delay be finely tuned, but the spatial overlap of the two beams must also be preserved. Both of these can be achieved with active stabilization feedback loops. In the configuration for which the beamline was designed, after generation in the gas cell, the harmonic beam propagates over 6 m down to the application chamber. Along this path the beam diverges before impinging on the SDU and being split, and continues to diverge until it reaches the application chamber, where the focusing optics are installed.

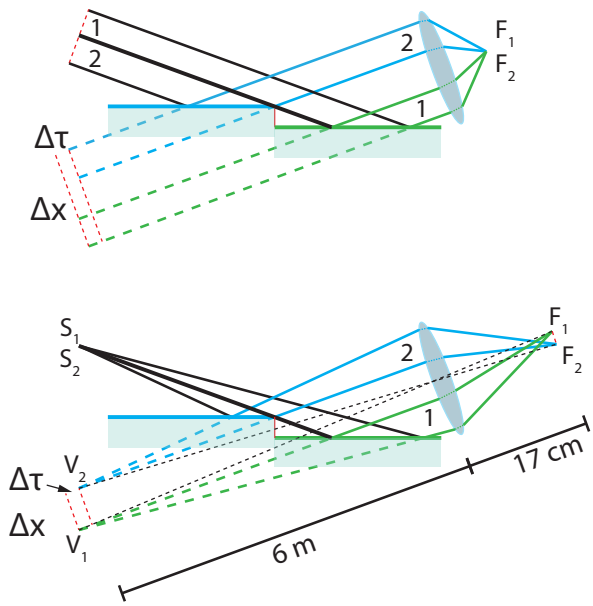

Figure 5.6: Effect of parallel displacement of one of the mirrors (green) on the focal points F_1 and F_2 in two cases: collimated beams from an infinitely distant source (above) and diverging beams from a point source (below).

The purpose of Figure 5.6 is to illustrate why a feedback loop is needed. If a collimated beam (upper part of the figure) is split into two parts (1 and 2), one of which is delayed and translated sideways upon reflection (1), the two resulting beams are still focused at the same position F_1=F_2. If the rays are traced back in the virtual space behind the split mirrors, the two halves of the wavefront will be found at two different planes (red dotted lines), separated in time by $\Delta\tau$, and laterally by a distance Δx, as discussed in Section 5.1.1. This is the effect of the two different paths taken by the central ray of the original beam. If the beam is divergent (lower part of Figure 5.6), i.e. if it originates from a point source (S_1=S_2), the two split halves will be focused at different positions $F_1 \neq F_2$. In order to explain why, let us consider the rays traced back to the virtual space behind the mirrors. The effect of the delay introduced by the movable mirror is twofold: in the two virtual point sources (V_1 and V_2) are separated in time by $\Delta\tau$ as in the previous case, and the two point sources move

apart laterally by a distance corresponding to Δx. The two different point sources will thus be imaged at different positions, giving rise to a distance $\overline{F_1F_2} \neq 0$. By tilting the movable mirror (green) it is possible to move the focal spot F_1 to make it overlap the other focal spot, F_2. This causes the two virtual point sources to coincide ($\overline{V_1V_2} = 0$), giving rise to a focus that is a combination of the two overlapping foci. From Equation 5.4 it can be estimated that the separation of the two virtual sources is about $\overline{V_1V_2}$=89 µm when the maximum delay is introduced. This corresponds to about 3 µm in the focal plane for the current XUV focusing geometry. This effect can be neglected in many cases, but in our case, as the spotsize is expected to be on the order of a few micrometers, a small deviation may lead to a loss of overlap, and even a drift of a small fraction of the FWHM spot size will lead to a significant decrease in peak intensity. Furthermore, if the two foci are not overlapped, the photons from the two replica pulses will not interact with the same target atom or molecule, thus not giving rise to a non-linear signal. Furthermore, since the piezoelectric actuators installed on the mount are open-loop, their actual elongation, once they are fed a certain voltage, is irreproducible and unpredictable. This results in a loss of pointing stability when the same voltage is applied to all three actuators to apply a certain delay between the two replicas. An active feedback loop is needed for both of these reasons, but merely installing closed-loop piezoelectric actuators would not have been sufficient to obtain the overlap in the focus, and the decision was made to implement the feedback in an all-optical fashion.

Figure 5.7 shows a photograph of the stabilization interferometer as it is currently implemented. The beam from a green laser diode is first made divergent by detuning a telescope to match the source position to that of the beam to be stabilized, i.e., to the XUV beam, or alternatively to the IR beam used in the case of the tests presented in Section 5.1.3. A mask is then inserted in the beam in order to avoid the strong horizontal diffraction patterns that would arise from splitting the wavefront of the green beam. The stabilization beam is inserted in the beam path of the beamline via a holey mirror placed in front of the SDU, and it co-propagates with the XUV and IR beams. After impinging on the split mirrors, the stabilization beam consists of two delayed replicas which are then picked out after the SDU by another holey mirror, and split into two parts by amplitude splitting. One part of these two replicas is focused onto the chip of a camera, and on the other side of the beamsplitter the two replicas are crossed onto the chip of another camera in order to create an interference pattern.

When two beams are crossed they produce an interference pattern, and the intensity distribution has the mathematical form: $I(x) \propto \cos^2(\Lambda x - \omega\Delta\tau)$. The oscillation period Λ depends only on the wavelength of the radiation and the crossing angle between the two beams, where ω is the angular frequency of the crossed beams and $\Delta\tau$ their relative delay. By performing Fourier analysis on the recorded image it is possible to retrieve the phase of this oscillation, and it is then possible to determine the relative delay between the two replicas by following the evolution of the phase of the signal. The difference between the required delay and the actual delay is the error function for the proportional-integral-derivative (PID) loop controlling all the three actuators of the mechanical mount of the SDU.

The focal profile of one of the two beams is recorded on the other arm of the interferometer. By setting the fixed focus as a reference, the other focus can be tracked and its deviation from the reference position in the two directions is fed to the PID loops as two error functions to control the horizontal and vertical actuators

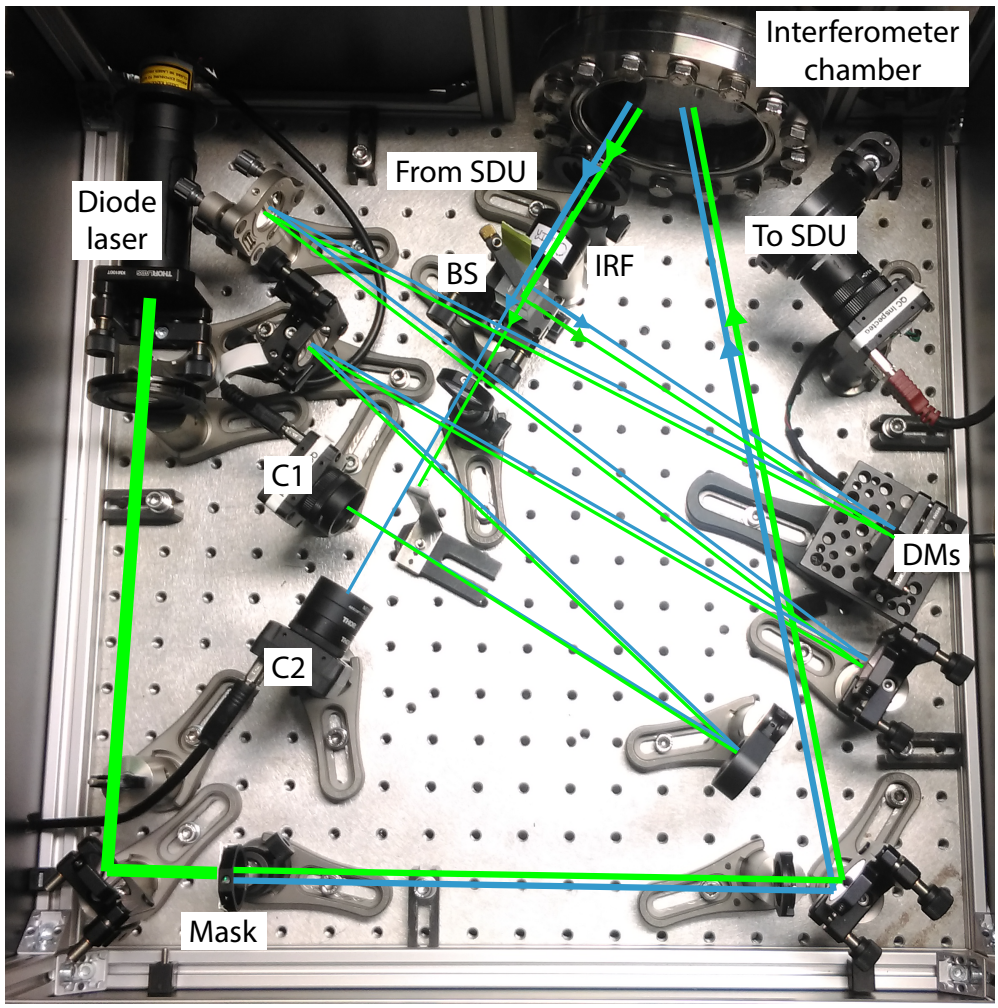

Figure 5.7: Photograph of the stabilization interferometer. The divergent beam from a diode laser is first sent onto a mask to create two smaller beams from the same wavefront, which are then sent into the interferometer chamber and picked out. The blue beam is the one that is delayed by the SDU in the interferometer chamber. Any residual radiation at IR wavelengths is filtered out with a notch filter (IRF) before the beams are split by a beamsplitter (BS). The reflected beams are crossed onto the chip of a camera (C1) by steering them individually with a pair of D-shaped mirrors (DMs). The transmitted beams are focused onto the chip of a camera recording the position of the focus (C2).

of the mechanical mount of the SDU.

5.1.3 Test of the performance

Preliminary tests were performed to assess the performance of the stabilization feedback loop in keeping the foci overlapped, and the results are reported in Paper **V**. The

deviation of the focal position from the nominal position was found to be less than 2 µm rms. Despite the fact that the PID was able to lock the position of the two foci in the focal plane of a lens, this test was performed offline, with IR pulses, and with a slightly different focusing geometry than that adopted in the HHG beamline. The same test was recently performed, after the SDU and its stabilization interferometer had been integrated in the beamline. The position of the static focus was recorded by means of the XUV microscope described in Section 4.2 and set as a reference for the moving focus. The three actuators of the SDU were moved with the aid of the delay PID control, and the position of the moving focus was recorded in two cases: when the stabilization PIDs (for the focal overlap) were off and on. Figure 5.8 presents the results of these measurements and it can be seen that the PID is indeed able to compensate for the horizontal displacement of the focal spot. The movement in the vertical direction is negligible and is therefore not shown in the plot. The black curve indicates an rms stability of about 0.7 µm, which should be compared to the size of the focus, which was about 6 µm FWHM. This is marginally worse than the predicted 0.3 µm reported in Paper **V**. The slight deviation is attributed to overall pointing instabilities in the beamline. Each data point in Figure 5.8 is the result of the accumulation of ten shots, as the camera used in the microscope did not allow for the acquisition of single-shot images. The instabilities were measured and found to be of about 0.5 µm in the focal plane, which led to an apparent larger focal distribution, and an uncertainty in identifying the center of the focal distribution. Furthermore, it can be seen that the maximum amplitude of the displacement is well above the expected 3 µm. A possible explanation is sub-optimal behavior of (at least) one of the piezoelectric actuators when operated with only one active PID over the entire range, and is being investigated at the time of writing. During every test or experiment, the feedback software logs the value of the delay error function, and its rms value can be extracted over a desired period of time. This error was estimated to less than 30 as (Paper **V**), but when integrating the SDU setup in the beamline a number of measures were made in order to reduce this error. All the optics in the interferometer were installed on short optical posts and the breadboard was encased in a box to limit the flow of air in the path of the beam. The latest tests showed a stability as good as 5 as rms.

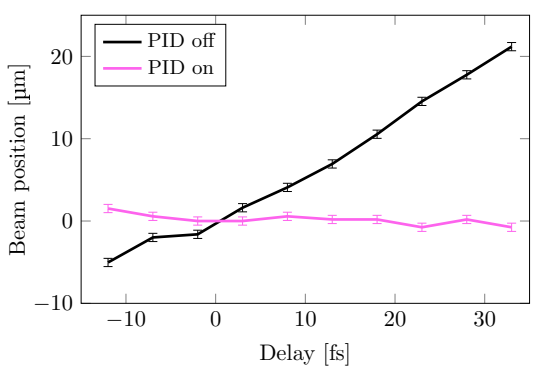

Figure 5.8: Position of the center of the beam with the PID loop on and off, recorded with the XUV microscope.

5.1.4 Alignment

Setting up a pump-probe experiment requires careful alignment. Not only must the two foci overlap in the focal region in the gas jet (their mutual alignment is then maintained by the feedback loops), but the zero delay must also be within the range of the piezoelectric actuators. Two separate alignment procedures must thus be implemented. While once the zero delay has been found it will always be in range as long as the manual actuators are not moved, setting the focal overlap is more crucial and it has to be determined before every experiment, and possibly during the course of the experiment.

Temporal overlap

In order to find the temporal overlap between two IR replica pulses, they must be overlapped in space at a certain plane where they interfere and give rise to a transverse distribution of fringes. The spacing of the fringes scales as the inverse of the crossing angle, therefore, the larger the crossing angle, the more fringes are created on the camera chip, and the finer the spacing. The overlap on the camera chip is achieved by tuning the manual actuators. The delay is then scanned by applying a voltage to the piezoelectric actuators, and the diffraction pattern is recorded by automated software which evaluates the visibility of the fringes at each delay. The temporal overlap between the two pulses corresponds to the data point exhibiting the highest visibility. This point can then be moved within the piezoelectric actuators by offsetting the three manual actuators. As open-loop piezoelectric actuators suffer from severe hysteresis, setting the zero delay too close to the end of their range may lead to this point falling out of the reach of the actuators. The visibility is thus evaluated during both the upward and downward delay ramp scans, and two maxima are found, typically about 10 fs apart. As a rule of thumb, the actuators are offset in such a way that the zero delay is at about 10% of the range. In fact, if the zero delay point is closer to the middle of the range, this would limit the range of delays that could be achieved in the experiments. Another effect that should be taken into account is that, due to the imperfect decoupling between the degrees of freedom of the SDU mount, when one mirror is moved back so as to be parallel to the other one, the effective delay may be affected. It is therefore useful to repeat the procedure at increasingly distant planes, i.e. for smaller crossing angles. Even finer tuning can be performed by observing a non-linear signal, e.g., ATI of an atomic system.

Focal overlap

Once the focusing optics are well aligned with respect to the incoming beam, the two split mirrors of the SDU must be angularly tuned to achieve focal overlap between the two replica pulses. Since the beamline, at the moment, lacks an on-line diagnostic tool to directly assess the focal distribution, indirect methods have to be used in this alignment procedure. The focus originating from the pulse that is not steered by the SDU is used as a reference to which the other focus is then aligned. Two different procedures are used for the alignment in the vertical and horizontal planes (in the laboratory frame of reference).

The movement of the beam in the focal plane was calibrated with the microscope described in Section 4.2 in terms of how many micrometers it moves per volt applied to the piezoelectric actuators. This was found to be consistent with raytracing simulations. The precision of the alignment procedures was then assessed in terms of the minimum voltage required to resolve a movement in the focus, and this resolution was compared to the focal spotsize in order to determine whether the procedure was sufficiently precise.

The spatial mode of the VMI spectrometer, described in Section 4.2, can be used for alignment in the vertical plane of the laboratory frame of reference. The images give an indication of the vertical position of the focus, and tests performed during the development of this procedure have shown that the precision achievable is about 3.5 µm, i.e., comparable to the focal spot size. In the horizontal plane, TOF spectra were used as a diagnostic tool. In this case the voltages were detuned from the Wiley-McLaren conditions (see Section 4.2) to obtain an estimate of the lateral position from which the fragments reaching the detector were originated. The lateral resolution achieved was estimated to be on the order of 5 µm, comparable to the focal spot size.

Although these procedures are tedious and time consuming, they provide a rough estimate of the focal overlap, which can then be optimized by maximizing the signal of the desired observable. As part of an upgrade of the diagnostic tools in the near future, an XUV wavefront sensor will soon be permanently installed after the focal region. Tests are being carried out to determine whether this tool can offer a reliable procedure for overlapping the foci in both planes. This is briefly addressed in Chapter 6.

5.2 Volume autocorrelation of XUV pulses

When the duration of XUV pulses is to be measured, be it in the femtosecond or in the attosecond regime, two main difficulties must be overcome, namely the broader spectral width of the pulse and its much lower intensity, compared to those of IR pulses. The aim is to use two XUV replica pulses to initiate a non-linear process, and to measure the yield of the products (ions and/or electrons) resulting from the process, as a function of the relative delay between two replica pulses. The process must be of at least the second order because a linear process would give rise to a signal corresponding to the field autocorrelation of the pulse, thus not providing any other information than the transform-limited duration, as explained in Section 2.3.2. The photoionization of noble gases is a suitable process since the relatively high ionization potentials (on the order of a few tens of eV) make the absorption of two XUV photons necessary for it to be overcome. As an example, helium has been previously utilized as a target to measure the duration of XUV pulses [34]. Its first ionization potential, at 24.6 eV, allows for the detection of pulses containing photon energies up to immediately below the potential. If the spectrum of the XUV pulse contained energies exceeding 24.6 eV, these photons would contribute to the ionization process in a single-photon manner, thus constituting an unwanted background. If pulses with a spectrum that extends to higher photon energies are to be measured, it is important to choose a suitable target gas and an ionization potential above the highest photon energy in the spectrum. For example, and as a reminder of the experiment described in Section 4.5, a typical spectrum generated in argon contains energies ranging from 23.3 eV to

51.2 eV, and neon has a second ionization potential at 62.5 eV, as shown in Figure 4.12. It is therefore a suitable target gas for measuring the duration of the XUV pulses generated. If the TPDI process was taking place predominantly in a direct manner, or, in other words if the system did not relax back to its first ionic state before absorbing a second photon, it would be possible to measure the autocorrelation of the pulse comprising the whole spectrum. Since the process takes place in a sequential manner, the entire spectrum contributes to the first ionization step, while only the four highest harmonic orders contribute to the second ionization step. In this case, the delay-dependent signal that would be observed corresponds to a cross-correlation between the original pulse and the pulse resulting from the superposition of the four highest harmonic orders.

Measurement of the pulse duration in the XUV spectral region is more challenging than that in the IR or visible spectral ranges. There are two reasons for this: the nature of the wavefront splitting, and the detection schemes usually employed. Splitting a beam into two replicas introduces a sharp truncation of the wavefront, giving rise to a steep gradient in the spatial phase in the transverse direction. The evolution of the spatial phase upon propagation has been evaluated both analytically [61] and numerically [34]. This can be done numerically in the framework of Fourier optics. For the sake of simplicity, only the transverse direction is considered in the following discussion, and it should be interpreted as the direction along which the wavefront is split. The intensity and spatial phase distributions in the other direction, i.e., perpendicular to the direction of propagation and the transverse direction, are not affected by the wavefront splitting, to a first approximation.

Figure 5.9 shows the result of the numerical calculation. The two beams exhibit the same focal intensity distribution (black curve) and distributions of the spatial phase that are specular to each other (purple and green curves). They are almost linear within the region where the intensity is above $1/e^2$ of its maximum value. The amplitude of the phase difference between the maximum and the minimum of the individual profiles is $\pm\pi$.

When the two beams overlap in the focal plane, they interfere and give rise to the intensity distribution shown in Figure 5.10a. The difference between the two phase distributions shown in Figure 5.9 is close to π on the shoulders of the intensity peak, as illustrated qualitatively in Figure 5.10d. This leads to destructive interference in these regions, and the focal distribution originating from the interference between the two beams is narrower than that of the individual beams.

When a nominal delay is introduced between the two replicas (nominal delay should be interpreted as that imposed by the delay line in the SDU, and as the phase difference at the center of the intensity distribution), it constitutes an additional temporal phase that is constant in spatial coordinates. This essentially translates one of the two wavefronts in Figure 5.10d along the y-axis, as shown in Figure 5.10e for a delay of $\pi/2$. The position at which the phase difference between the two beams is π (indicated in the figure by the dashed black line) moves along the transverse direction. This causes destructive interference to take place at a different position from the case with zero delay, as shown in Figure 5.10b.

If the nominal delay corresponds to π, destructive interference takes place at the center of the intensity distribution, as shown in Figure 5.10f, thus resulting in the intensity distribution shown in Figure 5.10c.

The bottom row of figures in Figure 5.10 also shows that when two tilted wavefronts

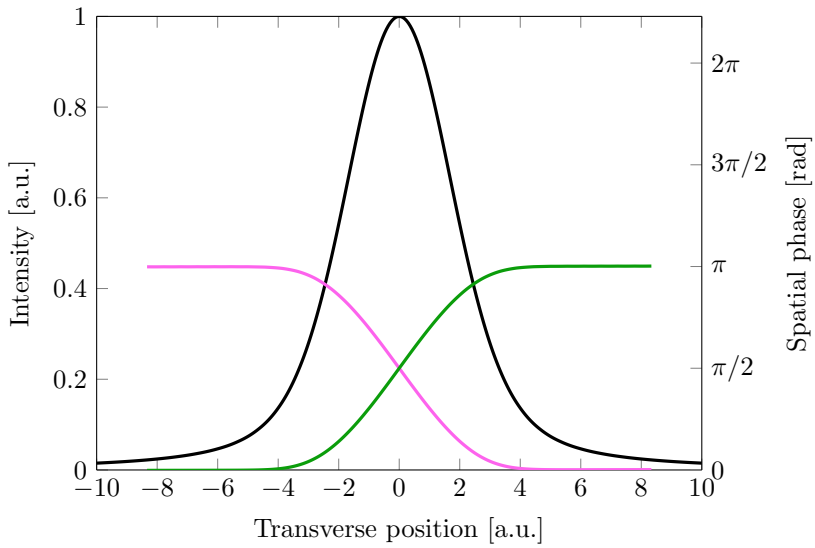

Figure 5.9: Intensity distribution (black curve) of both replica beams in the focal plane, and phase profiles of the two replicas (green and purple curves). The curves were obtained by propagating two half wavefronts of a monochromatic beam to the focal plane of the focusing optics, using Fourier optics.

propagate along the z-direction and interfere in a given plane where they are observed, the resulting difference in phase varies along the transverse direction. In practice, the difference in phase, $\Delta\Phi$, is mapped onto the transverse direction, x. This effect, combined with a detection scheme with sufficient transverse resolution, such as an ion-microscope [113], would allow for single-shot autocorrelation traces to be recorded by detecting the photoionization products [114, 115]. In fact, at each shot, photons from one beam interact in the gas with photons from the second beam, and the relative delay between the photons depends on the transverse position at which they interact. The yield of the ions at different positions therefore carries information on different delays.

In other cases, such as when a VMI spectrometer is employed, it is necessary to detect the particles at each value of the nominal delay. The yield of the detected ions then depends on the nominal delay, but it also contains information on all the other delays mapped onto the transverse direction at that value of the nominal delay. Furthermore, detectors such as the VMI spectrometer, perform an additional spatial integration. Not only is the signal detected from the entire focal plane, but also from every plane along the direction of propagation of the beam and within the interaction region.

There are two main significant differences between a standard autocorrelation, such as those described in Section 2.3, and a volume autocorrelation. The first is due to the volume integration performed by the particle detector. If the signal was recorded from a single point at the center of the focal distribution, it would correspond directly to a collinear interferometric autocorrelation. The volume integration averages the signal corresponding to the nominal delay, as well as the entire range of delays

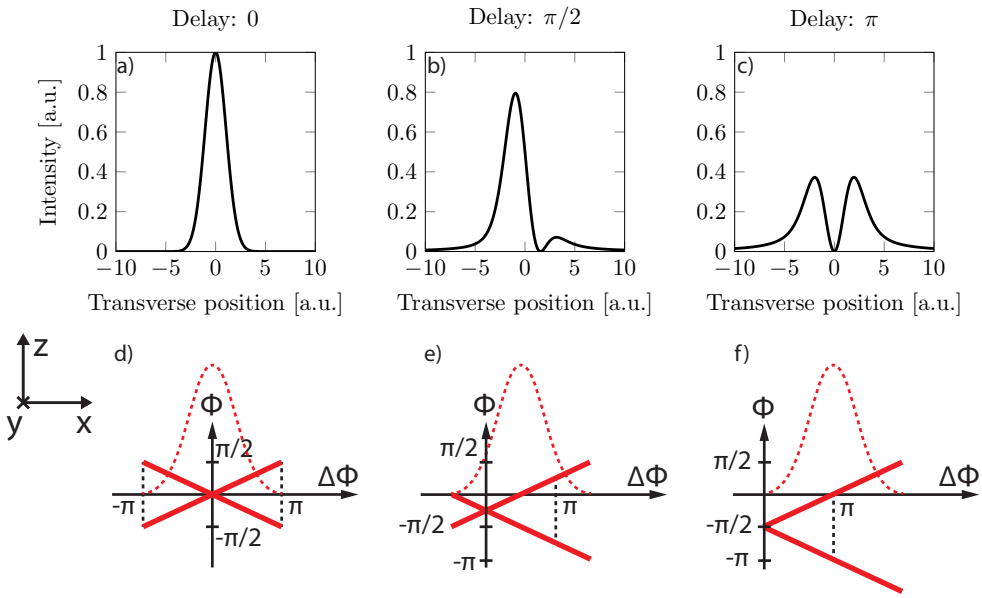

Figure 5.10: a-c) Intensity distributions resulting from the interference of two beams with intensity and phase distributions as in Figure 5.9, and with different relative delays. It is important to note that the integrated intensity, and therefore the energy, in the distribution is independent of the delay. This is an essential difference compared to, e.g., the output of a Michelson interferometer. d-f) The solid red lines represent two flat wavefronts in the focal plane, propagating at a small angle to the optical axis, which is aligned with the z-axis. They are an approximation of the actual wavefronts. The dashed red curves represent the intensity distribution of the individual replica beams, Φ is the phase, and $\Delta\Phi$ is the difference in phase between the two wavefronts. $\Delta\Phi=\pi$ at the positions indicated by the dashed black lines. d) The nominal delay between the two beams is zero, and $\Delta\Phi=0$ at the center of the intensity distribution. Destructive interference takes place at the shoulders of the intensity distribution. e) The nominal delay between the two beams is $\pi/2$, which causes one of the wavefronts to shift towards negative values of z and ϕ. As a consequence, the position at which $\Delta\phi=0$ is shifted towards positive values of x, and so is the position at which destructive interference takes place. f) The nominal delay between the two beams is π, which causes destructive interference at the center of the distribution. Matching of the horizontal axes between the top and bottom rows is only qualitative.

that are mapped onto the transverse direction, as argued above. This is analogous to performing a running weighted average on the trace resulting from a collinear interferometric autocorrelation. The result is a lower peak-to-background ratio, which was shown to be close to 2.75:1, instead of the traditional 8:1 (see Section 2.3.3).

The second difference is due to the resolution of the delay line of the typical pump-probe scheme employed. In fact, interferometric autocorrelation traces oscillate at the frequency defined by the carrier frequency of the pulse measured, and its Fourier transform spans components up to twice the highest frequency contained in the spectrum of the pulse to be measured. Typical spectra generated by HHG in argon extend to harmonic orders up to the 35^{th}, which have an oscillation period of about 76 as. To

sample oscillations with a period of 38 as requires a resolution of, or better than, 19 as, according to the Nyquist theorem. Such a resolution is approaching the limits of current technology in all but a few cases [25, 34, 116]. The stability of the SDU was estimated to be 5 as rms (Section 5.1.3), which should, in principle, allow pulses comprising harmonic orders up to the 133$^{\text{rd}}$ to be measured. If the resolution of the delay is not sufficient to resolve the fast oscillations of an interferometric autocorrelation, the resulting trace is the corresponding cycle-averaged signal [34]. This corresponds to the intensity autocorrelation component $C_0(\tau)$ shown in Figure 2.5. In this case, the volume integration reduces the peak-to-background ratio to 2:1, compared to the ratio of 3:1 observed in the figure [34].

Nevertheless, it is possible to extract information about the pulse duration from a volume autocorrelation, both in the case of IAPs and APTs. In fact, the former is a pulse with a similar temporal structure to laser pulses, and the latter consists of a train of pulses that resemble laser pulses. In this scenario, it is possible to extract both the duration of the envelope that encompasses the entire train of attosecond pulses and the duration of the individual pulses.

5.3 First results of time-resolved experiments

Section 5.1 presented the SDU, the device needed to perform time-resolved experiments, while Section 5.2 provided the theoretical background of XUV autocorrelations performed with the SDU. This section presents the first results that were obtained utilizing the SDU. Two types of autocorrelations were performed on IR pulses, which are reported in Paper **V**: a first-order and a second-order autocorrelation. IR pulses were also employed to induce ATI in argon, and the delay-dependent signal was recorded. Finally, the XUV microscope described in Section 4.2 was utilized to observe the intensity distribution arising from the interference of two replica XUV pulses as a function of the delay between the replicas.

5.3.1 Autocorrelation of IR pulses

After the SDU and its stabilization interferometer had been tested, they were employed to record autocorrelation traces of IR pulses. The setup illustrated in Figure 5.11 was inserted into the beam path of a broadband few-cycle IR laser pulse, whose spectrum is shown in Figure 5.12, and with a Fourier transform-limited duration of about 6 fs.

In the first experiment, the mirrors in the SDU were tilted to create an interference pattern on the sensitive area of a photodiode. If the energy of the entire pattern is recorded, the signal would either not exhibit clear time-dependent oscillations, or their contrast would be reduced (as discussed in Section 2.3.2). In order to perform a field autocorrelation it is necessary to measure the energy at only one point, or at least a small portion of, the interference pattern. A pinhole was placed in front of the photodiode as a means of increasing the contrast by selecting only the central part of the wavefront.

Figure 5.13 shows the measured field autocorrelation trace and the simulated trace, as the Fourier transform of the spectrum shown in Figure 5.12. Since the simulated field autocorrelation is calculated from the spectrum recorded before the setup, the

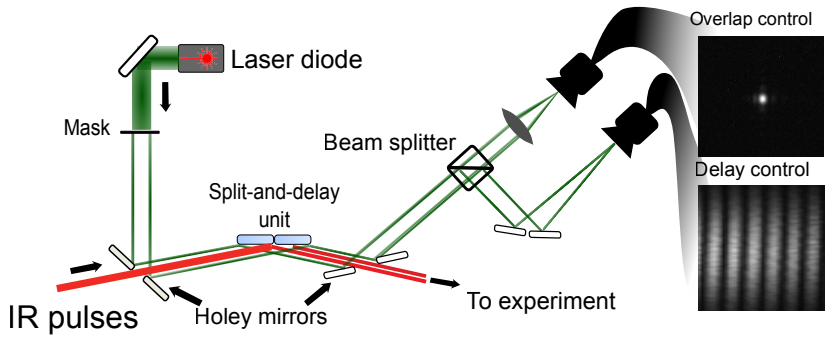

Figure 5.11: Setup utilized in the experiments described in this section. The SDU was operated at an angle of grazing incidence of 20°. Modified from Paper **V**.

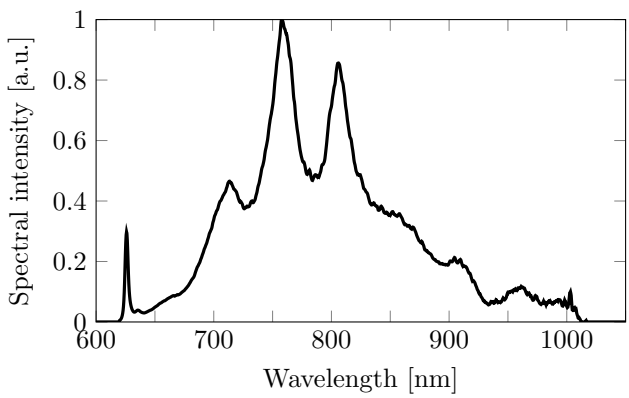

Figure 5.12: Spectrum of the laser used for autocorrelation measurements. The spectral width of about 300 nm supports few-cycle pulses with a duration down to 6 fs. Reproduced from Paper **V**.

slight disagreement between the two curves can be explained by effects such as angular chirp which may lead to a distorted version of the original spectrum propagating through the pinhole, and the performance of the anti-reflection coating, which was not designed for this spectral bandwidth and the angle of incidence utilized.

The setup shown in Figure 5.11 was then changed to allow a second-order autocorrelation to be performed. The pinhole was replaced with a second-harmonic generation crystal and the signal was recorded with a fiber-coupled spectrometer instead of the photodiode. A small beam stop was placed in the center of the beam after the second-harmonic generation crystal to suppress the contribution of the intensity autocorrelation component, which is preferentially emitted in the forward direction. The wavelength-dependent signal is not shown here, but it is reported in Paper **V**. Figure 5.14 shows the wavelength-integrated signal in the spectral range between 370 nm and 450 nm, and for two different pulse durations. The range of wavelengths included in the integration was chosen to exclude the contribution to the second harmonic from the narrow spectral feature at 625 nm, which produces a long temporal contribution,

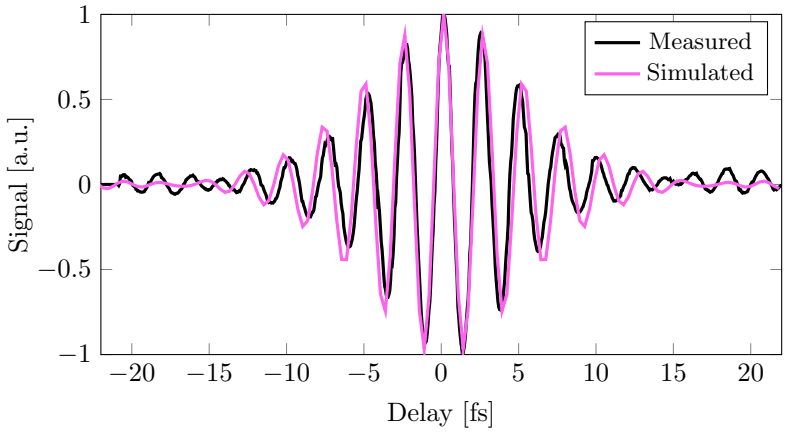

Figure 5.13: Measured and simulated field autocorrelation traces. The average was subtracted from the measured trace as it constitutes a background that arises from the energy reaching the photodiode when the two pulses are not overlapped in time. Since the recorded spectrum does not have a zero-frequency component the average of its Fourier transform is zero. Reproduced from Paper **V**.

and to suppress the contribution from the fundamental beam not converted during the second-harmonic generation process.

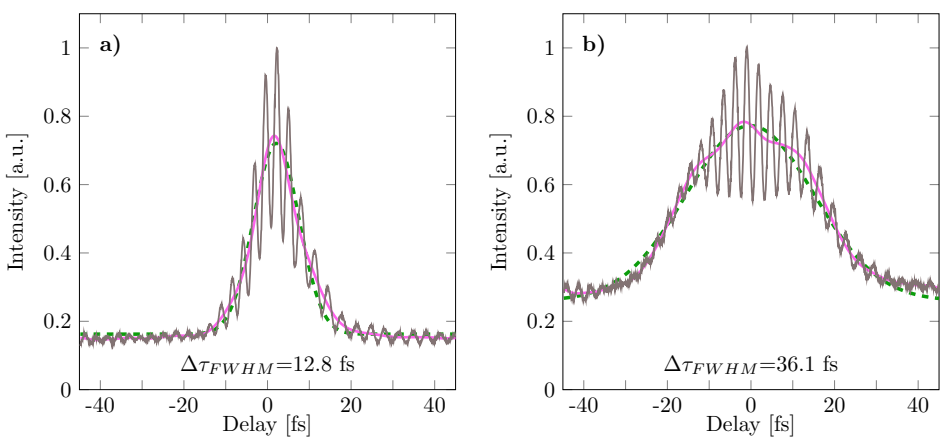

Figure 5.14: Wavelength-integrated signals of the second-order autocorrelation (grey lines), their low-frequency component (purple lines), and gaussian fits (green dashed lines), for pulses of two different durations: 6.2 fs (a) and 30 fs (b). The pulse durations were measured with the d-scan technique [100]. The two panels show the FWHM of the gaussian fits, which, after deconvolution, provide an estimate of the pulse durations: 9.1 fs and 25.5 fs, respectively. Reproduced from Paper **V**.

The traces exhibit the features of a second-order interferometric autocorrelation, and it is therefore possible to extract the low-frequency component applying a low-pass filter to their Fourier transforms, as described in Section 2.3.3. This results

in the corresponding second-order intensity autocorrelation traces. It is possible to estimate the pulse duration by fitting a gaussian profile to the traces and applying a deconvolution factor. The resulting pulse duration is slightly overestimated in the case of the shorter pulse, and slightly underestimated in the case of the longer pulse. This can be due to a bandwidth narrowing during the second-harmonic generation process, leading the transform-limited pulse to stretch and the chirped pulse to shorten.

5.3.2 Above-threshold ionization of argon

The first experiment conducted with the SDU integrated in the intense XUV beamline employed IR pulses. The pulses were used to induce ATI in argon, and ions were detected with the VMI spectrometer described in Section 4.2. The signal was the result of the accumulation of 200 shots per delay point, in steps of 100 as. The rms stability of the delay was about 50 as. Figure 5.15a shows the total yield of all the positive ions, i.e. not only Ar^+, Ar^{2+}, and Ar^{3+}, but also all the background gases present in the chamber, such as H_2O^+, $N_2{}^+$, and $O_2{}^+$.

Figure 5.15b shows the Fourier transform of the signal, which exhibits a clear peak at a frequency of 0.375 fs^{-1}, corresponding to the carrier frequency of the IR pulses. This confirms the precision of the SDU in setting the required delay, as any deviation from the required delay would introduce a shift in the periodicity of the oscillations. This experiment essentially constitutes a high-order autocorrelation of the IR pulses, although it is not possible to estimate the duration of the pulses. In fact, from the signal in Figure 5.15a, it is possible to observe the effect of the envelope, but the total range of the delay is not sufficiently long to fit a gaussian profile to the experimental curve.

For a 45 fs long gaussian pulse, a second-order autocorrelation is about 63 fs wide, and a higher-order autocorrelation is even shorter, therefore the envelope of the experimental curve was expected to show a substantial decrease within the delay range of 55 fs. However, the exact duration of the pulses during this experiment is not known. There are several reasons to expect the IR pulses to have been significantly longer: the pulse duration is measured before they propagate through a lens, a waveplate, and a vacuum window, and the dispersion introduced by the coating on the silica plates on the SDU is not known. Furthermore, while the coating was designed for s-polarized radiation, the pulses employed in this experiment were p-polarized. In fact, had they been s-polarized, they would have not carried sufficient energy to perform ATI because of the low reflectivity of the silica plates.

5.3.3 Delay-dependent XUV intensity distribution in the focus

The microscope described in Section 4.2 was employed to measure the intensity distribution generated by the interference of two XUV replica pulses, generated in argon and split by the SDU, in the focal plane. The camera utilized did not allow for the acquisition of single-shot images, therefore the exposure time was set to 30 s and the images are the result of the accumulation of 300 laser shots. Images were acquired at delay points with a relative separation of 100 as, over a total range of about 7 fs. The multi-shot acquisition resulted in images blurred due to pointing instabilities, as already discussed in Section 4.2.3.

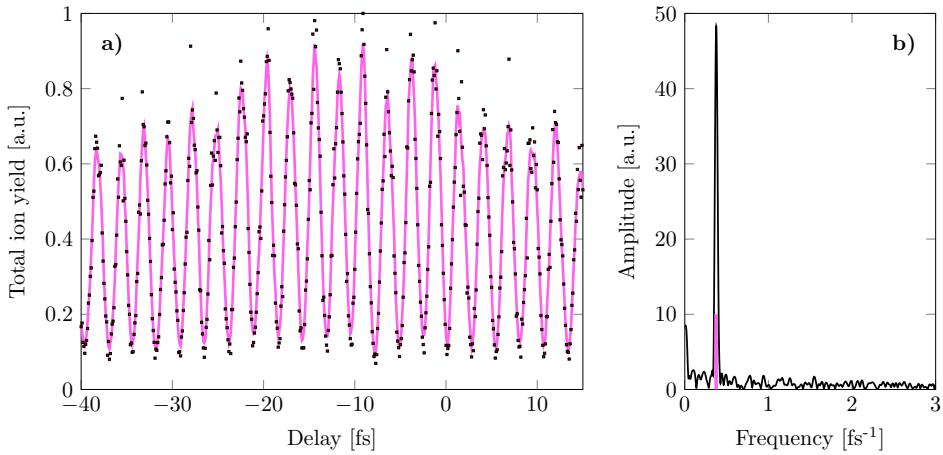

Figure 5.15: a) Total ion yield as a function of the delay between the two IR replica pulses. The grey dots are the experimental data points resulting from the accumulation of 200 shots of the laser, and the purple line is the curve obtained applying a running average between 3 consecutive points. The values of the delay should be interpreted as relative since it is not know where the zero is. b) Fourier transform of the purple curve in (a). The component at zero frequency has been subtracted. The purple line represents the carrier frequency of the IR pulses, whose spectrum is centered at 800 nm.

The sharp features that arise from destructive interference of two pulses delayed, e.g., by π, are smoothened by pointing instabilities. In fact, the dark fringe, characteristic of destructive interference, typically spans a small portion of the intensity distribution, and each shot of the laser hits the scintillation crystal with an rms precision of approximately 10% of the intensity distribution. The resolution of the microscope, estimated to be 2 µm, is not sufficient to resolve very sharp features. Furthermore, the interference patterns shown in Figure 5.10 are simulated for only one wavelength. The interference generated by each harmonic order, q, exhibits clear destructive interference only at delays that are odd integer multiples of T/2q (where T is the period of the fundamental IR wavelength). In other words, the interference from different harmonic orders is in phase only at delays that are integer multiples of T/2. To demonstrate this concept it is useful to consider Figure 5.16. This figure shows the transverse position of the center of mass of the intensity distribution in two cases: IR pulses (black line), and XUV pulses (purple line) comprising harmonic orders 13 through 31. The position of the center of mass of the XUV distribution closely follows that of the IR distribution around the delays where the two curves cross the zero, while it significantly deviates from that of the IR distributions at other delays. This can be seen in the insets: a) shows the lineouts of the IR and XUV distributions at T=0, b) shows those at T=0.25, and c) shows those at T=0.5. From the same figure it is possible to infer that the expected periodicity of the position of the center of mass is twice the periodicity of the IR field.

Figure 5.17a shows the position of the center of mass of the recorded intensity distributions, as a function of the delay. Figure 5.17b presents the Fourier transform of such a curve, showing a clear peak at 0.75 fs^{-1}, which is twice the periodicity of the

IR field, as expected.

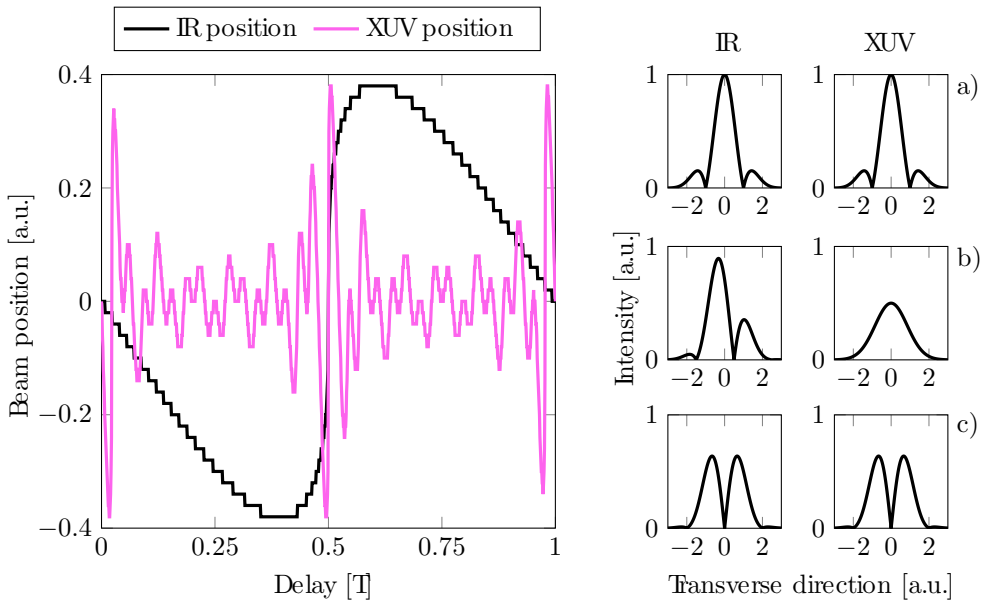

Figure 5.16: Position of the center of mass of the intensity distribution generated by the interference between two replica pulses of an IR pulse (black line) and an XUV pulse (purple line). The x-axis is expressed in units of the oscillation period of the carrier frequency of the IR pulse. a-c) IR and XUV distributions at the focal plane, at delays corresponding to 0, 0.25 T, and 0.5 T, respectively.

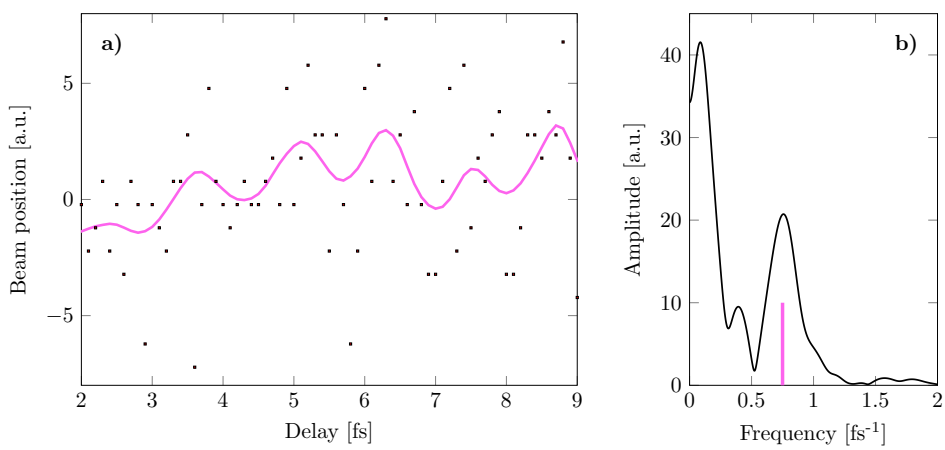

Figure 5.17: a) Position of the center of mass of the intensity distribution measured with the XUV microscope. The gray dots are the experimental data points, resulting from the accumulation of 300 laser shots. The purple line is the result of a 5-point running average. b) Fourier transform of the smoothened purple curve in panel (a). The purple line indicates the frequency corresponding to twice the laser periodicity.

Chapter 6

Summary and Outlook

The experiments presented in this thesis constitute significant steps towards performing attosecond XUV pump-probe experiments in atoms and molecules. The aim of such experiments is to reveal the ultrafast charge dynamics taking place on the attosecond timescale. Two main enabling technologies are required to perform a pump-probe experiment: a device that is able to split an incoming pulse into two replicas and to introduce a stable and reliable delay between them, and a detector that is able to collect the products of the photoionization process. The split-and-delay unit was the main focus of this thesis, and it has been tested in the experiments described in Paper **V**. It was also modified to suit the requirements of the beamline at the Extreme Light Infrastructure, which is described in Paper **VI**. The detector is a double-sided velocity map imaging spectrometer, and is described in Section 4.2 and in Paper **VII**. It allows the detection of both electrons or negative fragments and positive fragments, at the same time.

High intensity is required when performing a pump-probe experiment to ensure that photons from both the pump and the probe pulses interact with the same target. Various approaches were used to increase the intensity in the interaction region, namely: increasing the energy of the generated XUV pulses, decreasing the duration of these pulses, and achieving the smallest possible distribution of the intensity at the focus. These approaches are recapitulated below.

- **Generation of high-energy pulses.** The XUV pulses were generated via the HHG process. The process was macroscopically optimized in the experiment described in Paper **I** by investigating the phase-matching conditions. The focusing geometry was extended to utilize more energy in the IR driving pulses. This approach was adopted in the experiments reported in Paper **II**, where the XUV pulses were shown to reach sufficiently high intensities to induce a non-linear absorption process in neon.

- **Generation of shorter pulses.** A pulse post-compression scheme was applied to the driving IR pulses as a means of broadening their spectrum, which led to a threefold decrease in their duration. These pulses were then used to drive the

HHG process, which resulted in a significant extension of the generated cutoff. These results are presented in Paper **III**.

In a proof-of-principle experiment conducted on this beamline, the output of the grating compressor was sent to an interferometer. The interferometer was designed in such a way that the output of the two arms are spatially and temporally separated. The two outgoing pulses, propagating parallel to each other but displaced laterally, were sent to the IR focusing optics, which in this case was a spherical mirror with a focal length of 4 m. This causes the two pulses to overlap in the focal plane in the generation cell with a small crossing angle. By finely tuning their relative delay it was possible to angularly streak different XUV pulses. While the generated XUV spectra were more continuous than those generated with a standard geometry, no clear footprint of an extended continuum that would support an IAP was observed. This preliminary experiment paved the way for the experiment described in Paper **IV** where the data acquired at a different beamline are reported.

- **Optimization of focusing conditions.** Two main tools have been employed to characterize the intensity distribution in the XUV focus and to optimize the alignment of the Wolter focusing optics (described in Section 4.3.2): an XUV microscope, described in Section 4.2, and an XUV wavefront sensor. The latter was found to be an extremely useful tool, as described in Paper **VIII**, both for characterization and optimization of the focus. A wavefront sensor, recently developed by the group, is currently being tested and will be integrated in the beamline in the near future.

Attempts to perform XUV pump-probe experiments in neon were also made, but no clear delay dependence was found. This was mainly attributed to long-term instabilities of the driving IR laser, such as pointing and energy fluctuations. In fact, during the non-linear ionization experiments reported in Paper **II**, less than one doubly-charged neon ion was detected for each laser shot, and accumulation of data over a few tens of thousands shots was required, resulting in acquisition times of a few tens of minutes. A pump-probe trace would exhibit oscillations characterized by low contrast, thus requiring long acquisition times for every data point, each corresponding to a different delay. To record a trace over a range of several femtoseconds with high temporal resolution, excellent stability is thus required over several hours. While a different transport scheme of the IR pulses is currently being implemented to reduce pointing instabilities, energy fluctuations lead to different XUV spectral distributions and energies to be generated at each shot. A solution to circumvent this problem is suggested in the next section.

6.1 Further developments

Constructing, optimizing, and constantly upgrading a beamline for XUV attosecond pump-probe experiments are formidable tasks that require years of collective efforts. These tasks have been carried throughout the present work alongside scientific experiments, that had already shown the possibility of performing high-intensity XUV experiments on this beamline. Tests have been performed confirming the viability of

the pump-probe setup for the study of atomic and molecular dynamics, but there is always room for improvement of the tools available. Some planned developments are discussed in the rest of this section.

A prototype of an XUV wavefront sensor has recently been constructed, and reconstruction software has been developed in-house. These have proven to be satisfactory, and together will provide a powerful diagnostic tool on the beamline in the near future. Apart from the applications of an XUV wavefront sensor already described, such as characterization and optimization of the focus, two other applications are worth mentioning.

The importance of focal overlap in pump-probe experiments was addressed in Chapter 5, where it was stated that it can be evaluated to some extent with the current detection tools. The wavefront sensor can provide a more precise method of achieving and, most importantly, assessing the focal overlap on a single-shot-basis. The idea is that, once the distance between the sensor and the focal plane is known, it is expected that knowledge of only the centers of mass of the far-field intensity distributions of the two XUV replicas and the four tilt terms in their wavefront decomposition (one x-tilt and one y-tilt component per half wavefront), will be sufficient to evaluate the position of the two foci in the focal plane. The difference in position in the two transverse directions can constitute the two error functions for the PIDs controlling the piezoelectric actuators of the SDU during an automated alignment routine. They could potentially also be used to stabilize the focal position.

Another improvement that the wavefront sensor could bring to the beamline is actually due to the camera integrated in the sensor. Overall pointing instabilities in the beamline cause pulses to impinge on the optics of the SDU at different positions at each shot, and therefore to be split unevenly. The interference arising from two pulses was described in detail in Section 5.2. If the splitting ratio of the two pulses is uneven, the expected dark fringes originating from destructive interference will be washed out. In fact even if the phase difference between the two pulses is π, if they carry different energies their combined intensity will never be zero at any point in space. This effect is expected to reduce the contrast in a time-dependent signal. If the actual splitting ratio is recorded on a single-shot basis, it is possible to tag each data point recorded in an experiment with its respective splitting ratio. It would then be possible to either discard the data points that exhibit a ratio above an arbitrary threshold, or to assign a different weight to them. Such tagging can be achieved by integrating the signal over the two halves of the energy-calibrated camera that records the diffraction patterns in a wavefront sensor, thus providing the intensity ratio between the two half wavefronts.

This tagging technique can be particularly useful in combination with the double-sided VMI spectrometer and the covariance analysis technique. The spectrometer is able to acquire different kinds of information at the same time, such as both electron and ion initial kinetic energies and TOF spectra. Covariance analysis can unravel the correlations between different observables, e.g., the amplitude of a given peak in the TOF spectrum with different regions of a velocity map image, thus showing the initial kinetic energy of ions characterized by that specific mass/charge ratio. If a certain parameter, such as the intensity of the XUV pulses, is unstable during the acquisition of the data, partial covariance can be applied. Partial covariance takes into account the variation in the parameter by assigning a different weight to data collected from different laser shots. Such an analysis technique was employed in the experiments reported in Paper **VII**. In a pump-probe experiment the splitting ratio can constitute

a parameter that varies on a shot-to-shot basis, and must therefore be corrected for.

Examples of other improvements from which pump-probe experiments would benefit are: the implementation of spectral discrimination of the XUV pump and probe pulses with two different metallic filters, the acquisition of single-shot energy-calibrated spectra directly after the interaction region, the availability of IAPs, and the possibility of aligning molecules in the gas jet before the pump pulse reaches them. The generation of IAPs via two-color generation is currently being investigated, and an IR interferometer for molecular alignment has already been designed and will be integrated in the beamline in the near future.

Appendix - Raytracing

Although an extensive and detailed description of the principles of raytracing lies outside the scope of this this, raytracing is a powerful tool which was utilized widely throughout the entire project as an aid in designing and characterizing various optical components required in the development of the beamline. Therefore a few basic concepts of raytracing are presented here, together with a description of the software used to carry out reliable simulations of the behavior of the main components in a physical situation.

As its name suggests, raytracing is concerned with tracing rays of light, and thus it has its place in in the geometrical optics framework [117]. In principle, it is always possible to trace a ray, as only two simple laws are required to obtain a complete description of the system: the law of reflection and Snell's law of refraction. If more than one ray is traced from the same point, it is easy possible to determine whether, and where, these rays intersect, defining the position of the image at the object point.

It may thus appear that it is easy to simulate a complete optical system, however, the simulation of a large optical system, such as an entire beamline, or possibly, a real experiment is, in fact, extremely laborious. The question at this point is whether or not an exact simulation is needed, as this might require a considerable amount of computational power. As is often tha case in physics, the answer depends on the purpose of the simulation, hence different kinds of raytracing are available, and are applied for different purposes.

There are two main approaches to raytracing, namely exact raytracing and approximate raytracing. The latter, as the name suggests, is employed in particular when there is no need for a complete description of the image formed by the rays, and it is usually carried out with a first- or third-order approximation. The first-order approximation is also known as the paraxial approximation. The order of the approximation refers to the order of the Taylor expansion used when calculating the refraction at a given interface, according to Snell's law: $\sin\theta \approx \theta - \theta^3/3! + ...$

Paraxial raytracing is used to assess the basic properties of an optical system, primarily where the image will be formed, and how large it will be, and to estimate the kind of aberrations expected in an optical system. The calculations are simplified significantly by using the first order approximation, and can even be performed manually.

Third-order raytracing provides knowledge about the origin and degree of various types of aberration in the optical system, while still providing a simplified version of

the calculations needed. This is very useful when designing an optical system to help the designer understand what kind of measures are needed to reduce the aberrations. However, when an exact prediction of the aberrations and the overall performance of the optical system is needed, an exact raytracing procedure must be used, and thus software is required. Not only are the calculations in this case much more demanding, but also the number of rays that have to be traced increases with the increasing degree of precision required.

In the work described in this thesis, the raytracing software FRED^{TM} from Photon Engineering was used. FRED is an exact ray tracing program, which uses a gaussian beam decomposition (GBD) approach to compute coherent fields as a synthesis of different individual gaussian beamlets [118]. The working principle, as stated in the application notes provided by the developers, is that when creating a coherent light source, e.g. a laser beam, a grid of an arbitrary number of points is created across the beam cross section. Each point in the grid serves as the origin for a base ray that is traced along the axis of each individual ray. By default, the software assigns eight secondary rays to the base ray, four for each transverse dimension, whose relationship with the base ray allows the computation of the beam waist and beam divergence at any given plane along the direction of propagation of the beam.

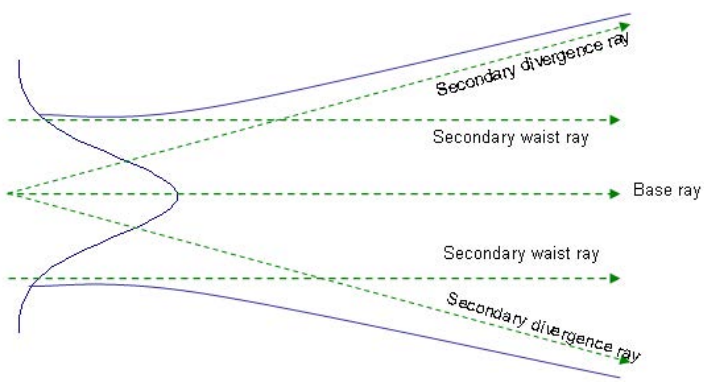

Figure 1: A base ray and two in plane pairs of secondary rays. Reproduced from FRED help files.

Figure 1 shows the base ray and the four secondary rays in one plane; four additional secondary rays lie in the orthogonal plane. The waist rays are initially traced parallel to the base ray, at a distance which is internally calculated in order to obey the laws governing gaussian beams, starting from the far-field divergence (θ), given as an input parameter by the user. The divergence rays originate coincidently with the base ray, and follow a trajectory asymptotically to the far-field divergence angle. The beam waist obtained by means of the secondary waist rays (w_0), and the divergence angle satisfy the relationship:

$$\tan\theta = \lambda/(\pi w_0). \tag{6.1}$$

Furthermore, within the framework of FRED, it is possible to design an arbitrary

optical system, thanks to several basic optical components present as built-in functions in the software. An additional degree of freedom is afforded by allowing the user to define an arbitrary optical component by means of an equation defined surface, in order to introduce less commonly used optics, such as a toroidal mirror. It is also possible to define different materials, apart from those given in a catalogue, together with their optical properties, as well as different kinds of coatings, in order to simulate the effects of multilayers, by defining their specific optical behavior in terms of reflectivity and transmission. Most important of all, several analysis surfaces can be created, to simulate the presence of different cameras to visualize the intensity distribution and the positions of the rays.

Coherent field synthesis, carried out by means of GBD, enables the computation of interference, as each of the beamlets carries the phase of the beam. In this way, interference phenomena can be simulated to a high degree of precision, as well as diffraction patterns from different configurations. This option, together with the possibility of writing scripts, allows, for example, the simulation of autocorrelation traces, or the theoretical output of any kind of real experiment that could be performed in reality with the optical system in question. It is also possible to interface other scripts in the FRED framework written with software such as Matlab.

Comments on the papers

I **A high-flux high-order harmonic source**
We present the high-flux source based on high-order harmonic generation in gases, showing the generation of XUV pulses approaching with energy 1 µJ. We also discuss a theorethical model for scaling the parameters for generating harmonics with higher flux. At the start of my Ph.D. I participated to the final experiments and provided feedback on the manuscript. I did not perform any of the simluations.

II **Two-photon double ionization of neon using an intense attosecond pulse train**
In this paper we benchmark the HHG beamline in terms of generated and available flux of the harmonics, estimating a peak intensity as high as 3×10^{12} W/cm^2 through measurements of the focal spot. Furthermore, we present our results on two-photon double ionization of Ne showing the ability of our XUV pulses to initiate non-linear processes. I took part in this project with the design of the gas cell used for HHG, building up the beamline, and as one of experimental investigators. Furthermore I provided raytracing simulations of the expected XUV profile in the focus and contributed with feedback to the manuscript.

III **Compression of TW class laser pulses in a planar hollow waveguide for applications in strong-field physics**
We present a post-compression scheme for high energy pulses and demonstrated sub-15 fs durations. I had a major role in building up the HHG setup used to test the application of post-compressed pulses, and a minor role in the experiments involving the planar hollow waveguide.

IV **Gating attosecond pulses in a noncollinear geometry**
We show the first experimental implementation of the noncollinear optical gating technique, allowing for the production of isolated attosecond pulses, angularly separated from the driving laser field. I had a minor experimental role, participating in the proof-of-concept experiments.

V **Design and test of a broadband split-and-delay unit for attosecond XUV-XUV pump-probe experiments**
We present the design and the preliminary tests of the split-and-delay unit and its active stabilization scheme. I have designed, commissioned, and assembled the mechanical mount of the split mirror, I designed the stabilization feedback system, and performed extensive simulations on it. I also helped in analysing the data recorded during the tests and wrote the manuscript. I did not perform the preliminary tests.

VI **The ELI-ALPS facility: the next generation of attosecond sources**
In this topical review we present the different beamlines that are planned at the ELI-ALPS facility. I contributed to the design of the beamline related to the Lund group by helping to adapt the pump-probe setup, which I designed and implemented at the Lund Laser Centre, for use at ELI-ALPS.

VII **A Versatile Velocity Map Electron-Ion Covariance Imaging Spectrometer for High Intensity XUV Experiments**
In this manuscript we report on the design and first performance tests of a newly developed two-sided velocity map imaging spectrometer. I experimantally contributed to the data acquisition both at the intense XUV beamline at the Lund Laser Centre and at the synchrotron radiation facility Max-lab. I did not contribute to the simulations. I contributed to the manuscript with feedback.

VIII **Micro-focusing of broadband high-order harmonic radiation by a double toroidal mirror**
In this manuscript we report experiments aiming at optimizing the focusing conditions in the beamline. I contributed to the project by acquiring hands-on experience with the wavefront sensor utilized in previous experiments not reported here. I did not perform the experiments with the XUV microscope. I also characterized the focusing optics, both with extensive raytracing simulations and experimentally. I set up and performed raytracing simulations of the resulting wavefronts. I did not analyze the output of these simulations. I contributed to writing portions of the manuscript and provided feedback on the rest of it.

Acknowledgements

My career at Atomic Physics has been similar to the research presented in this thesis and the process of writing it: it had many different chapters, it led to some frustration at times, but in the end was extremely satisfactory. Many people have accompanied me on the unpredictable scientific and personal path that resulted in this thesis, and I would like to explicitily thank many of them here.

First and foremost, I would like to express my sincere gratitude to my main supervisor, Per Johnsson, although I don't really know where to start. You have been very understanding and patient all along, guiding me through difficulties that arose along the way. I have also learned a lot about physics, and science in general, from you. Your fast thinking and your problem-solving skills have always been a source of inspiration. I think our memories of the conference in Banff will always delight us with a quite funny anecdote.

I would also like to thank to my co-supervisor and group leader, Anne L'Huillier, who gave me the chance to join this amazing group. I remember your very interesting and engaging lectures in light-matter interaction, and your explanations at various meetings. I believe that you have made a significant contribution to the environment of the Division of Atomic Physics, especially the Atto-group, as well as making in a pleasant place to work. You are also proof that it is possible to lead a highly regarded research group with humility and humanity.

I would also like to thank the head of the Atomic Physics Division, Claes-Göran Wahlström. Although we did not have much contact, you have always been available for important issues, and it is thanks to you that this project was concluded in the way it was.

To my old office-mates, Piotrek and Marija: well, what fun we had! The office recently turned into a coffee room, but it will always remind me of all the conversations we had and the new "words" (ehm) Marija taught us. To my new office-mates, "make optics great again" Hampus and the little Coca-Cola fridge, who witnessed the entire process of writing this thesis: thanks for the cold company (Hampus) and the laughter (the fridge)!

Work in the lab without colleagues would be all frustration and having no one to share the joy of the results with. For this reason I would like to thank the three generations of "10 Hz people" I have worked with: "principessa" Fernando, Christoph, Byunghoon, and Piotr; "beer-bear-beer" Linnea and Bastian; "hipster-mustache" Sylvain, Jan, Jasper, Hélène, and Hampus; not forgetting the guests and master's students

Hugo, Emma, Fabian, and Balasz x3. None of these results would have been achieved without the laser, and the laser is unhappy unless Anders is around. If the laser is unhappy we are all unhappy. Thanks Anders for keeping the laser happy, and for teaching us the secrets to making it a little less sad when you are on vacation!

Among all the other people who work, and have worked, in the Atto-group, a special mention goes to Stefanos for all the IT support he provided over the years, and for tolerating my playful meaningness (to be interpreted as me being mean). I feel old when I think about all the people that I should mention here, whom I wish I had more time and space to thank. I don't want to offend anybody, so I will mention them in the most random order possible: Cord, Johan, Miguel, Diego, Anne, Chen, Kathrin, Mathieu, David, Neven, Marcus, Shiyang, Samuel, Yu-Chen, Erik, Lana, Eleonora, Jana, David, Erik, Diana, Isabel, Lovisa, Jenny, Saikat, Emma, Maité, Sara, and whoever I might have omitted.

My project was partly supported by the Marie Curie program ATTOFEL (ITN), through which I have met several people with whom I have shared interesting meetings and an unforgettable winter school in Bormio. It is thanks to ATTOFEL and the support of Marc Vrakking and Arnaud Rouzèe that I could spend two fruitful months working at the Max-Born Institut in Berlin.

The work environment I have experienced has been amazing, and the entire division seems to run smoothly and without troubles. This is thanks to the "invisible" work of the technical and administrative staff: Anne, Bertil, Camilla, Harriet, Jakob, and Åke.

I seem to have spent most of my life studying, and the result is this thesis. However, everyone I have ever met has contributed to it in one way or another. I do not need to name them individually, because they know who they are. One exception is Caroline, whom I would like to thank, *bigly*.

Grazie ai miei genitori per il sostegno in tutti questi circa venticinque anni di istruzione, mentre eravamo vicini e lontani. Per non avermi giudicato quando pensavo di non voler arrivare alla fine di questo percorso, anche se sono sicuro che siete contenti che abbia cambiato idea!

Bedankt voor alles, Pauline. May I repay you throughout your Ph.D. with the same support you have given me during mine. I am sure you will also succeed, thrive, and make me proud!

Finally, the biggest "miao meow miauw pur-pur" goes to Olof and Stella, the best seal and fox in the world!

Mischievous Outlook

I would like to lay out a further outlook by describing a conceptual pump-probe experiment, despite its complicacy. I have been working hard (or hardly working?) on this idea in my free time.

Communication can take different forms, and manifests itself through the macroscopic movement of muscles (lips, tongue, vocal cords, hands, and arms). Long before these structural dynamics take place (on the millisecond timescale), charge dynamics play an important role. Ions move out of cells to form synapses in the motor cortex, which in turn set charges in motion in the peripheral nervous system, which then

regulates the structural changes. As we learned throughout this thesis, it would take a high-resolution pump-probe experiment to resolve these charge dynamics.

The setup is as follows: take an Italian sample, and initiate the dynamics with a pump event. For example say: "I like ketchup and escargot on my pineapple pizza". Take a photograph of the system at a certain delay. Make sure that you run away before the end of the dynamics, needless to say why. Find another sample and repeat the procedure, but with a different delay, until you have collected enough frames to reconstruct the dynamics. Figure 2 is the result of a proof of principle of such experiments.

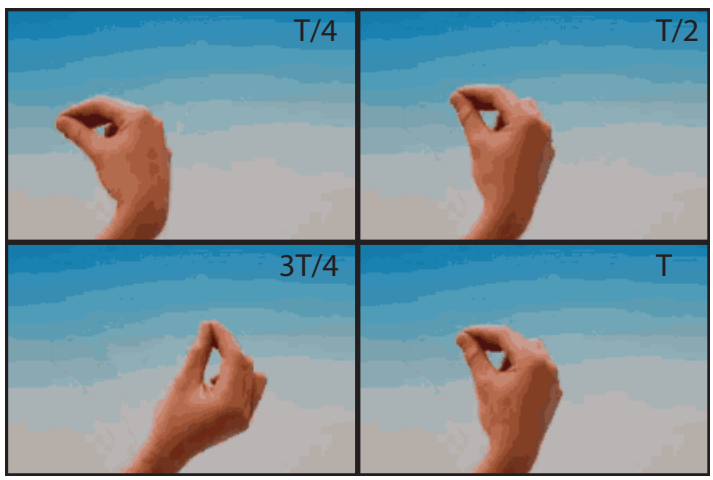

Figure 2: Four snapshots of ketchup-and-escargot-on-pizza-induced Italian dynamics. T is the oscillation period, which depends on the system. T is generally smaller when the system is more highly excited.

Despite the difficulty in interpretation, I was able to decipher the underlying message through a collaboration with Campi et al. It reads something along the lines of "That's all folks. Thank you all so much!". An intriguing data analysis revealed the hidden message "Babidibubidi", whose precise interpretation is still open to debate. The next Ph.D. project...

References

1. S. von Stumm, B. Hell and T. Chamorro-Premuzic. *The Hungry Mind.* Perspectives on Psychological Science **6**, 574–588 (2011).

2. M. J. Gruber, B. D. Gelman and C. Ranganath. *States of Curiosity Modulate Hippocampus-Dependent Learning via the Dopaminergic Circuit.* Neuron **84**, 486–496 (2017).

3. G. P. Urcelay and R. R. Miller. *On the generality and limits of abstraction in rats and humans.* Animal cognition **13**, 21–32 (2010).

4. T. R. Kane and M. P. Scher. *A Dynamical Explanation of the Falling Cat Phenomenon.* International Journal of Solids and Structures **5**, 663–670 (1969).

5. E. Gutierrez, D. B. Quinn, D. D. Chin and D. Lentink. *Lift calculations based on accepted wake models for animal flight are inconsistent and sensitive to vortex dynamics.* Bioinspiration & Biomimetics **12**, 016004 (2016).

6. Bret W Tobalske. *Biomechanics of bird flight.* Journal of Experimental Biology **210**, 3135 LP – 3146 (2007).

7. M. Marey. *Photographs of a tumbling cat.* Nature **51**, 80–81 (1894).

8. J. J. Thomson. *XXIV. On the structure of the atom: an investigation of the stability and periods of oscillation of a number of corpuscles arranged at equal intervals around the circumference of a circle; with application of the results to the theory of atomic structure.* Philosophical Magazine **7**, 237–265 (1904).

9. C. Th. J. Alkemade. *Single-Atom Detection.* Applied Spectroscopy **35**, 1–14 (1981).

10. F. E. Lytle, R. M. Parrish and W. T. Barnes. *An Introduction to Time-Resolved Pump/Probe Spectroscopy.* Applied Spectroscopy **39**, 444–451 (1985).

11. J. M. Richter, F. Branchi, F. V. A. Camargo, B. Zhao, R. H. Friend, G. Cerullo and F. Deschler. *Ultrafast carrier thermalization in lead iodide perovskite probed with two-dimensional electronic spectroscopy.* Nature Communications **8**, 376 (2017).

12. R. Kienberger, E. Goulielmakis, M. Uiberacker, A. Baltuska, V. Yakovlev, F. Bammer, A. Scrinzi, Th. Westerwalbesloh, U. Kleineberg, U. Heinzmann, M. Drescher and F. Krausz. *Atomic transient recorder.* Nature **427**, 817 (2004).

13. A. McPherson, G. Gibson, H. Jara, U. Johann, T. S. Luk, I.A. McIntyre, K. Boyer and C. K. Rhodes. *Studies of multiphoton production of vacuum-ultraviolet radiation in the rare gases.* J. Opt. Soc. Am. B **4**, 595 (1987).

14. M. Ferray, A. L'Huillier, X. F. Li, L. A. Lompre, G. Mainfray and C. Manus. *Multiple-harmonic conversion of 1064 nm radiation in rare gases.* J. Phys. B **21**, L31 (1988).

15. T. Popmintchev, M.-C. Chen, D. Popmintchev, P. Arpin, S. Brown, S. Ališauskas, G. Andriukaitis, T. Balciunas, O. D. Mücke, A. Pugzlys, A. Baltuska, B. Shim, S. E. Schrauth, A. Gaeta, C. Hernandez-Garcia, L. Plaja, A Becker, A. Jaron-Becker, M . M. Murnane and H. C. Kapteyn. *Bright Coherent Ultrahigh Harmonics in the keV X-ray Regime from Mid-Infrared Femtosecond Lasers.* Science **336**, 1287–1291 (2012).

16. Will Durant. *The Story of Philosophy* (1926). ISBN 978-0-671-69500-2.

17. Press Release: The 1999 Nobel Prize in Chemistry (1999).

18. C. J. Giunta. *What's in a Name? Amount of Substance, Chemical Amount, and Stoichiometric Amount.* Journal of Chemical Education **93**, 583–586 (2016).

19. F. Remacle and R. D. Levine. *Attosecond pumping of nonstationary electronic states of LiH: Charge shake-up and electron density distortion.* Physical Review A **83**, 13411 (2011).

20. F. Remacle and R. D. Levine. *An electronic time scale in chemistry.* PNAS **103**, 6793 (2006).

21. F. Calegari, D. Ayuso, A. Trabattoni, L. Belshaw, S. De Camillis, S. Anumula, F. Frassetto, L. Poletto, A. Palacios, P. Decleva, J. B. Greenwood, F. Martin and M. Nisoli. *Ultrafast electron dynamics in phenylalanine initiated by attosecond pulses.* Science **346**, 336–339 (2014).

22. P Tzallas, E Skantzakis, L A A Nikolopoulos, G D Tsakiris and D Charalambidis. *Extreme-ultraviolet pump-probe studies of one-femtosecond-scale electron dynamics.* Nature Physics **7**, 781–784 (2011).

23. B Manschwetus, L Rading, F Campi, S Maclot, H Coudert-Alteirac, J Lahl, H Wikmark, P Rudawski, C M Heyl, B Farkas, T Mohamed, A L'Huillier and P Johnsson. *Two-photon double ionization of neon using an intense attosecond pulse train.* Phys. Rev. A **93**, 61402 (2016).

24. E. Takahashi, Y. Nabekawa and K. Midorikawa. *Generation of 10-μJ coherent extreme-ultraviolet light by use of high-order harmonics.* Opt. Lett. **27**, 1920 (2002).

25. E. J. Takahashi, P. Lan, O. D. Mücke, Y. Nabekawa and K. Midorikawa. *Attosecond nonlinear optics using gigawatt-scale isolated attosecond pulses.* Nature Communications **4** (2013).

26. J.-F. Hergott, M. Kovacev, H. Merdji, C. Hubert, Y. Mairesse, E. Jean, P. Breger, P. Agostini, B. Carré and P. Salières. *Extreme-ultraviolet high-order harmonic pulses in the microjoule range.* Phys. Rev. A **66**, 21801 (2002).

27. N. A. Papadogiannis, L. A. A. Nikolopoulos, D. Charalambidis, G. D. Tsakiris, P. Tzallas and K. Witte. *Two-photon ionization of He through a superposition of higher harmonics.* Phys. Rev. Lett. **90**, 133902 (2003).

28. K. Midorikawa, Y. Nabekawa and A. Suda. *XUV multiphoton processes with intense high-order harmonics.* Progress in Quantum Electronics **32**, 43–88 (2008).

29. P Tzallas, D Charalambidis, N A Papadogiannis, K Witte and G D Tsakiris. *Direct observation of attosecond light bunching.* Nature **426**, 267 (2003).

30. T. Shimizu, T. Okino, K. Furusawa, H. Hasegawa, Y. Nabekawa, K. Yamanouchi and K. Midorikawa. *Observation and analysis of an interferometric autocorrelation trace of an attosecond pulse train.* Physical Review A **75**, 33817 (2007).

31. T. Okino, Y. Furukawa, Y. Nabekawa, S. Miyabe, A. Amani Eilanlou, E. J. Takahashi, K. Yamanouchi and K. Midorikawa. *Direct observation of an attosecond electron wave packet in a nitrogen molecule.* Science Advances **1** (2015).

32. P. A. Carpeggiani, P. Tzallas, A. Palacios, D. Gray, F. Martín and D. Charalambidis. *Disclosing intrinsic molecular dynamics on the 1-fs scale through extreme-ultraviolet pump-probe measurements.* Physical Review A **89**, 023420 (2014).

33. Yasuo Nabekawa, Yusuke Furukawa, Tomoya Okino, A Amani Eilanlou, Eiji J Takahashi, Kaoru Yamanouchi and Katsumi Midorikawa. *Sub-10-fs control of dissociation pathways in the hydrogen molecular ion with a few-pulse attosecond pulse train.* **7**, 12835 (2016).

34. Paraskevas Tzallas, D Charalambidis, N A Papadogiannis, Klaus Witte and George D Tsakiris. *Second-order autocorrelation measurements of attosecond XUV pulse trains.* Journal of Modern Optics **52**, 321–338 (2005).

35. M. Hentschel, R. Kienberger, Ch. Spielmann, G. A. Reider, N. Milosevic, T. Brabec, P. Corkum, U. Heinzmann, M. Drescher and F. Krausz. *Attosecond metrology.* Nature **41**, 509 (2001).

36. M. Drescher, M. Hentschel, R. Kienberger, G. Tempea, C. Spielmann, G. A. Reider, P. B. Corkum and F. Krausz. *X-ray Pulses Approaching the Attosecond Frontier.* Science **291**, 1923 LP – 1927 (2001).

37. I. J. Sola, E. Mével, L. Elouga, E. Constant, V. Strelkov, L. Poletto, P. Villoresi, E. Benedetti, J.-P. Caumes and S. Stagira. *Controlling attosecond electron dynamics by phase-stabilized polarization gating.* Nature Physics **2**, 319–322 (2006).

38. G. Sansone, E. Benedetti, F. Calegari, C. Vozzi, L. Avaldi, R. Flammini, L. Poletto, P. Villoresi, C. Altucci, R. Velotta, S. Stagira, S. De Silvestri and M. Nisoli. *Isolated Single-Cycle Attosecond Pulses.* Science **314**, 443–446 (2006).

39. J. Li, X. Ren, Y. Yin, K. Zhao, A. Chew, Y. Cheng, E. Cunningham, Y. Wang, S. Hu, Y. Wu, M. Chini and Z. Chang. *53-attosecond X-ray pulses reach the carbon K-edge.* Nature Communications **8**, 186 (2017).

40. G. Sansone, F. Calegari and M. Nisoli. *Attosecond Technology and Science.* Selected Topics in Quantum Electronics, IEEE Journal of **18**, 507–519 (2012).

41. T. H. Maiman. *Stimulated optical radiation in Ruby.* Nature **18**, 493 (1960).

42. R. N. Hall, G. E. Fenner, J. D. Kingsley, T. J. Soltys and R. O. Carlson. *Coherent Light Emission From GaAs Junctions.* Physical Review Letters **9**, 366–368 (1962).

43. F. J. McClung and R. W. Hellwarth. *Giant Optical Pulsations from Ruby.* Appl. Opt. **1**, 103–105 (1962).

44. R. W. Hellwarth. *Control of Fluorescent Pulsations.* In J R Singer, editor, *Advances in Quantum Electronics* page 334. Columbia University Press (1961).

45. L. E. Hargrove, R. L. Fork and M. A. Pollack. *Locking of He-Ne laser modes induced by synchronous intracavity modulation.* Applied Physics Letters **5**, 4–5 (1964).

46. A. J. DeMaria, W. H. Glenn Jr., M. J. Brienza and M. E. Mack. *Picosecond laser pulses.* Proceedings of the IEEE **57**, 2–25 (1969).

47. E. P. Ippen, C. V. Shank and A. Dienes. *Passive mode locking of the cw dye laser.* Applied Physics Letters **21**, 348–350 (1972).

48. C. V. Shank and E. P. Ippen. *Subpicosecond kilowatt pulses from a mode-locked cw dye laser.* Applied Physics Letters **24**, 373–375 (1974).

49. P. F. Moulton. *Spectroscopic and laser characteristics of Ti:Al2O3.* J. Opt. Soc. Am. B **3**, 125–133 (1986).

50. B. E. A. Saleh and M. C. Teich. *Fundamentals of Photonics.* John Wiley and Sons (2007).

51. F. Krausz and M. Ivanov. *Attosecond physics.* Rev. Mod. Phys. **81**, 163–234 (2009).

52. V. Lakshminarayanan and A. Fleck. *Zernike polynomials: a guide.* Journal of Modern Optics **58**, 545–561 (2011).

53. K. T. Kim, C. M. Kim, M.-G. Baik, G. Umesh and C. H. Nam. *Single sub-50-attosecond pulse generation from chirp-compensated harmonic radiation using material dispersion.* Phys. Rev. A **69**, 51805 (2004).

54. D. H. Ko, K. T. Kim and C. H. Nam. *Attosecond-chirp compensation with material dispersion to produce near transform-limited attosecond pulses.* Journal of Physics B: Atomic, Molecular and Optical Physics **45**, 74015 (2012).

55. D. Atwood. *Soft X-Rays and Extreme Ultraviolet Radiation.* Cambridge University Press (1999). ISBN 0-521-65214-6.

56. J.-C. Diels and W. Rudolph. *Ultrashort laser pulse phenomena.* Academic Press (1996).

57. P. M. Paul, E. S. Toma, P. Breger, G. Mullot, F. Augé, Ph. Balcou, H. G. Muller and P. Agostini. *Observation of a train of attosecond pulses from high harmonic generation.* Science **292**, 1689–1692 (2001).

58. P. B. Corkum and F. Krausz. *Attosecond science.* Nature Physics **3**, 381–387 (2007).

59. F. Frank, C. Arrell, T. Witting, W. A. Okell, J. McKenna, J. S. Robinson, C. A. Haworth, D. Austin, H. Teng, I. A. Walmsley, J. P. Marangos and J. W. G. Tisch. *Technology for Attosecond Science.* Review of Scientific Instruments **83**, 71101 (2012).

60. P. Agostini and L. F. DiMauro. *The physics of attosecond light pulses.* Rep. Prog. Phys. **67**, 813 (2004).

61. H Mashiko, A Suda and K Midorikawa. *All-reflective interferometric autocorrelator for the measurement of ultra-short optical pulses.* Applied Physics B **76**, 525–530 (2003).

62. E. Power, J. Pentland, J. Nees, C. P. Hauri, M. Merano, R. Lopez-Martens and G. Mourou. *All-reflective high fringe contrast autocorrelator for measurement of ultrabroadband optical pulses.* Optics Letters **31**, 3514–3516 (2006).

63. T. Gebert, D. Rompotis, M. Wieland, F. Karimi, A. Azima and M. Drescher. *Michelson-type all-reflective interferometric autocorrelation in the VUV regime.* New Journal of Physics **16**, 73047 (2014).

64. J. H. Eberly, Q. Su and J. Javanainen. *Nonlinear Light Scattering Accompanying Multiphoton Ionization.* Phys. Rev. Lett. **62**, 881 (1989).

65. X. F. Li, A. L'Huillier, M. Ferray, L. A. Lompré and G. Mainfray. *Multiple-harmonic generation in rare gases at high laser intensity.* Physical Review A **39**, 5751–5761 (1989).

66. Paul B Corkum. *Plasma perspective on strong field multiphoton ionization.* Phys. Rev. Lett. **71**, 1994 (1993).

67. K. J. Schafer, B. Yang, L. F. DiMauro and K. C. Kulander. *Above threshold ionization beyond the high harmonic cutoff.* Phys. Rev. Lett. **70**, 1599 (1993).

68. P. Agostini, F. Fabre, G. Mainfray, G. Petite and N. K. Rahman. *Free-Free Transitions Following Six-Photon Ionization of Xenon Atoms.* Physical Review Letters **42**, 1127–1130 (1979).

69. M. Lewenstein, Ph. Balcou, M. Yu. Ivanov, A. L'Huillier and P. B. Corkum. *Theory of high-harmonic generation by low-frequency laser fields.* Physical Review A **49**, 2117 (1994).

70. T. Popmintchev, M.-C. Chen, O. Cohen, M. E. Grisham, J. J. Rocca, M. M. Murnane and H. C. Kapteyn. *Extended phase matching of high harmonics driven by mid-infrared light.* Optics Letters **33**, 2128–2130 (2008).

71. A. L'Huillier and Ph. Balcou. *High-order harmonic generation in rare gases with a 1-ps 1053-nm laser.* Physical Review Letters **70**, 774–777 (1993).

72. F. Brizuela, C. M. Heyl, P. Rudawski, D. Kroon, L. Rading, J. M. Dahlström, J. Mauritsson, P. Johnsson, C. L. Arnold and A. L'Huillier. *Efficient high-order harmonic generation boosted by below-threshold harmonics.* **3**, 1410 (2013).

73. X. He, M. Miranda, J. Schwenke, O. Guilbaud, T. Ruchon, C. Heyl, E. Georgadiou, R. Rakowski, A. Persson, M. B. Gaarde and A. L'Huillier. *Spatial and spectral properties of the high-order harmonic emission in argon for seeding applications.* Phys. Rev. A **79**, 63829 (2009).

74. M. Lewenstein, P. Salières and A. L'Huillier. *Phase of the atomic polarization in high-order harmonic generation.* Phys. Rev. A **52**, 4747 (1995).

75. K. Varjú, Y. Mairesse, B. Carré, M. B. Gaarde, P. Johnsson, S. Kazamias, R. López-Martens, J. Mauritsson, K. J. Schafer, P. H. Balcou, A. L'huillier and P. Salières. *Frequency chirp of harmonic and attosecond pulses.* Journal of Modern Optics **52**, 379–394 (2005).

76. P. Balcou, P. Salières, A. L'Huillier and M. Lewenstein. *Generalized phase-matching conditions for high harmonics: The role of field-gradient forces.* Phys. Rev. A **55**, 3204–3210 (1997).

77. E. Constant, D. Garzella, P. Breger, E. Mével, Ch. Dorrer, C. Le Blanc, F. Salin and P. Agostini. *Optimizing High Harmonic Generation in Absorbing Gases: Model and Experiment.* Phys. Rev. Lett. **82**, 1668 (1999).

78. M Geissler, G Tempea and T Brabec. *Phase-matched high-order harmonic generation in the nonadiabatic limit.* Phys. Rev. A **62** (2000).

79. M. B. Gaarde, J. L. Tate and K. J. Schafer. *Macroscopic aspects of attosecond pulse generation.* J. Phys. B **41**, 132001 (2008).

80. C. M. Heyl, J. Güdde, A. L'Huillier and U. Höfer. *High-order harmonic generation with μJ laser pulses at high repetition rates.* Journal of Physics B: Atomic, Molecular and Optical Physics **45**, 74020 (2012).

81. Z. Chang and P. Corkum. *Attosecond photon sources: the first decade and beyond [Invited].* Journal of the Optical Society of America B **27**, B9–B17 (2010).

82. G. Sansone, L. Poletto and M. Nisoli. *High-energy attosecond light sources.* Nat Photon **5**, 655–663 (2011).

83. M. Chini, K. Zhao and Z. Chang. *The generation, characterization and applications of broadband isolated attosecond pulses.* Nat Photon **8**, 178–186 (2014).

84. E. Goulielmakis, M. Schultze, M. Hofstetter, V. S. Yakovlev, J. Gagnon, M. Uiberacker, A. L. Aquila, E. M. Gullikson, D. T. Attwood, R. Kienberger, F. Krausz and U. Kleineberg. *Single-cycle nonlinear optics.* Science **320**, 1614–1617 (2008).

85. A. Jullien, T. Pfeifer, M. J. Abel, P. M. Nagel, M. J. Bell, D. M. Neumark and S. R. Leone. *Ionization phase-match gating for wavelength-tunable isolated attosecond pulse generation.* Applied Physics B **93**, 433 (2008).

86. M. J. Abel, T. Pfeiffer, P. M. Nagel, W. Boutu, M. J. Bell, C. P. Steiner, D. M. Neumark and S. R. Leone. *Isolated attosecond pulses from ionization gating of high-harmonic emission.* Chemical Physics **366**, 9–14 (2009).

87. F. Ferrari, F. Calegari, M. Lucchini, C. Vozzi, S. Stagira, G. Sansone and M. Nisoli. *High-energy isolated attosecond pulses generated by above-saturation few-cycle fields.* Nat Photon **4**, 875–879 (2010).

88. G. Gademann, F. Plé, P.-M. Paul and M. J. J. Vrakking. *Carrier-envelope phase stabilization of a terawatt level chirped pulse amplifier for generation of intense isolated attosecond pulses.* Optics Express **19**, 24922–24932 (2011).

89. B. Shan, S. Ghimire and Z. Chang. *Generation of the attosecond extreme ultraviolet supercontinuum by a polarization gating.* Journal of Modern Optics **52**, 277–283 (2005).

90. P. Tzallas, E. Skantzakis, C. Kalpouzos, E. P. Benis, G. D. Tsakiris and D. Charalambidis. *Generation of intense continuum extreme-ultraviolet radiation by many-cycle laser fields.* Nature Phys. **3**, 846 (2007).

91. Z. Chang. *Controlling attosecond pulse generation with a double optical gating.* Physical Review A **76**, 51403 (2007).

92. H. Mashiko, S. Gilbertson, C. Li, S. D. Khan, M. M. Shakya, E. Moon and Z. Chang. *Double optical gating of high-order harmonic generation with carrier-envelope phase stabilized lasers.* Physical Review Letters **100**, 103906 (2008).

93. X. Feng, S. Gilbertson, H. Mashiko, H. Wang, S. D. Khan, M. Chini, Y. Wu, K. Zhao and Z. Chang. *Generation of Isolated Attosecond Pulses with 20 to 28 Femtosecond Lasers.* Physical Review Letters **103**, 183901 (2009).

94. H. Vincenti and F. Quéré. *Attosecond Lighthouses: How To Use Spatiotemporally Coupled Light Fields To Generate Isolated Attosecond Pulses.* Phys. Rev. Lett. **108**, 113904 (2012).

95. K. T. Kim, C. Zhang, T. Ruchon, J.-F. Hergott, T. Auguste, D. Villeneuve, P. Corkum and F. Quere. *Photonic streaking of attosecond pulse trains.* Nat Photon **7**, 651–656 (2013).

96. C. M. Heyl, S. N. Bengtsson, S. Carlström, J. Mauritsson, C. L. Arnold and A. L'Huillier. *Noncollinear optical gating.* New Journal of Physics **16**, 52001 (2014).

97. P. Lan, E. J. Takahashi and K. Midorikawa. *Optimization of infrared two-color multicycle field synthesis for intense-isolated-attosecond-pulse generation.* Physical Review A **82**, 53413 (2010).

98. C.-G. Wahlström, S. Svanberg, J. Larsson and A. Persson. *Lund high-power laser facility - systems and first results.* Physica Scripta **49**, 187 (1994).

99. F. Verluise, V. Laude, Z. Cheng, Ch. Spielmann and P. Tournois. *Amplitude and phase control of ultrashort pulses by use of an acousto-optic programmable dispersive filter: pulse compression and shaping.* Optics Letters **25**, 575–577 (2000).

100. M. Miranda, T. Fordell, C. Arnold, A. L'Huillier and H. Crespo. *Simultaneous compression and characterization of ultrashort laser pulses using chirped mirrors and glass wedges.* Opt. Express **20**, 688–697 (2012).

101. Ben C Platt and Roland Shack. *History and Principles of Shack-Hartmann Wavefront Sensing.* Journal of Refractive Surgery **17**, S573–S577 (2001).

102. M. Nisoli, S. De Silvestri and O. Svelto. *Generation of high energy 10 fs pulses by a new pulse compression technique.* Applied Physics Letters **68**, 2793–2795 (1996).

103. B. Schenkel, J. Biegert, C. Vozzi, U. Keller, M. Nisoli, G. Sansone, S. Stagira, S. De Silvestri and O. Svelto. *Generation of 3.8-fs pulses from adaptive compression of a cascaded hollow fiber supercontinuum.* Opt. Lett. **28**, 1987 (2003).

104. U. Even. *The Even-Lavie valve as a source for high intensity supersonic beam.* EPJ Techniques and Instrumentation **2**, 17 (2015).

105. M. Moszyński, T. Ludziejewski, D. Wolski, W. Klamra and L. O. Norlin. *Properties of the YAG:Ce scintillator.* Nucl. Instr. Meth. Phys. Res A **345**, 461–467 (1994).

106. F Frassetto, S. Anumula, F. Calegari, A. Trabattoni, M. Nisoli and L. Poletto. *Microfocusing beamline for XUV-XUV pump-probe experiments using HH generation.* Proc. of SPIE **92**, 92080J–1 (2014).

107. I H McLaren W. C. Wiley. *Time-of-flight mass spectrometer with improved resolution.* Rev. Sci. Instrum (1955).

108. A. T. J. B. Eppink and D. H. Parker. *Velocity map imaging of ions and electrons using electrostatic lenses: Application in photoelectron and photofragment ion imaging of molecular oxygen.* Rev. Sci. Instr. **68**, 3477 (1997).

109. P. Johnsson, A. Rouzée, W. Siu, Y. Huismans, F. Lépine, T. Marchenko, S. Düsterer, F. Tavella, N. Stojanovic, H. Redlin, A. Azima and M. J. J. Vrakking. *Characterization of a two-color pump-probe setup at FLASH using a velocity map imaging spectrometer.* Optics Letters **35**, 4163–4165 (2010).

110. James H Underwood. *9 - Imaging properties and aberrations of spherical optics and nonspherical optics.* In J A R Samson and D L Ederer, editors, *Vacuum Ultraviolet Spectroscopy* pages 145–181. Academic Press Burlington (2000). ISBN 978-0-12-617560-8.

111. Hans Wolter. *Spiegelsysteme streifenden Einfalls als abbildende Optiken für Röntgenstrahlen.* Annalen der Physik **445**, 94–114 (1952).

112. P. Mercère, P. Zeitoun, M. Idir, S. Le Pape, D. Douillet, X. Levecq, G. Dovillaire, S. Bucourt, K. A. Goldberg, Patrick P Naulleau and Senajith Rekawa. *Hartmann wave-front measurement at 13.4 nm with λ/120 accuracy.* Opt. Lett. **28**, 1534–1536 (2003).

113. M. Schultze, B. Bergues, H. Schröder, F. Krausz and K. L. Kompa. *Spatially resolved measurement of ionization yields in the focus of an intense laser pulse.* New Journal of Physics **13**, 33001 (2011).

114. G. Kolliopoulos, P. Tzallas, B. Bergues, P. A. Carpeggiani, P. Heissler, H. Schröder, L. Veisz, D. Charalambidis and G. D. Tsakiris. *Single-shot autocorrelator for extreme-ultraviolet radiation.* Journal of the Optical Society of America B **31**, 926–938 (2014).

115. N. Tsatrafyllis, B. Bergues, H. Schröder, L. Veisz, E. Skantzakis, D. Gray, B. Bodi, S. Kuhn, G. D. Tsakiris, D. Charalambidis and P. Tzallas. *The ion microscope as a tool for quantitative measurements in the extreme ultraviolet.* **6**, 21556 (2016).

116. K. Prince, E. Allaria, C. Callegari, R. Cucini, G. De Ninno, S. Di Mitri, B. Diviacco, E. Ferrari, P. Finetti, D. Gauthier, L. Giannessi, N. Mahne, G. Penco, O. Plekan, L. Raimondi, P. Rebernik, E. Roussel, C. Svetina, M. Trovò, M. Zangrando, M. Negro, P. Carpeggiani, M. Reduzzi, G. Sansone, A. N. Grum-Grzhimailo, E. V. Gryzlova, S. I. Strakhova, K. Bartschat, N. Douguet, J. Venzke, D. Iablonskyi, Y. Kumagai, T. Takanashi, K. Ueda, A. Fischer, M. Coreno, F. Stienkemeier, Y. Ovcharenko, T. Mazza and M. Meyer. *Coherent control with a short-wavelength free-electron laser.* Nat Photon **10**, 176–179 (2016).

117. J. A. Arnaud and H. Kogelnik. *Gaussian Light Beams with General Astigmatism.* Applied Optics **8**, 1687–1693 (1969).

118. J. Arnaud. *Representation of Gaussian beams by complex rays.* Applied Optics **24**, 538–543 (1985).